



ALMA MATER STUDIORUM
UNIVERSITÀ DI BOLOGNA

DOTTORATO DI RICERCA IN FISICA

CICLO XXXVII

Settore Concorsuale: 02/A1 - FISICA SPERIMENTALE DELLE INTERAZIONI FONDAMENTALI

Settore Scientifico Disciplinare: FIS/01 - FISICA SPERIMENTALE

Event reconstruction and analysis in the MUonE experiment

CANDIDATO:

Eugenia Spedicato

SUPERVISORE:

Umberto Marconi

COORDINATORE DOTTORATO:

Alessandro Gabrielli

CO-SUPERVISORI:

Giovanni Abbiendi

Angelo Carbone

Esame Finale - Anno 2025

Abstract

The MUonE experiment aims to measure the leading hadronic contribution to the muon anomaly a_μ^{HLO} , due to vacuum polarization, with precision better than 1%. The proposed method is innovative, based on the measurement of the hadronic contribution to the running of the electromagnetic coupling $\alpha(t)$ in the space-like region of momentum transfer. The relevant process is the elastic scattering of 160 GeV muons off the atomic electrons of a low-Z target. The M2 beamline at CERN provides the necessary intensity to reach the statistical goal in few years of data taking. This thesis presents a study of the performance of reconstruction and new developments. One of the main objectives has been the optimization of the tracking algorithm to improve the reconstruction efficiency and the angular resolution, which are the most important figures in the detector design. With the optimal configuration, first results are presented from the 2023 Test Run data, and final considerations are made on the future developments for the experiment.

Contents

1	The anomalous magnetic moment of the muon	6
1.1	Historical overview	6
1.2	Magnetic moments	7
1.3	Renormalization, running constants and QED	9
1.4	Muon $g - 2$ in the Standard Model	11
1.4.1	QED contribution	11
1.4.2	Electroweak contribution	12
1.4.3	Hadronic contribution	12
1.5	Experimental measurement of $g-2$	19
1.6	Theory VS Experiment	20
2	The MUonE experiment	23
2.1	Hadronic contribution: space-like approach	23
2.2	Experimental proposal	25
2.2.1	Precision requested for the measurement	27
2.3	$\mu - e$ scattering theory	28
2.3.1	Elastic differential cross section	29
2.4	Extraction of $\Delta\alpha_{had}(t)$	33
2.5	Experimental apparatus	36
2.5.1	Tracking system	36
2.5.2	Electromagnetic calorimeter	40
2.5.3	Muon filter	41
3	Simulation and reconstruction tools	42
3.1	FairMUonE software	42
3.1.1	Simulation	42
3.1.2	Event reconstruction	44
3.1.3	Alignment	45
3.2	Reconstruction performance	46
3.2.1	Reconstruction efficiencies	47
3.2.2	Angular resolution	51

3.2.3	Tilted modules	54
4	Test Run 2023	60
4.1	Data recorded and offline event selection	62
4.2	First studies on TB data	63
5	Real data and MC comparison	68
5.1	Results	73
5.1.1	Analysis of the problem	77
5.1.2	Comparison of the shapes	83
5.2	Future steps	86
6	Conclusion and outlooks	89
	Appendices	93
A	Automatized workflow with Snakemake	94
B	First background studies with minimum bias simulation	97
C	Comparison of data with minimum bias MC simulation	102
D	Angular resolution and track quality with improved reconstruction algorithm	105
	Acknowledgement	112

Introduction

MUonE is an experiment being prepared at the CERN M2 muon beam line. Its primary goal is to measure the leading hadronic contribution to the muon anomaly a_μ^{HLO} , a crucial component to understand the observed discrepancy between experimental measurements and theoretical predictions of the muon's anomalous magnetic moment ($\frac{g-2}{2}$). MUonE aims to measure a_μ^{HLO} using an innovative approach [30]. The experiment will exploit elastic collisions obtained by a high-intensity 160 GeV muon beam onto the atomic electrons of a low- Z material target $\mu^+e^- \rightarrow \mu^+e^-$. By precisely measuring the differential elastic cross section through angular distributions of the scattered particles from these elastic collisions, the experiment will determine the running of the electromagnetic coupling constant, $\alpha(t)$, which is then used to determine the leading hadronic contribution to the muon anomaly.

The measurement will be performed using a modular detector composed of an array of identical tracking stations each one mounting a thin target. The fundamental detector unit consists of two consecutive tracking stations, allowing the tracking of incoming muons upstream of the interleaved target element and of the outgoing particles downstream of it. Each tracking station is equipped with 2S modules, developed by the CMS collaboration for the planned upgrade of their outer tracker. These modules operate at the LHC clock frequency of 40 MHz, providing hit position measurements with a spatial resolution of $25\ \mu\text{m}$. The M2 beam can deliver a muon intensity of up to 2×10^8 muons per spill. Since the muons enter the detector with an unknown phase relative to the clock cycle, significant effort has been invested in optimizing the data acquisition system and the reconstruction algorithms—work that is ongoing and requires further refinement. Additionally, the detector will be equipped with a magnetic spectrometer to precisely measure the incoming muon momenta, as well as particle identification (PID) capabilities, provided by an electromagnetic calorimeter and a muon identifier. The detector layout has been optimized and tested in recent years through dedicated test beam activities.

In this thesis, I present the work I have done to study the performance of the detector. My main task has been to study and optimize the performance of the tracking algorithm to improve tracking efficiency and angular resolution, which are the most critical operational parameters of the detector. With the optimized configuration, a first analysis of

the 2023 test run data has been carried out.

The thesis is organized into five chapters. Chapter 1 sets the context by providing the formalism, discussing the theoretical foundations, and outlining the current understanding of the discrepancy between theory and experimental measurements of the muon's anomalous magnetic moment $\frac{g-2}{2}$. Chapter 2 describes the new experimental method proposed by MUonE to measure the hadronic vacuum polarization and the detector setup. This chapter includes a detailed discussion of the elastic scattering process and the role of higher-order approximations in describing the collision process. Chapter 3 presents the simulation and analysis framework, describing the main features and evaluating the physics performance of the FairMUonE reconstruction. In particular, reconstruction efficiency and angular resolution has been quantified varying different reconstruction parameters, identifying the optimal reconstruction configuration. Chapter 4 introduces the setup of the 2023 test run that has been carried out at the CERN SPS North Area with the M2 muon beam. The main goals are presented, together with the first results from data collected. Finally, Chapter 5 presents an initial physics analysis, detailing the procedure along with the selection criteria applied to both MC and data to obtain a clean sample of elastic events. The comparison between data and MC was conducted using both an absolute normalization and a normalization to the number of events in real data. Final considerations and outlooks are provided, with particular focus on the next steps needed to enhance the MUonE experimental setup.

Chapter 1

The anomalous magnetic moment of the muon

1.1 Historical overview

In 1936 C. D. Anderson and S. Neddermeyer discovered a new particle as a constituent of cosmic-ray showers through a cloud chamber measurement; those data were commented by them in 1937 [1] as

the first experimental evidence for the existence of particles of both penetrating and non-penetrating character [...]. Moreover, the penetrating particles in this range do not ionize perceptibly more than the non-penetrating ones, and cannot therefore be assumed to be of protonic mass. [...] The non-penetrating particles are readily interpreted as free positive and negative electrons. Interpretations of the penetrating ones encounter very great difficulties, but at present appear to be limited to the following hypotheses: (a) that an electron (+ or -) can possess some property other than its charge and mass which is capable of accounting for the absence of numerous large radiative losses in a heavy element; or (b) that there exist particles of unit charge, but with a mass (which may not have a unique value) larger than that of a normal free electron and much smaller than that of a proton

The existence of such a particle was confirmed in 1937 by J.C. Street and E.C. Stevenson, in particular they supported the idea that these were “particles of electronic charge, and of mass intermediate between those of the proton and electron[...]” [2].

Because of its mass, many physicists at that time believed that this new entity could be related to the one theoretically predicted by Yukawa in 1935: the *mesotron* (shortened as *meson*), mediator of the strong nuclear force. But, in 1946, an important experiment by M. Conversi, E. Pancini and O. Piccioni [3] showed that those new entities were

not affected by the nuclear force, being unreactive in the nuclear sense, thus could not correspond to the Yukawa's hypothesis. His predicted particle, nowadays known as π meson, was finally identified in 1947 [4].

Nevertheless, it was found that in some cases an object that appeared to be a meson would stop and then emit another particle of somewhat lower mass. Hence the origin of cosmic ray muons became clear: the majority of π mesons, entering the atmosphere, decays into muons which are able to reach the Earth's surface; with this discovery they managed to differentiate the Yukawa particle from the earlier-discovered muon.

Nowadays, in the framework of the Standard Model, the muon is classified as a lepton. Those are particles of half-integer spin classified in three generations:

$$L_e = \begin{pmatrix} \nu_e \\ e^- \end{pmatrix}_L \quad L_\mu = \begin{pmatrix} \nu_\mu \\ \mu^- \end{pmatrix}_L \quad L_\tau = \begin{pmatrix} \nu_\tau \\ \tau^- \end{pmatrix}_L \quad (1.1)$$

together with their respective right-handed antiparticles.

The mass is the key parameter which differentiate those fermions. The electron can be studied more precisely because of its stability, but nowadays also the muon can be studied extremely well in experiments and it reveals to be a good leptonic candidate for the discovery of physics beyond the Standard Model.

1.2 Magnetic moments

A particle of mass m with electric charge e orbiting in a magnetic field \vec{B} carries a magnetic dipole moment

$$\vec{\mu}_L = \left(\frac{e}{2m} \right) \vec{L} \quad (1.2)$$

where $\vec{L} = m\vec{r} \times \vec{v}$ is the orbital angular momentum. This $\vec{\mu}_L$ quantifies the level of torque $\vec{\tau}$ that a particle experiences when placed in an external \vec{B} field:

$$\vec{\tau} = \vec{\mu} \times \vec{B}. \quad (1.3)$$

After Stern-Gerlach experiment in 1922 [5], the concept of spinning particle was introduced in 1925 by G.E. Uhlenbeck and S.A. Goudsmit [6] as an explanation of the anomalous Zeeman effect, that was showing a level splitting of atomic spectra in the presence of a magnetic field [7]. The spin is defined as a quantum angular momentum $\vec{S} = \frac{\hbar}{2}\vec{\sigma}$, thus an intrinsic magnetic moment can be defined as:

$$\vec{\mu} = g_s \left(\frac{e}{2m} \right) \vec{S} = g_s \frac{\mu_B}{\hbar} \vec{S} \quad (1.4)$$

where μ_B is the Bohr magneton and g_s is the dimensionless gyromagnetic ratio. To explain observations, g_s needed to assume empirically the value of 2.

In 1928, Dirac presented his famous theory of the electron [8], whose equation in an external \vec{B} field took the form

$$(i\partial_\mu - eA_\mu)\gamma^\mu\psi = m\psi. \quad (1.5)$$

Together with the prediction of the existence of antiparticles, the theory also predicted, unexpectedly, that the value of g_s needed to be equal to 2, consistently with the value measured in earlier experiments. Acting on Eq. 1.5, the non-relativistic form resulted in [9]:

$$\left[-2im\frac{\partial}{\partial t} - \vec{\nabla}^2 - e\vec{B} \cdot (\vec{L} - 2\vec{S})\right]\psi = 0, \quad (1.6)$$

where it is clearly shown that a unit of spin angular momentum interacts with a magnetic field twice as much as a unit of orbital angular momentum.

Many years of measurements supported this theoretical prediction, even though with large error bars. It took about 20 years of experimental effort to establish that the electron magnetic moment differs from 2 by about a tiny fraction. The advent of Quantum Field Theory (QFT) made it clear that an *anomalous* contribution to this quantity

$$a_e = \frac{g_e - 2}{2} \quad (1.7)$$

was needed when describing the interaction of the electron with an external \vec{B} field. In 1947 J. Schwinger [10] stated that from a theoretical point of view “discrepancies can be accounted for by a small additional electron spin magnetic moment”, that arises from the lowest-order radiative correction to the Dirac moment.

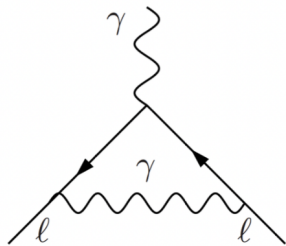


Figure 1.1: Lowest order QED contribution to the electron anomalous magnetic moment calculated by Schwinger.

Due to quantum fluctuations via virtual electron-photon interactions, the leading order quantum correction (one-loop) for the anomalous magnetic moment (Eq.1.7) was predicted to be

$$a_e = \frac{\alpha}{2\pi} \sim 0.00116 \quad (1.8)$$

and the corresponding Feynman diagram is the one shown in Fig. 1.1.

In the same year, this deviation was experimentally confirmed by P. Kusch and H. M.

Foley [11], resulting to be:

$$g_e^{exp} = 2 \cdot (1.00119 \pm 0.00005), \quad (1.9)$$

in agreement with Schwinger's prediction. This confirmation of the perturbative method is one of the Quantum Electrodynamics (QED) triumphs.

1.3 Renormalization, running constants and QED

In QED calculations can be performed by a perturbation method, based on Feynman diagrams, at subsequent orders of series expansion in powers of the coupling constant α . In doing so, one of the main problems is the appearance of divergent quantities. Infinities come from the integration over variables (as the momenta of virtual particles) that are not directly measurable and can therefore reach extremely high or low values. Thus, in evaluating the integral, it should be integrated only up to a cut-off. If the diagram contribution diverges sending the cutoffs to infinity or to zero, one says that the diagram has respectively an ultraviolet or an infrared divergence. The procedure to actually renormalize a theory, trying to get rid of these infinities, involves a set of advanced mathematical techniques. The basic points are:

1. *Regularization*: The infinities are removed with the introduction of a cutoff Λ , representing the finite domain of validity of that given theory. The integral is said to have been 'regularized';
2. *Renormalization*: Redefine a finite number of parameters to absorb the infinities. In this process a mass scale μ , called renormalization scale, is introduced.

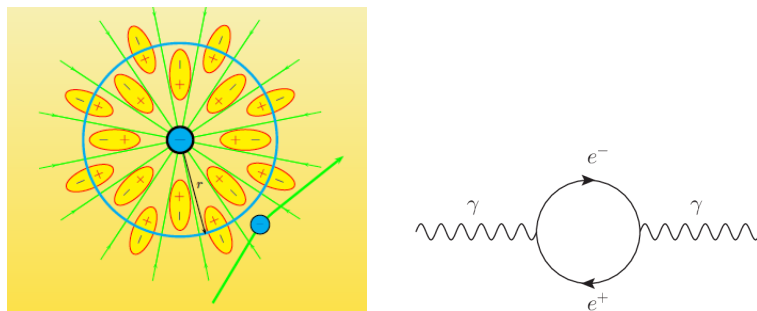


Figure 1.2: Left: Representation of the vacuum polarization phenomenon causing charge screening by virtual pairs. Right: Feynman diagram of the vacuum polarization effect.

The infinities of the theory end up in the so-called *bare* parameters. Let's consider an electron. Due to quantum fluctuations, spacetime is full of particle-antiparticle pairs

(mainly $e^- - e^+$) coming from the vacuum polarization effect, represented in Fig. 1.2. This cloud of particles shields the electron and its measured quantities (e.g. electric charge, mass) will depend on the energy scale/distance of the process through which we probe the particle. Bare parameters are the values in the absence of vacuum interactions, while *renormalized* ones are the experimentally measured values, that depend on the energy. The more the probing particle is able to get through the virtual cloud, the more intense will be the electromagnetic interaction. Thus, the coupling constant α grows with the momentum transfer q^2 . This phenomenon is a general feature of quantum field theories known as running of the coupling constants. It can be described quantitatively starting from the so-called β function that describes the variation of a renormalized parameter as a function of the energy scale:

$$\beta(g) = \left(\frac{dg}{d\ln\mu} \right) \xrightarrow{QED} \beta(e) = \frac{e^3}{12\pi^2}, \quad (1.10)$$

where g in this case is the renormalized charge and μ the energy scale. In terms of the coupling constant, Eq.1.10 becomes:

$$\left(\frac{d\alpha}{d\ln\mu^2} \right) = \frac{\alpha^2}{3\pi}. \quad (1.11)$$

To get how the coupling α runs with energy, the integration is done considering an arbitrary scale q_0 :

$$\int_{\alpha(q_0^2)}^{\alpha(q^2)} \frac{1}{\alpha^2} d\alpha = \int_{q_0^2}^{q^2} \frac{1}{3\pi} d\ln\mu^2$$

$$\alpha(q^2) = \frac{\alpha(q_0)}{1 - \frac{\alpha(q_0)}{3\pi} \ln\left(\frac{q^2}{q_0^2}\right)}. \quad (1.12)$$

The closer one gets (increasing the energy scale q is equivalent to probing a smaller distance scale), the greater the observed effect of the virtual processes is, which modifies the electric charge.

Therefore, the running of the electromagnetic coupling goes like:

$$\alpha(q^2) = \frac{\alpha}{1 - \Delta\alpha(q^2)} \quad (1.13)$$

where $\alpha = \alpha(q = 0)$ is the fine structure constant and

$$\Delta\alpha = \Delta\alpha_{lep}(q^2) + \Delta\alpha_{top}(q^2) + \Delta\alpha_{had}(q^2) \quad (1.14)$$

, meaning that the vacuum polarization loops in Fig. 1.2-right may be composed by leptons but also quarks. Vacuum polarization enters at the two loop level (fourth order in the electric charge) and it is the only source of difference between the g -factors of the electron and muon, because of their different mass.

1.4 Muon $g - 2$ in the Standard Model

The muon anomaly a_μ receives contribution from QED, electroweak and strong interactions:

$$a_\mu = a_\mu^{QED} + a_\mu^{EW} + a_\mu^{had}, \quad (1.15)$$

the representative Feynman diagrams are shown in Fig. 1.3.

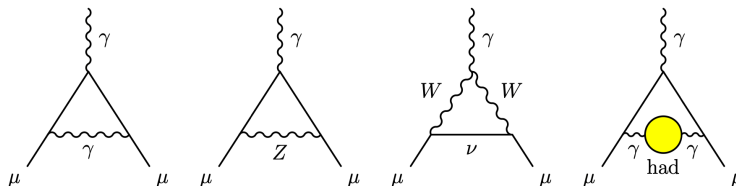


Figure 1.3: Representative diagrams contributing to a_μ . From left to right: leading order QED (Schwinger term), lowest-order electroweak, lowest-order hadronic contribution.

The QED and electroweak contributions can be calculated with extreme precision by perturbative calculation, and the QED gives the largest contribution to the anomaly. The hadronic one, instead, cannot be obtained through perturbation theory, and its calculation must rely on data-driven method (based on experimental data) or Lattice QCD (LQCD). It is really demanding to measure this contribution and it presents the biggest uncertainty. The muon anomaly provides a particularly sensitive probe for new physics, more than the electron as the sensitivity goes with m_l^2 ($m_\mu^2/m_e^2 \sim 43000$).

The current Standard Model prediction for the muon anomaly, as reported in the White Paper (WP) by the Muon $g - 2$ Theory Initiative in 2020 [12] is:

$$a_\mu^{SM} = 116591810(43) \times 10^{-11}. \quad (1.16)$$

The Theory Initiative is planning to write an updated estimate, given some new results on the measurement needed for the data-driven method and the new LQCD results, before the release of the Fermilab $g - 2$ experiment's final measurement result, expected in 2025.

1.4.1 QED contribution

The QED contribution can be divided in three main contributions:

$$a_\mu^{QED} = A_1 + A_2(m_\mu/m_e) + A_2(m_\mu/m_\tau) + A_3(m_\mu/m_e, m_\mu/m_\tau) \quad (1.17)$$

taking into account the masses of the three leptons that give contribution in the internal loops. Each coefficient A_j can be expanded in perturbation theory as a series in α/π :

$$A_j = \sum_{i=j}^N A_j^{(2i)} \left(\frac{\alpha}{\pi}\right)^i. \quad (1.18)$$

Given the smallness of the QED coupling constant, it allows to calculate each A_j by using perturbation theory for QED. The A_1 term is universal for all leptons and its lowest order contribution represents the one loop calculation given in 1947 by Schwinger and shown in Fig. 1.1.

Summing the terms in the perturbative QED expansion up to fifth order in α and using the measurement of α from Cs atoms oscillations [13], the value of muon's a_μ^{QED} reported in [12] is:

$$a_\mu^{QED} = 11658471.8931(104) \times 10^{-10}. \quad (1.19)$$

1.4.2 Electroweak contribution

Electroweak interaction effects are mediated by the exchange of heavy weak gauge bosons W^\pm and Z or the Higgs, as represented in Fig. 1.4.

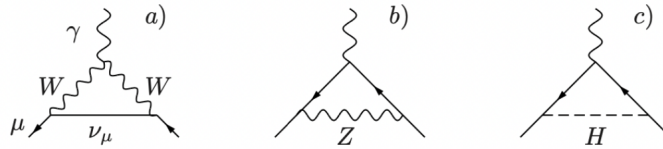


Figure 1.4: The leading electroweak contributions to a_μ .

The EW contributions are strongly suppressed with respect to the pure QED ones, due to the heavy boson masses, as $(m_\mu/m_W)^2$. Two loop contribution is not negligible and also includes non-perturbative hadronic corrections, which appear from diagrams including light quark loops.

The resulting value of the electroweak contribution a_μ^{EW} reported in [12] is:

$$a_\mu^{EW} = 153.6(1.0) \times 10^{-11}. \quad (1.20)$$

1.4.3 Hadronic contribution

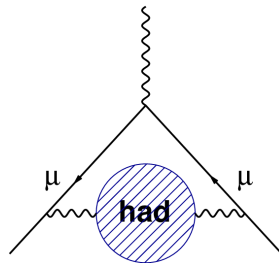


Figure 1.5: The leading hadronic contribution to a_μ .

The hadronic contribution is the one with the larger uncertainty in the estimate of a_μ^{SM} . This is mainly due to the fact that its evaluation cannot be done through

perturbative methods. Given the non-perturbative nature of QCD at low energy, different methods need to be used. At the moment, the two competitive approaches are:

1. **Data-driven** based on dispersion relations together with the optical theorem. This makes use of the measured hadron production cross section from e^+e^- annihilation;
2. **Lattice QCD** consisting in a non-perturbative approach to compute hadronic observables of QCD theory of quarks and gluons from first principles.

The leading hadronic contribution comes from vacuum polarization (VP) diagrams as in Fig. 1.5, where a hadronic blob is inserted in the internal photon line. This diagram is also responsible for the biggest uncertainty, related to the LO term a_μ^{HLO} . It is the most sizable hadronic effect and cause the biggest source of uncertainty, in particular the LO term a_μ^{HLO} . The higher order term a_μ^{HNLO} is suppressed by a power of α with respect to the LO term and its error does not play a critical role.

The second class of relevant hadronic terms is the so-called light-by-light (LbL), whose diagram is obtained by a four-point function as in Fig. 1.6) This is a more involved and problematic calculation. It obtains a similar contribution to the muon anomaly as

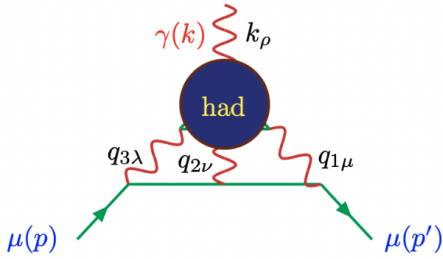


Figure 1.6: Diagram of the hadronic light-by-light interaction process.

the NLO vacuum polarization term, however the LbL contribution has a sizable larger uncertainty, which is about half the uncertainty of the leading VP term.

Data-driven method: dispersive approach with time-like e^+e^- process Dispersion relations, together with the optical theorem and experimental data of the cross section of e^+e^- annihilation into hadrons, have been the traditional method to evaluate a_μ^{HLO} .

Because of the analyticity of the vacuum polarization function, the following dispersion relation holds:

$$\frac{\Pi_\gamma^{had}(q^2)}{q^2} = \int_0^\infty \frac{ds}{s} \frac{1}{\pi} \text{Im}\Pi_\gamma^{had}(s) \frac{1}{q^2 - s}, \quad (1.21)$$

representing the hadronic VP contribution.

Optical theorem enables to relate the imaginary part of the vacuum polarization amplitude to the total cross section of the time-like process $e^+e^- \rightarrow had$ (Fig. 1.7):

$$\text{Im}\Pi_\gamma^{had}(s) = \frac{s}{4\pi\alpha} \sigma_{had}^0(e^+e^- \rightarrow had) = \frac{\alpha}{3} R_{had}(s), \quad (1.22)$$

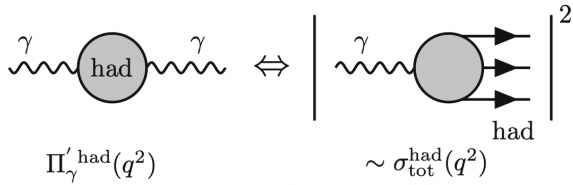


Figure 1.7: Illustrative representation of the optical theorem.

where the R-ratio

$$R_{had}(s) = \frac{\sigma_{had}^0}{4\pi\alpha^2/(3s)} \quad (1.23)$$

relies on the cross section measured. The dispersion relation in Eq.1.21 needs the bare cross section for e^+e^- annihilation, that is different from the measured one σ_{had} . Therefore, the bare parameter can be renormalized as a function of the measurable one such that:

$$\sigma_{had}^0 = \sigma_{had} \frac{\alpha^2}{\alpha(s)^2}. \quad (1.24)$$

Given that, the resulting R-ratio is:

$$R_{had}(s) = \frac{\sigma_{had}}{4\pi\alpha(s)^2/(3s)}. \quad (1.25)$$

Exploiting the dispersion relation in Eq.1.21, the lowest order hadronic contribution to the anomaly can be computed through:

$$a_\mu^{HLO} = \frac{\alpha}{\pi} \int_0^\infty \frac{ds}{s} \frac{1}{\pi} \text{Im}\Pi_{had}(s) K(s), \quad (1.26)$$

where $K(s)$ is the kernel function defined as:

$$K(s) = \int_0^1 dx \frac{x^2(1-x)}{x^2 + (1-x)s/m_\mu^2}. \quad (1.27)$$

The integral can be divided in two contributions: one for the low-energy region, below a certain E_{cut} value, and the other for the high energy tail:

$$a_\mu^{HLO} = \left(\frac{\alpha m_\mu}{3\pi}\right)^2 \left(\int_0^{E_{cut}^2} ds \frac{R_{had}^{data}(s) \hat{K}(s)}{s^2} + \int_{E_{cut}^2}^\infty ds \frac{R_{had}^{pQCD}(s) \hat{K}(s)}{s^2} \right). \quad (1.28)$$

The latter can be evaluated with perturbative QCD and gives negligible contribution to the final uncertainty. $\hat{K}(s)$ is the rescaled kernel function:

$$\hat{K}(s) = \frac{3s}{m_\mu^2} K(s). \quad (1.29)$$

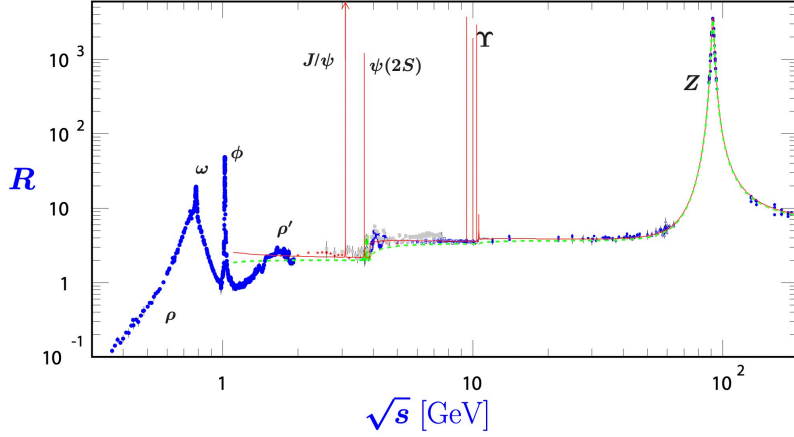


Figure 1.8: Experimental data (in blue) of $R(s)$. The green curve represents a naive quark-parton model prediction, while the red one follows the 3-loop pQCD calculation [14].

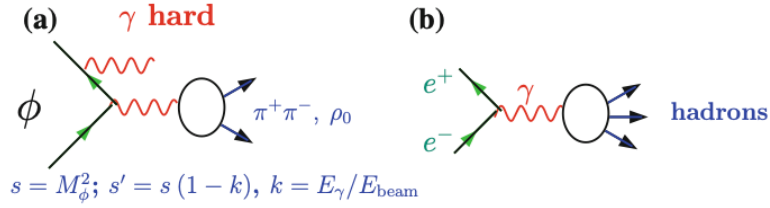


Figure 1.9: a) Principle of the radiative return; b) Direct scan mode [16].

Because of the $1/s^2$ term in Eq.1.28, the low energy region gives the major contribution to the integral. In Fig. 1.8 the $R(s)$ behavior as a function of \sqrt{s} shows the large fluctuations present at low energies, given by resonances production. Therefore this constitutes the main difficulty of the method. In that plots, the dominant low energy part is given by the channel $e^+e^- \rightarrow \pi^+\pi^-$, forming the ρ resonance around (~ 0.77 GeV). This represent the 73% of the HVP contribution to a_μ and the 70% on the squared uncertainty. Increasing the energy, more channels open up.

There are two main methods for the cross section measurement:

1. **Direct scan mode** (Fig. 1.9.b): the beam energy is adjusted to provide measurements at different center-of-mass (CM) energies, doing a scan at discrete energy points to cover the full accessible range. The high energy resolution of these machines allows precision studies especially for narrow peak resonances ($\omega \phi$). BESIII and KEDR are doing scans from 2 GeV to 5 GeV and VEP-2000 is doing scan below

2 GeV. There CMD-3 and SND detectors are installed at the interaction region of the target [15];

2. **Radiative return method** (Fig. 1.9.a): the collider is operating at fixed CM energy. Here the high statistics allow for an effective scan over different masses of the hadronic system through the emission of initial state photons, whose spectrum can be calculated and, in some cases, measured directly. This emission reduces the invariant mass from s to $s' = s(1 - k)$ where k is the energy fraction carried by the photon. Therefore, $\sigma_{had}(s')$ can be measured at all $\sqrt{s'}$, lower than the fixed \sqrt{s} . This allows to cover a wide range of $\sqrt{s'}$ values providing a continuous cross section measurement. This method is particularly interesting for meson machines like ϕ and B- factories with high luminosities. Important results have been achieved by KLOE (at the DAΦNE collider in Frascati) and BaBar (at the PEP-II collider at SLAC) by measuring the $\pi^+\pi^-$ cross section which is the dominating channel for σ_{had} .

It is important to remark that there are some discrepancies between results from different experiments and this strongly affects the precision of the combined cross sections used for the evaluation of the dispersion integrals. The most precise measurement of the $\pi^+\pi^-$ cross sections for BABAR [18], KLOE [17] and, recently, CMD-3 [19] experiments do not agree within the given uncertainties, as shown in Fig. 1.10. The yellow band corresponds to the average of all experiments before CMD-3 (the most recent one), where the gray band includes additional uncertainties taking into account the KLOE-BABAR inconsistency.

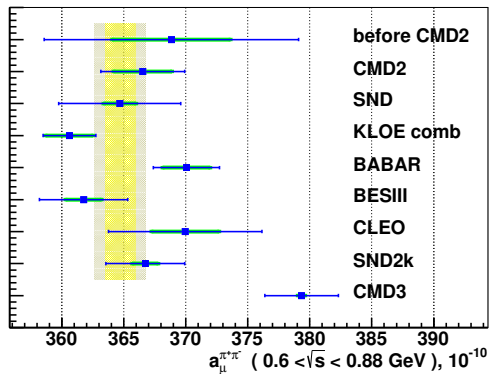


Figure 1.10: The $\pi^+\pi^-$ contribution to the a_μ for the low-energy range ($0.6 < \sqrt{s} < 0.88$ GeV) from different experiments [19].

The discrepancy between BABAR and KLOE was deeply discussed in the Muon $g-2$ Theory Initiative [12]. However, no understanding of the difference could be achieved and consequently no solution to the problem emerged yet. The recommended estimate given in [12] was:

$$a_\mu^{HLO} = (693.1 \pm 4.0) \times 10^{-10}, \quad (1.30)$$

where the final error is evaluated taking into account the tension between different experimental results (excluding the recent CMD-3 result, which was not yet available). In addition to the LO results, also the higher-order vacuum polarization contributions have been evaluated, as not negligible. The final VP term estimates in [12] resulted in:

$$\begin{aligned} a_\mu^{HVP} &= a_\mu^{HLO} + a_\mu^{HNLO} + a_\mu^{HNNLO} = \\ &= [(693.1 \pm 4.) - (9.83 \pm 0.07) + (1.24 \pm 0.01)] \times 10^{-10} = \\ &= (684.5 \pm 4.0) \times 10^{-10}. \end{aligned} \quad (1.31)$$

It's important to remark once again that the WP [12] was published in 2020, while the new important CMD-3 result in [19] was achieved in 2023. Thus, a new evaluation for the theoretical estimate of a_μ^{HVP} needs to be done taking into account this new result. In addition, further studies on the old evaluations based on KLOE and BABAR data have to be kept on in order to understand the reason of this discrepancy. Some hypotheses have been made in [23], where this tension has been reviewed. It seems that these differences may be related to the treatment of radiative corrections and in particular the strong reliance of certain experiments on the results of Monte Carlo generators.

Summing up all the SM contributions, the final theoretical value reported in [12] is:

$$a_\mu = 116591890(43) \times 10^{-11}. \quad (1.32)$$

Lattice QCD approach In 2021, the first competitive result from LQCD was published by the BMW collaboration [20]. Before that, the only estimate that allowed a reasonable comparison with the experimental measurement, that had a precision at the level of ppm, was coming from the data-driven dispersive method discussed above. LQCD evaluations of a_μ^{HVP} are based on the computation of the electromagnetic current-current correlator

$$C_{\mu\nu}(t) = \langle J_\mu(c) J_\nu(0) \rangle \quad (1.33)$$

where

$$J_\mu(x) = \frac{2}{3}(\bar{u}\gamma_\mu u)(x) - \frac{1}{3}(\bar{d}\gamma_\mu d)(x) - \frac{1}{3}(\bar{s}\gamma_\mu s)(x) + \dots \quad (1.34)$$

The vacuum polarization tensor is defined as Eq.1.33's Fourier transformed:

$$\Pi_{\mu\nu}(Q) = \int dx^4 e^{iQ \cdot x} C_{\mu\nu}(x). \quad (1.35)$$

Traditionally the leading hadronic contribution to the muon anomalous magnetic moment is expressed as:

$$a_\mu^{HLO} = \left(\frac{\alpha}{\pi}\right)^2 \int_0^\infty dQ^2 f(Q^2) \hat{\Pi}(Q^2) \quad (1.36)$$

where $\hat{\Pi}(Q^2) = 4\pi^2[\Pi(Q^2) - \Pi(0)]$ and $f(Q^2)$ is a known function [12].

Lattice calculations are performed by replacing integrals over the full phase space with sums over finite lattice volumes. Extrapolation to continuum, namely to lattice spacing $a \rightarrow 0$, and to infinite volumes are therefore required to obtain the desired quantities. Reducing the uncertainty in the calculation to below half a percent is a major challenge. In particular, a number of contributions to this uncertainty must be controlled. They are: (a) statistical uncertainties; (b) those associated with the finite spatial size L and time T of the lattice; (c) with the extrapolation to the continuum limit; (d) with fixing the five parameters of four-flavour QCD; (e) with QED and strong-isospin breaking corrections.

In order to better compare results from different LQCD calculations and improve the accuracy of the HVP term by substituting the dispersive results, based on R-ratio measurements, by lattice inputs in a time-region where the lattice data turn out to be more precise, the integral in Eq.1.36 can be divided into three parts [21]:

$$a_\mu^{HLO} = a_\mu^{SD} + a_\mu^W + a_\mu^{LD}. \quad (1.37)$$

These three terms corresponds respectively to short-distance (corresponding to short Euclidean time), intermediate and long-distance window. LQCD has the best precision in the intermediate window, while the R-ratio data are more precise in the short- and long-distance windows [21]. Comparison between the two methods can be done more stringerly in the intermediate window. This corresponds to distance $0.4 - 1.0$ fm in the time-like approach.

From 2021, different LQCD collaborations confirmed the result presented by the BMW

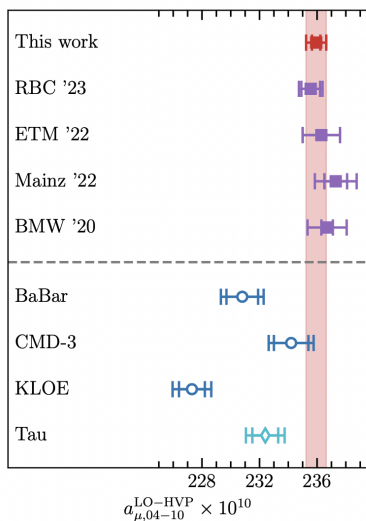


Figure 1.11: Comparison of the LO contribution to the muon anomaly from vacuum polarization in the intermediate-distance region ($0.4 - 1.0$ fm). In the data-driven case, results are taken from [23] that uses the measurements of the two-pion spectrum obtained in individual electron-positron annihilation experiments. The LQCD results come from different collaborations, “this work” refers to the new BMW result in [22].

collaboration, which has recently updated its value with a new more precise estimate [22]:

$$a_{\mu}^{HLO} = 11659201.9(3.8) \times 10^{-10}. \quad (1.38)$$

In Fig. 1.11 a comparison of results for the full intermediate window contribution from different lattice determinations and data-driven results is shown. While the LQCD estimates seem to perfectly agree within each other, those results display significant tensions with the data-driven result. The disagreement between the two methods is enhanced in the low energy range. In [24] the hypothesis that the tensions can be explained by modifying the R-ratio in different intervals of centre-of-mass energy is tested. Their study also suggests that the measurement by KLOE experiment is impacted by the higher-order radiative effects, at a level larger than the systematic uncertainty assigned to this effect[23]. But the situation is not clear yet, further studies need to be done.

1.5 Experimental measurement of g-2

Different experiments in the last sixty years have been devoted to in the measurement of a_{μ} : from CERN g-2 experiment (1958-1962) reaching a 0.4% precision [25], to Brookhaven's E821 experiment (1990-2004) achieving 0.5 ppm [26], until the g-2 experiment at Fermilab that in August 2023 released the new result from Run-2 and Run-3 data, allowing to reach a precision of 0.20 ppm, combined with Run-1 data [27].

The new world average after this measurement is

$$a_{\mu}^{exp} = 11659205.9(2.2) \times 10^{-10} \rightarrow 0.19 \text{ ppm}. \quad (1.39)$$

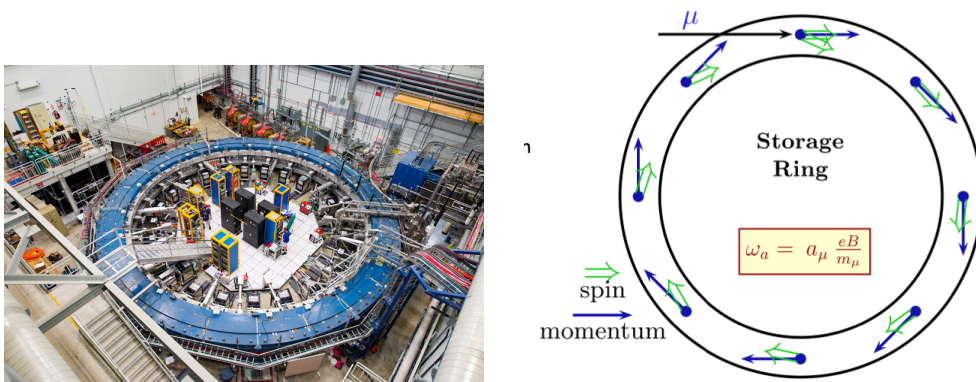


Figure 1.12: Left: picture of storage ring of the g-2 experiment at Fermilab. Right: working principle of polarized muons running inside the storage ring.

The working principle of these g-2 experiments is based on the measurement of the magnetic anomaly of muons in a magnetic storage ring, with a uniform vertical magnetic field \vec{B} and weakly focusing electric field \vec{E} (Fig. 1.12). The observable is the muon's *anomalous precession frequency* $\vec{\omega}_a = \vec{\omega}_s - \vec{\omega}_c$, where

$$\vec{\omega}_s = g \frac{e\vec{B}}{2m_\mu} + (1 - \gamma) \frac{e\vec{B}}{\gamma m_\mu}, \quad \vec{\omega}_c = \frac{e\vec{B}}{\gamma m_\mu} \quad (1.40)$$

represents respectively the muon spin precession, given by the interaction between the muon intrinsic magnetic moment and the magnetic field, and the cyclotron frequency. If $g_\mu \neq 2$, then $\vec{\omega}_s \neq \vec{\omega}_c$. Thus $\vec{\omega}_a \neq 0$ and it can be expressed for relativistic muons as:

$$\vec{\omega}_a = a_\mu \frac{e}{m_\mu} \vec{B} + \frac{e}{m_\mu} \left[\left(a_\mu - \frac{1}{\gamma^2 - 1} \right) \frac{\vec{\beta} \times \vec{E}}{c} + a_\mu \left(\frac{\gamma}{\gamma + 1} \right) (\vec{\beta} \cdot \vec{B}) \vec{\beta} \right]. \quad (1.41)$$

Choosing the momentum to be 3.094 GeV/c, the so-called *magic momentum*, the Eq.1.41 takes the form:

$$\vec{\omega}_a = a_\mu \frac{e}{m} \vec{B}, \quad (1.42)$$

while the third term is negligible because \vec{B} is perpendicular to the muon's orbit. Therefore, a_μ can be determined by a precise measurement of $\vec{\omega}_a$ and \vec{B} . The aim of the g-2 experiment at Fermilab is to reach 0.14 ppm precision with the full dataset, aiming to another factor 2 improvement in statistical precision with respect to the last result.

An alternative and innovative approach with respect to all previous experiments has been proposed at J-PARC in Japan. The muon g-2/EDM experiment aims at reaching a precision comparable to the Fermilab experiment with completely different systematics. It will feature an ultra-cold muon beam, with a factor of 10 lower momentum, injected into a compact storage ring, 20 times smaller in diameter and with a highly uniform magnetic field with respect to the previous g-2 experiment [28].

It is important to perform an experiment with different systematic effects with respect to all previous ones, as this will enable an independent confirmation of the actual experimental measurement a_μ^{exp} .

1.6 Theory VS Experiment

In previous sections, the general landscape on muon anomaly has been described both on the theoretical and experimental side. The current theory estimates of the muon anomaly are reported in Eq.1.32, Eq.1.38, respectively from the Theory Initiative and the BMW collaboration based on the Lattice QCD. The current best experimental measurement is given by 1.39 from the last Fermilab g-2 result. Fig. 1.13 shows a comparison of all the different estimates of a_μ with the methods discussed. The discrepancy between theory

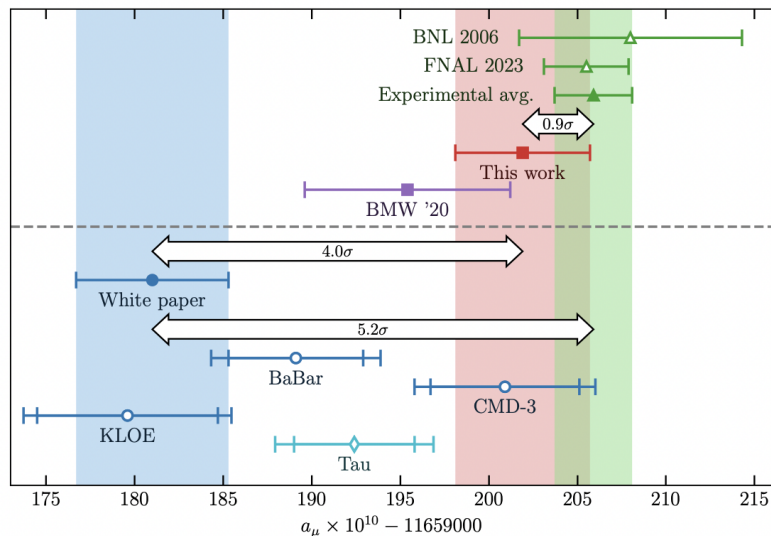


Figure 1.13: Comparison of SM predictions of the a_μ with its measured value [22]. The panel above the dashed line shows a comparison of the world-average measurement (green band), with the SM prediction obtained in [22] - including the new BMW result- (red band). The panel below the line shows the predictions for a_μ obtained in the data-driven approach using the most precise measurements of the two-pion spectrum in e^+e^- annihilation. These correspond to BaBar, KLOE and CMD-3. The blue band shows the muon g-2 Theory Initiative combination of the data-driven results [12], obtained prior to the publication of the CMD-3.

and experiment $\Delta a_\mu = a_\mu^{th} - a_\mu^{exp}$ varies depending on the method used for the theoretical calculation:

- $\Delta a_\mu = 5.2\sigma$ between the 2020 Theory Initiative result (mainly based on dispersive method) and the current experimental average;
- $\Delta a_\mu = 0.9\sigma$ between the new BMW result from LQCD and the current experimental average;
- $\Delta a_\mu = 4.0\sigma$ between the new BMW result from LQCD and the 2020 Theory Initiative result.

It is clear that the landscape is puzzling. There are important discrepancies within the dispersive method and the old Theory Initiative estimate seems not to agree with the LQCD results. Moreover, the latter seems to reduce the difference with the experimental value, bringing it to below 1σ .

The situation is intriguing. A new independent and alternative data-driven method for

the evaluation of the theoretical value of a_μ may be essential to shade some light on this topic. In this respect the MUonE experiment is presented.

Chapter 2

The MUonE experiment

It has been shown that the largest contribution to the theoretical uncertainty of a_μ comes from the hadronic vacuum polarization term at LO a_μ^{HLO} . The different approaches used until now to calculate this contribution are not enough to draw a solid conclusions on the existing discrepancy between the theoretical evaluations and the experimental measurement. The MUonE collaboration is proposing an alternative method to shade some light on this intriguing puzzle [29, 30, 31, 32]. The innovative proposal consists in evaluating the hadronic vacuum polarization term through an high precision measurement of the effective electromagnetic coupling α_{QED} , in the space-like region of momenta where the vacuum polarization contribution is a smooth function.

2.1 Hadronic contribution: space-like approach

In the time-like approach, a_μ^{HLO} can be written as Eq.1.26, where $\text{Im}\Pi_{had}$ is proportional to $\sigma_{had}(e^+e^-)$. By some mathematical manipulations [29, 33], the time-like equation can be transformed in a space-like integral:

$$a_\mu^{HLO} = \frac{\alpha}{\pi} \int_0^1 dx (x-1) \bar{\Pi}_{had}[t(x)], \quad (2.1)$$

where

$$\bar{\Pi}_{had}[t] = \Pi_{had}(t) - \Pi_{had}(0), \quad t(x) = \frac{x^2 m_\mu^2}{1-x} < 0, \quad (2.2)$$

$t(x)$ is the space-like four-momentum transfer.

It is possible to express the shift of the coupling constant $\Delta\alpha(q^2)$ in Eq.1.13 such that:

$$\Delta\alpha(q^2) = -\text{Re}(\bar{\Pi}(q^2)) = -\text{Re}(\bar{\Pi}_{lep}(q^2)) - \text{Re}(\bar{\Pi}_{had}(q^2)). \quad (2.3)$$

In the space-like region of momenta, $q^2 < 0$, resulting in having $\text{Im}(\bar{\Pi}(q^2)) = 0$. Therefore:

$$\bar{\Pi}_{had}(q^2) = \text{Re}(\bar{\Pi}_{had}(q^2)) = -\Delta\alpha_{had}(q^2) \quad (2.4)$$

and Eq.2.1 becomes [33]:

$$a_\mu^{HLO} = \frac{\alpha}{\pi} \int_0^1 dx (1-x) \Delta\alpha_{had}[t(x)], \quad (2.5)$$

where $(1-x)$ is the LO kernel. This allows to calculate the leading hadronic contribution to the muon anomaly through a direct measurement of $\Delta\alpha_{had}(t)$. The hadronic shift cannot be calculated in perturbation theory as it involves QCD contributions at low energy scales. However, at LO its expression can be determined starting from the effective coupling

$$\alpha(t) = \frac{\alpha}{1 - \Delta\alpha(t)} = \frac{\alpha}{1 - \Delta\alpha_{lep}(t) - \Delta\alpha_{had}(t)} \quad (2.6)$$

giving as a result

$$\Delta\alpha_{had}(t) = 1 - \Delta\alpha_{lep}(t) - \frac{\alpha}{\alpha(t)} \quad (2.7)$$

The leptonic contribution can be calculated in perturbation theory, thus it is possible to subtract it in order to get the hadronic one. This is not true anymore at higher order calculations, resulting in a more complex expression which needs the implementation of Monte Carlo simulations.

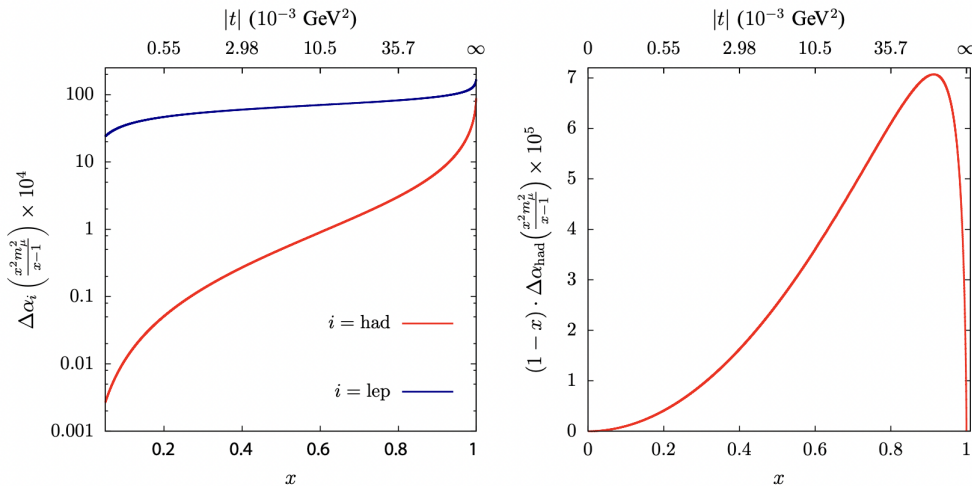


Figure 2.1: Leptonic and hadronic contribution to the running of α_{QED} on the left as a function of x and the integrand $(1-x)\Delta\alpha_{had}[t(x)]$ as a function of x and t on the right [30].

The change from annihilation (s-channel) to scattering (t-channel) process simplifies the evaluation of the anomaly [30]. While the time-like integration of Eq.1.28 is affected by fluctuations of $R_{had}^{data}(s)$, the hadronic contribution to the effective coupling is a smooth

function of the variable x , free of any resonance poles as shown in the left plot of Fig.(2.1), and this simplifies the evaluation of the integral. The range of the integration variable x from 0 to 1 corresponds to momentum transfer t going respectively from 0 to $-\infty$. The integrand in Eq.2.5 is shown as a function of the variable x in the right plot of Fig. 2.1. It peaks at $x_{peak} \approx 0.914$, corresponding to a momentum transfer $t_{peak} \approx -0.108 \text{ GeV}^2$, where $\Delta\alpha_{had}(t_{peak}) \approx 7.86 \times 10^{-4}$. An important advantage of the MUonE (space-like) approach is that all the experimental input necessary to estimate the muon anomaly can be obtained by a single scattering experiment. Thus, the space-like approach is not affected by the systematic uncertainties due to handling data from different experiments, which is one of the main limitation of the time-like approach.

This new method, involving the dispersive integral in the space-like region, is at the base of the MUonE project and is described in the next section.

2.2 Experimental proposal

The MUonE experiment proposal aims to achieve a very precise and independent measurement of a_μ^{HLO} through a novel approach based on the evaluation of the dispersive integral in the space-like region of momenta, Eq.2.5 [29, 30]. This can be obtained from the direct measurement of the running QED coupling in the space-like region, from the shape of the differential cross section for the μe elastic scattering cross section, with a unprecedented precision. Until now very few such measurements have been made, the most precise one was obtained by the OPAL experiment [34], from small-angle Bhabha scattering at LEP, which reached the first direct evidence for the hadronic contribution. But there there would be some intrinsic limitations related choosing the Bhabha process for the application of the proposed method, as the mixing of s and t channels which complicates the extraction of $\Delta\alpha_{had}(t)$ from data, limiting the accuracy on a_μ^{HLO} . MUonE proposes to exploit the t -channel $\mu - e$ elastic scattering cross section at low energy, overcoming some difficulties concerning Bhabha scattering physics. For this measurement, the 160 GeV M2 muon beam at CERN North Area will be used. The reasons why it is an extremely appealing proposal are listed in the following points [30]:

1. Differently from Bhabha scattering, it is a pure t -channel process, where the dependence on t of the differential cross section is proportional to $|\alpha(t)/\alpha|^2$:

$$\frac{d\sigma}{dt} = \frac{d\sigma^0}{dt} \left| \frac{\alpha(t)}{\alpha} \right|^2, \quad (2.8)$$

enabling an easier extraction of the running $\alpha(t)$;

2. The highly energetic muons from CERN M2 beam allow to access the region of the peak of the integrand function (Eq.2.5) shown in Fig.(2.1);

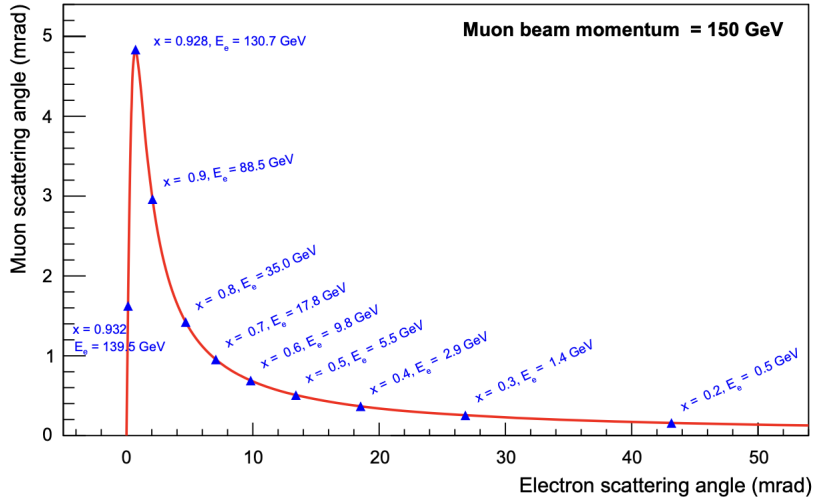


Figure 2.2: Correlation plot of the scattering angles of muons and electrons from elastic scattering events given a 150 GeV muon beam.

3. The boosted kinematics of the collision guarantees the containment of all the events in a single homogeneous detector, as the angular deflection stays within a 50 mrad cone;
4. The kinematics of the elastic scattering is well known and determined by angular observables. This permits to identify the signal region through the correlation of muon and electron scattering angles, shown in Fig.(2.2). It is evident from that picture that for $\theta_e < 5$ mrad there is an ambiguity region where $\theta_e \sim \theta_\mu$ and which needs to be treated carefully in order to have the right μ/e identification.

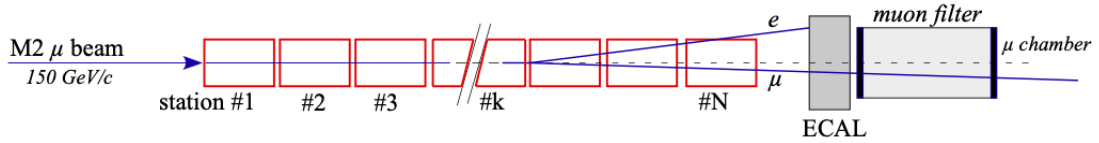


Figure 2.3: Schematic view of the MUonE apparatus.

The proposed experimental apparatus [31] to measure the elastic scattering process consists of a sequence of 40 identical tracking stations, followed by an electromagnetic calorimeter and a muon filter, as drawn in Fig. 2.3. Each station is composed by one target of low-Z material (beryllium or graphite) and six modules with silicon strip sensors, for a total level arm of ~ 1 m and transverse dimensions of $\sim 10 \times 10$ cm². The main role of the ECAL and muon filter is particle identification. The first may also help

in rejecting background events, while the second can control the contamination of pions in the M2 muon beam at CERN. Beam muons are almost unaffected by the upstream detector material, except for a small energy loss, so every station behaves as an independent detector. The events occurring at a given station have the incoming muon direction measured by the preceding station. The average beam intensity for energies at 160 GeV is of $\sim 1 - 2 \times 10^7$ muons/s. Assuming 3 years of data taking and a running time of $\Delta t_0 \sim 4 \times 10^7$ s/year, the integrated luminosity is of $\sim 1.5 \times 10^7$ nb $^{-1}$. This permits the collection of the statistics required to achieve the aimed accuracy for MUonE.

2.2.1 Precision requested for the measurement

In order to have this new space-like determination of a_μ^{HLO} competitive with the present time-like and LQCD approaches, the challenge of the experiment is to achieve a statistical and systematic uncertainty in the measurement of the μe differential cross section at the level of 10ppm. A competitive determination requires a precision of the order of 10^{-2} in measuring the hadronic running, which has an effect at the 10^{-3} level. This, in turn, translates to a precision of 10^{-5} in the shape of the differential cross section.

The aimed accuracy requires an excellent control of many effects:

1. on the theoretical side, the effect of radiative corrections to the μe cross section, which requires NLO and NNLO calculations. In order to extract with high precision $\Delta\alpha_{had}(t)$, a Monte Carlo code accurate to the NNLO level must be available;
2. on the experimental side, there are several aspects which need to be taken into account:
 - (a) detector resolution which is a fundamental parameter for elastic selection, but also for signal/background discrimination. The main background is pair-production on nuclei going into electron and positron pairs $\mu+N \rightarrow \mu+e^++e^-$;
 - (b) the control of multiple Coulomb scattering effects which break the muon-electron angular correlation of Fig(2.2) and their planarity;
 - (c) uniformity of sensors efficiency;
 - (d) tracker alignment and the knowledge of the longitudinal distances of the tracking stations;
 - (e) the knowledge of the mean energy of the beam, which affects the elastic angular correlation curve.

All these aspects will be discussed in the following sections of this chapter.

2.3 $\mu - e$ scattering theory

Elastic $\mu - e$ scattering process in Fig.(2.4) is represented by

$$\mu^\pm(p_1)e^-(p_2) \rightarrow \mu^\pm(p_3)e^-(p_4) \quad (2.9)$$

where p_1, p_2 and p_3, p_4 are the 4-momenta respectively of the initial and final state particles. In a fixed target experiment, the electron is initially at rest, thus in the

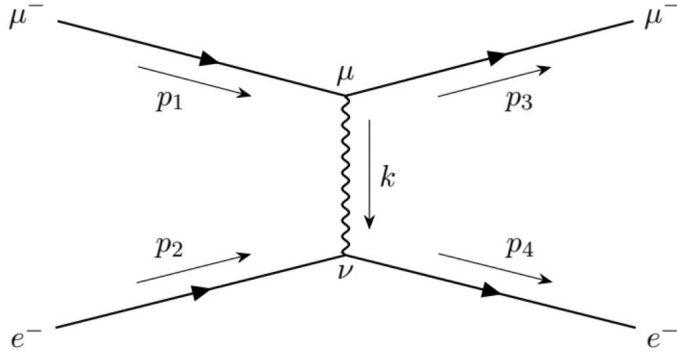


Figure 2.4: Feynman diagram for $\mu - e$ elastic scattering process.

laboratory system (LAB) Mandelstam variables s and t are defined as

$$\begin{aligned} s &= (p_1 + p_2)^2 = (p_3 + p_4)^2 = m_\mu^2 + m_e^2 + 2m_e E_\mu, \\ t &= (p_2 - p_4)^2 = (p_1 - p_3)^2 = 2m_e^2 - 2m_e E_e, \\ s + t + u &= 2m_\mu^2 + 2m_e^2. \end{aligned} \quad (2.10)$$

For any given value of the incoming muon momentum, there exists a maximum four-momentum transfer $q_{max}^2 = -t_{min}$:

$$t_{min} = -\frac{\lambda(s, m_\mu^2, m_e^2)}{s} \quad (2.11)$$

where $\lambda(a, b, c)$ is the Källén function defined as

$$\lambda(a, b, c) = a^2 + b^2 + c^2 - 2ab - 2ac - 2bc. \quad (2.12)$$

Given the M2 CERN muon beam, at a reference value $E_\mu = 150\text{GeV}$ it is found

$$t_{min} = -(380\text{MeV})^2. \quad (2.13)$$

The parameters for the Lorentz transformation between LAB and center-of-mass (CM) frame are

$$\begin{aligned} \gamma &= \frac{E_\mu + m_e}{\sqrt{s}}, \\ \beta &= \frac{p_\mu}{E_\mu + m_e}; \end{aligned} \quad (2.14)$$

The CM energy corresponding to the muon beam energy is $\sqrt{s} \sim 0.405541\text{GeV}$ and the Lorentz γ factor $\gamma \sim 370$.

The elasticity condition which relates the scattering angles θ_e and θ_μ in the LAB frame results to be

$$\theta_\mu(\theta_e) = \arcsin \left\{ \sin \theta_e \sqrt{\frac{E_e^2(\theta_e) - m_e^2}{[E_\mu + m_e - E_e(\theta_e)]^2 - m_\mu^2}} \right\}, \quad (2.15)$$

where $E_e(\theta_e)$ is the final energy of the electron, given the reconstructed θ_e

$$E_e(\theta_e) = m_e \frac{1 + \beta^2 \cos^2 \theta_e}{1 - \beta^2 \cos^2 \theta_e}, \quad \cos \theta_e = \frac{1}{\beta} \sqrt{\frac{E_e - m_e}{E_e + m_e}}. \quad (2.16)$$

The elasticity curve in Fig.(2.2) is Eq.2.15 in the $\theta_e - \theta_\mu$ plane and it is the fundamental constraint for MUonE to allow the discrimination of elastic scattering events from background processes.

Given that the incident muon has higher mass than the struck electron, the elastic scattering kinematics gives a maximum scattering angle for the muon:

$$\sin \theta_\mu^{max} = \frac{m_\mu}{m_e} \rightarrow \theta_\mu^{max} = 4.8 \text{ mrad}, \quad (2.17)$$

while the recoiling electron can be emitted at larger angles according to its energy, i.e. $0 \leq \theta_e \leq \sim 32 \text{ mrad}$ for electron energies $E_e' > 1 \text{ GeV}$. Therefore, when both scattering angles are lower than $\sim 5 \text{ mrad}$ there is an ambiguity between muon and electron which must be resolved with μ/e discrimination.

2.3.1 Elastic differential cross section

The LO QED prediction for the elastic differential cross section is:

$$\frac{d\sigma_0}{dt} = \frac{4\pi\alpha^2}{t^2\lambda(s, m_\mu^2, m_e^2)} \left[(s - m_\mu^2 - m_e^2)^2 + st + \frac{t^2}{2} \right] \quad (2.18)$$

where α is the fine-structure constant and $\lambda(a, b, c)$ is defined in Eq.2.12.

This expression is valid both for positive and negative muons. But the LO level is not enough for the aimed 10 ppm precision, NLO and NNLO corrections need to be considered. The needed theoretical calculation has to include higher orders:

$$\begin{aligned} \sigma(\mu^+ + e^- \rightarrow \mu^+ + e^-) \simeq & LO(QED) + LO(EW) + \\ & + NLO(QED) + NLO(HAD) + NLO(EW) + \\ & + NNLO(QED) + NNLO(HAD) + NNLO(EW) \end{aligned} \quad (2.19)$$

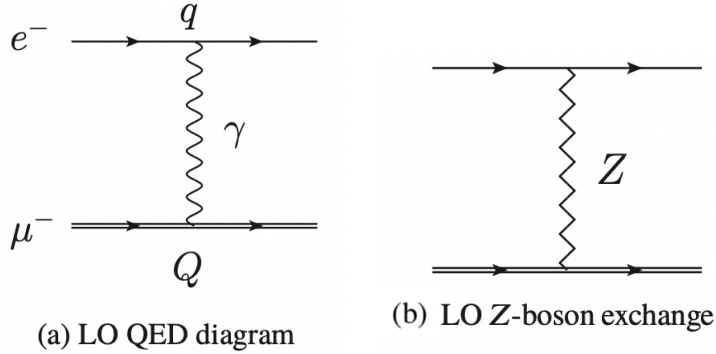


Figure 2.5: LO contributions from QED, HVP and the Z-boson exchange [35].

At LO in QED there is just the single diagram with a t-channel photon exchange as shown in Fig. 2.5(a) and it refers to the Born cross section in Eq.2.18. Electroweak contributions due to the exchange of Z boson (Fig. 2.5(b)) are strongly suppressed because of the large mass M_z , however the $\gamma - Z$ interference can not be neglected, as their suppression is of the order of 10^{-5} .

Higher order calculations are available in the form of MC codes for numerical integrations or fully exclusive event generators [35]. In this thesis work the MESMER Monte Carlo generator [36, 37, 38] has been used.

The full NLO QED and one-loop EW corrections have been computed exactly and implemented in the fully exclusive MC generator MESMER [36].

NLO(HAD) is the term given by the hadronic vacuum polarization insertion in the

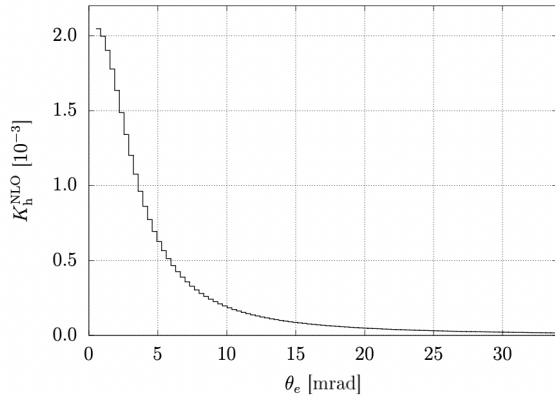


Figure 2.6: The relative importance of the HVP term at NLO in $\mu - e$ scattering as a function of θ_e [35].

photon propagator that we intend to extract. The impact of the hadronic contribution at NLO is shown in Fig. 2.6 as a function of θ_e . The plotted NLO K factor is defined as [35]

$$K_h^{NLO} = \frac{d\sigma^{NLO}}{d\theta_e} / \frac{d\sigma^0}{d\theta_e}. \quad (2.20)$$

It can be observed that the hadronic contribution is larger at small θ_e , whereas for $\theta_e > 20$ mrad it is strongly suppressed.

The NLO cross section can be written as the sum of the $2 \rightarrow 2$ process, including LO and one-loop virtual corrections, and the $2 \rightarrow 3$ real photon emission:

$$d\sigma_{NLO} = d\sigma_{\mu e \rightarrow \mu e} + d\sigma_{\mu e \rightarrow \mu e \gamma}. \quad (2.21)$$

The dependence of the observable signal for the hadronic running of α from NLO radiative corrections has been studied in [36] by considering the following ratios:

$$R_i = \frac{d\sigma_i(\Delta\alpha_{had}(t) \neq 0)}{d\sigma_i(\Delta\alpha_{had}(t) = 0)}, \quad \text{with } i = \text{LO, NLO}. \quad (2.22)$$

They represent the ratio of a given cross section including the contribution of $\Delta\alpha_{had}(t)$ to the running of α and the same cross section with the contribution switched off. Therefore they display the sensitivity of a given observable (e.g. scattering angles) to the signal of interest.

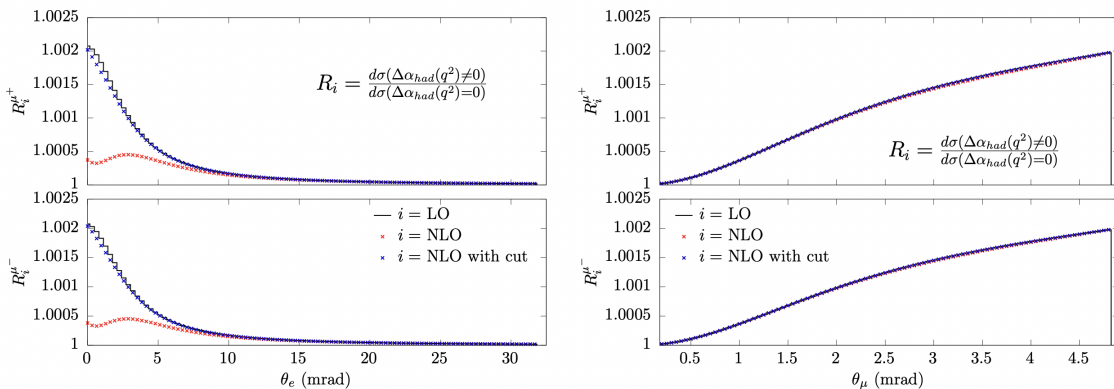


Figure 2.7: Ratios R_i are shown for the process $\mu^+e \rightarrow \mu^+e$ (top) and $\mu^-e \rightarrow \mu^-e$ (bottom) as a function of the electron (left) and muon (right) scattering angle [35].

Fig. 2.7 shows the ratio as a function of the observables θ_μ , θ_e at the LO and NLO. Focusing on $R_i(\theta_e)$, the elastic signal at low θ_e , visible in the blue peak, is washed out by photon radiation effects at NLO, visible in the almost flat red line of crosses. In the study it has been highlighted that the sensitivity to the hadronic correction can be recovered by the application of an elastic selection (e.g. requiring the planarity between scattered leptons: acoplanarity cut $|\pi - (\phi_e - \phi_\mu)| < 3.5$ mrad), as shown from the 2D plot in Fig. 2.8. This selection removes radiative events. The improvement is clear from the blue points which mostly overlap the elastic curve both in Fig. 2.7 and 2.8. This is particularly important for the electron, which is more affected by photon radiation, while the distribution as a function of the muon angle is robust against those effects, as

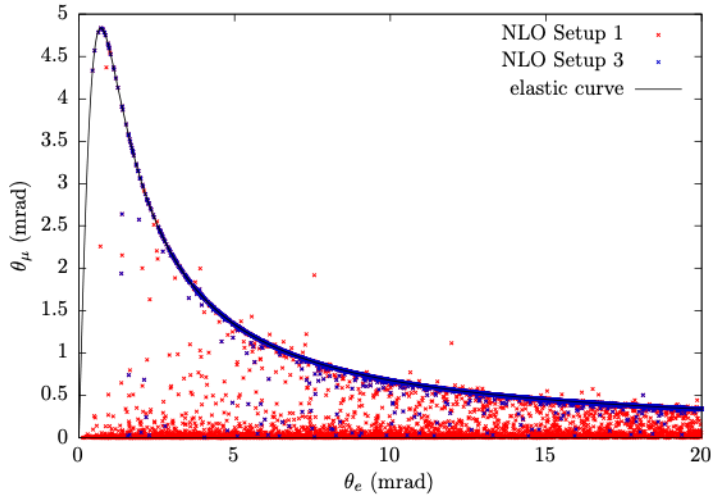


Figure 2.8: The correlation between the electron and muon scattering angle. The curve in blue represents the LO elastic curve and the dots are the NLO events, given two different selection criteria: setup 1 $\theta_e < 100$ mrad and $E_e > 0.2$ GeV (red); setup 3 the same as setup 1 with the addition of acoplanarity cut (blue). [36].

less affected by real photon emission.

The NNLO QED contributions have been evaluated and implemented in the MC generator MESMER [36, 37] and in the MC integrator McMULE [39]. The complete set of leptonic corrections to $\mu - e$ scattering consists of three parts, with contributions from virtual and real leptonic corrections:

$$d\sigma_{NNLO} = d\sigma_{virt} + d\sigma_{\gamma} + d\sigma_{real}. \quad (2.23)$$

They include:

- $d\sigma_{virt}$ virtual two-loop contribution, both factorisable and non-factorisable;
- $d\sigma_{\gamma}$ interplay between real photon radiation and leptonic loop insertion;
- $d\sigma_{real}$ tree-level amplitudes for the processes $\mu^{\pm}e^{-} \rightarrow \mu^{\pm}e^{-}l^{+}l^{-}$, with $l = e, \mu$. This process may contribute to the background in case two final-state tracks are lost and the event is reconstructed as a two-track event.

As it was happening at NLO, the corrections to $d\sigma/d\theta_e$ from NNLO QED can be mitigated by the introduction of an elastic selection including cuts on the acoplanarity and the distance of the two-track event from the elastic curve, as can be seen in Fig. 2.9. The process shown there is production of pairs from scattering on atomic electrons.

At the NNLO level, the hadronic contribution exhibits a complex evaluation, due to the presence of non factorizable hadronic loops. This latter contribution is of the order of $10^{-4} - 10^{-5}$ playing thus an important role in the MUonE data analysis. It was computed in [41, 42].

The main source of background is identified in the direct production of electron-positron pairs in the field of target nuclei. This may mimic an elastic process if one

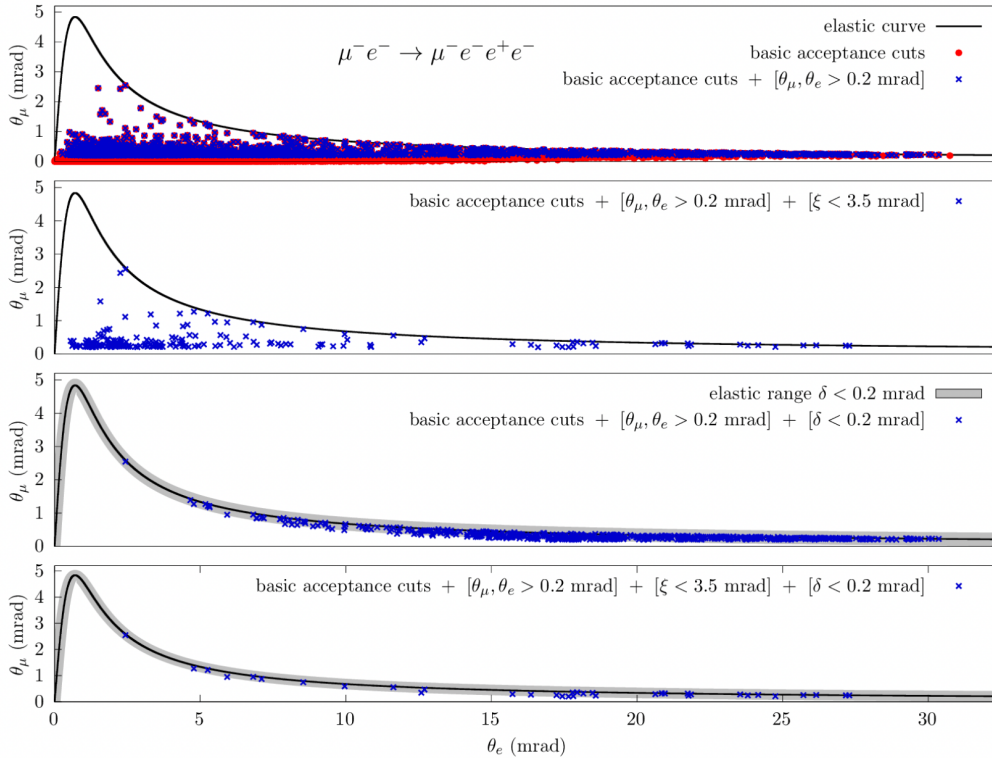


Figure 2.9: A series of cuts is applied, including cuts on the particle angles, the acoplanarity and the distance of the two-track event from the elastic curve [37].

of the outgoing leptons are emitted outside the detector acceptance. The contribution of this background is estimated to be of the order of 10^{-4} . A MC generator has been developed for the MUonE collaboration [40] and the double differential cross section of the process is shown in Fig. 2.10.

2.4 Extraction of $\Delta\alpha_{had}(t)$

The experimental workflow is articulated in precise steps:

1. commissioning of the detector in order to have good quality data (stable and reliable readout, good efficiencies of detection and reconstruction, good calibrations etc.);
2. a selection of signal events which helps in the rejection of background ones, suppression of radiative events and reduction of some detector effects;

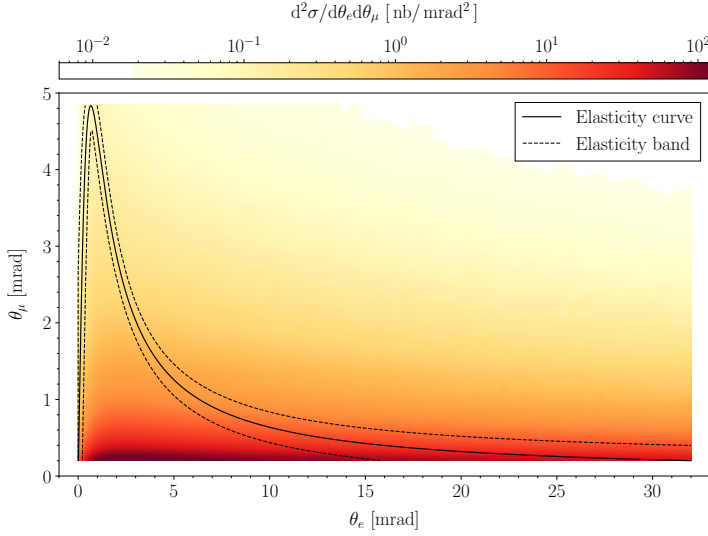


Figure 2.10: Double differential cross section $\mathbf{d}\sigma^2/\mathbf{d}\theta_e\mathbf{d}\theta_\mu$ for the lepton pair production in muon-nucleus scattering for two-tracks events. The elasticity curve is denoted by a black solid line, while the black dashed lines delimit the area where the events satisfy the elasticity [40].

3. precise measurement of the scattering angles of the outgoing muons and electrons (θ_e, θ_μ) to determine the shape of the double-differential cross section for elastic scattering;
4. extraction of $\Delta\alpha_{had}(t)$ from a template fit to the shape of the differential cross section;
5. evaluation of the hadronic vacuum polarization contribution a_μ^{HLO} through the master integral in Eq.2.5.

The suppression of physical and beam backgrounds is needed for determining the shape of the differential cross section, defined by the counting ratio $R(\theta_i)$:

$$R(\theta_i) = \frac{d\sigma_{data}(\Delta\alpha_{had}(t) \neq 0)/d\theta_i}{d\sigma_{MC}(\Delta\alpha_{had}(t) = 0)/d\theta_i} = \frac{dN_{data}(\Delta\alpha_{had}(t) \neq 0)/d\theta_i}{dN_{MC}(\Delta\alpha_{had}(t) = 0)/d\theta_i}. \quad (2.24)$$

In Eq.2.24, the observables θ_i are the scattering angles of the outgoing muon and electron ($i = e, \mu$) from the elastic scattering process, $d\sigma_{data}(\Delta\alpha_{had}(t) \neq 0)/d\theta_i$ and $dN_{data}(\Delta\alpha_{had}(t) \neq 0)/d\theta_i$ are respectively the differential cross section and the observed event yield of the elastic scattering, while $d\sigma_{MC}(\Delta\alpha_{had}(t) = 0)/d\theta_i$ and $dN_{MC}(\Delta\alpha_{had}(t) = 0)/d\theta_i$ are the corresponding MC predictions obtained with $\Delta\alpha(t) = \Delta\alpha_{lep}(t)$ where the hadronic running $\Delta\alpha_{had}(t)$ is switched off.

The hadronic contribution to the running $\Delta\alpha_{had}(t)$ will be extracted by a template fit to the ratio $R(\theta_i)$ in Eq.2.24 [31]. The used parametrization has two parameters, inspired by the one-loop QED calculation for the vacuum polarization induced by a lepton pair

in the space-like region:

$$\Delta\alpha_{had}(t) = k \left\{ -\frac{5}{9} - \frac{4M}{3t} + \left(\frac{4M^2}{3t^2} + \frac{M}{3t} - \frac{1}{6} \right) \frac{2}{\sqrt{1 - \frac{4M}{t}}} \log \left| \frac{1 - \sqrt{1 - \frac{4M}{t}}}{1 + \sqrt{1 - \frac{4M}{t}}} \right| \right\}. \quad (2.25)$$

This method consists in generating a grid of points (k, M) in the parameters space

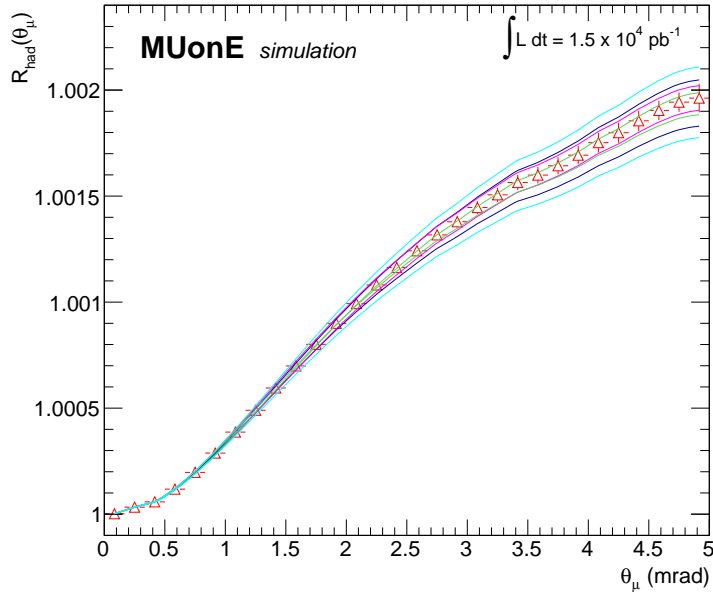


Figure 2.11: Central value of $R_{had}(\theta_\mu)$. The error bars correspond to the expected statistical uncertainties for the nominal MUonE luminosity of $1.5 \times 10^4 \text{pb}^{-1}$. The curves represent the representative MC templates [51].

covering a region of $\pm 5\sigma$ around the expected values, where σ is the expected uncertainty. For each pair of values, a template for R_{had} is obtained with the Monte Carlo generator (Fig. 2.11), which then is compared with data (pseudodata in MC) calculating:

$$\chi^2(K, M) = \sum_i \frac{R_i^{data} - R_i^{templ}(K, M)}{\sigma_i^{data}} \quad (2.26)$$

where $K = \frac{k}{M}$, and the minimum χ^2 is found by parabolic interpolation across the grid points. The fit can be done on the distribution of the muon or the electron scattering angle, as shown in Fig. 2.12, as well as on their two-dimensional distribution, which gives the most accurate result.

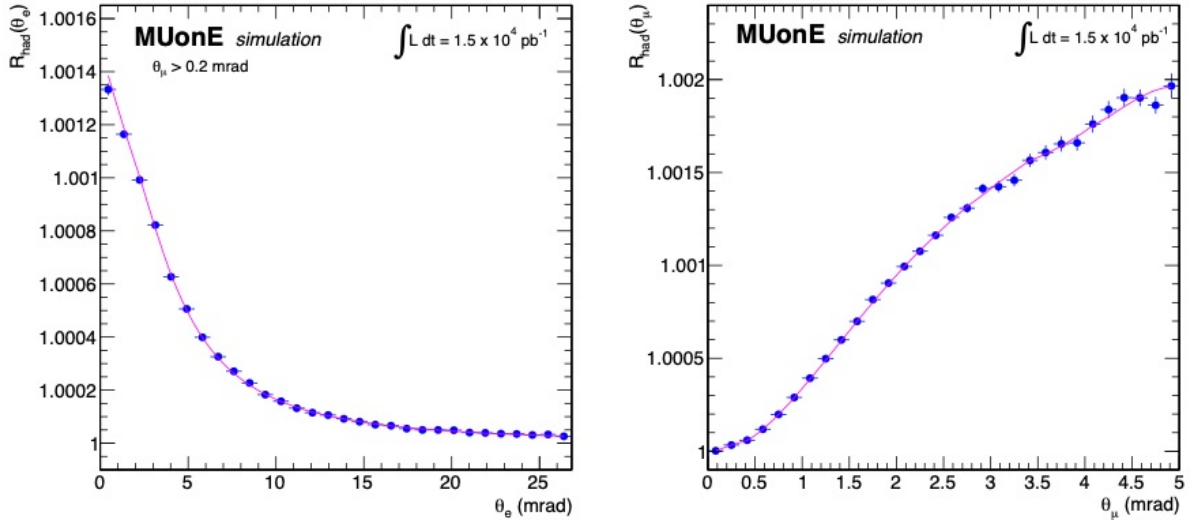


Figure 2.12: Example pseudodata showing the ratio R_{had} as function of electron (left) and muon (right) angular distributions. Entries correspond to the expected events for the nominal MUonE integrated luminosity. The template fit is superimposed [51].

2.5 Experimental apparatus

Muons from the M2 beam line impinge on the atomic electrons of beryllium or graphite targets. The apparatus is divided in:

1. tracking system;
2. electromagnetic calorimeter;
3. muon filter.

2.5.1 Tracking system

Several requirements are needed to perform the tracking:

1. maximize the coverage of the region of interest of the process having a uniform response from the detector;
2. minimize the multiple Coulomb scattering (MS) in order to reduce the smearing of particle tracks;
3. maximize data collection;
4. a good angular resolution.

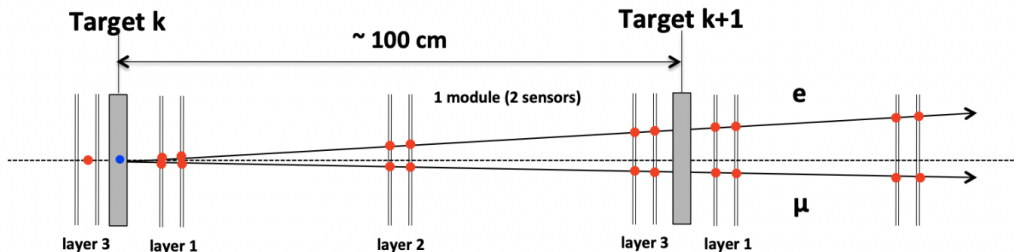


Figure 2.13: An overview of one station, composed by one target and six tracking modules. This is repeated 40 times in the final apparatus.

The basic unit of the tracking system is the single station, sketched in Fig. 2.13. Each station behaves as an independent detector, composed by one low- Z target and six silicon strip modules, named after their measurement coordinate: two X , two Y and two stereo modules (U and V), which are rotated of $\alpha = 45^\circ$ around Z axis. The stereo modules are meant in order to remove ambiguities during pattern recognition for tracks formation. The segmentation of the entire system has been thought in order to maximize the collection of data minimizing the effect of MS, as the total thickness of the target (~ 60 cm) is divided into 40 thin slabs each ~ 1.5 cm thick. In that way, the same muon beam can interact different times in different stations, increasing the collection of data. The tracking modules have been chosen to be the so-called 2S modules, foreseen for the upgrade of the CMS outer tracker for the high luminosity phase of LHC [43]. Each module is composed of two single-sided silicon micro-strip sensors with a thickness of $320 \mu\text{m}$ each, for an overall area of $10 \times 10 \text{ cm}^2$.

This large area allows to completely contain the relevant angular acceptance, up to a scattering angle of ~ 30 mrad, which, given the 160 GeV beam energy, corresponds to energy $E_e > 1$ GeV for the outgoing electron. Each sensor has a total of 1016 strips with $90 \mu\text{m}$ pitch, which are read out by eight CMS Binary Chips (CBC). The two strip sensors are separated by a 1.8 mm gap and have parallel strips reading the same coordinate. Hits from the two sensors are correlated by the CBC, forming the so-called stub, or track element. The chip provides a binary measurement, presence or absence of a hit. The data from the CBC are aggregated by a concentrator chip (CIC), which transmits the digital data to the lp-GBT [44]. While stereo modules are orthogonal to the Z -axis (beam direction), the X and Y ones are tilted of about 233 mrad (~ 15) deg.

This setting has been optimized after a detailed simulation study [45]. The single hit resolution of the modules is expected to change from about $90 \mu\text{m} / \sqrt{12} \simeq 26 \mu\text{m}$ (corresponding to the strip pitch) to about $10 \mu\text{m}$. The improvement is mainly due to charge sharing between adjacent strips. Tilt increases the fraction of tracks which produce signals in two adjacent strip from a few percent to 40 – 50%, depending on the

setting of the signal threshold. Tracks with a signal in two strips are measured with an improved spatial resolution, however it comes at the cost of a potential reduction in efficiency. This is due to the lowering of the energy deposition per strip, relative to the total, resulting a less favorable signal to noise ratio. Therefore this aspect requires a careful scrutiny.

An important parameter is the detector angular resolution, which is related to the single

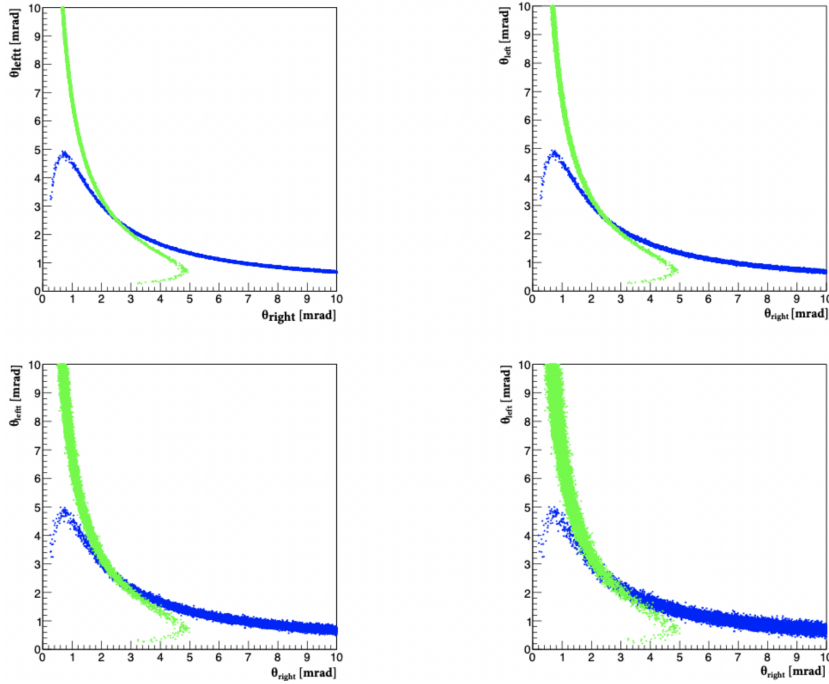


Figure 2.14: Distribution of the two measured scattering angles for events simulated with different angular resolution: (top-left) ideal angular resolution (only MS effect); (top-right) angular resolution of $20 \mu\text{rad}$; (bottom-left) angular resolution of $60 \mu\text{rad}$; (bottom-right) angular resolution of $100 \mu\text{rad}$. In blue the points with correct $\mu - e$ identification, in green the wrong identification [31].

hit resolution of the tracking planes. An angular resolution of $20 \mu\text{rad}$ corresponds to a spatial resolution of $20 \mu\text{m}$, which can be achieved with state-of-the-art silicon detectors. The angular resolution has an impact on the capability to identify the outgoing muon and electron tracks. There exists an ambiguity region where the two leptons may be misidentified and its extension is determined by the angular resolution. Fig. 2.14 shows the distribution of the two scattering angles θ_{left} and θ_{right} , defined with respect to an arbitrary axis without any identification, for different values of the intrinsic angular resolution. It can be noticed that the higher is the resolution, the wider will be the ambiguity region where $\theta_{\mu} \sim \theta_e$. This also highlights the fact that the tracking system

itself is not enough for a good particle identification (PID), for this aim the presence of an electromagnetic calorimeter (ECAL) and a muon detector could be of fundamental importance.

Stub finding logic The first step of the ‘stub finding logic’ is aimed at determining hits in both sensors separately. A hit corresponds to a cluster, namely a group of adjacent fired strips. The maximum size of the cluster can be set and for MUonE it is set to four. The CBC compares clusters found in the two matched sensors comprising the 2S module, respectively the seed and the correlation cluster, in a given window of acceptance, to find a correlation. The center of this window corresponds to the expected matched position of the seed cluster in the correlation layer. This value can be adjusted by setting a configurable offset within maximum ± 3 strips, to correct for geometrical effects. In addition, the width of the correlation window can be configured up to ± 7 strips around the center. The logic is represented in Fig. 2.15.

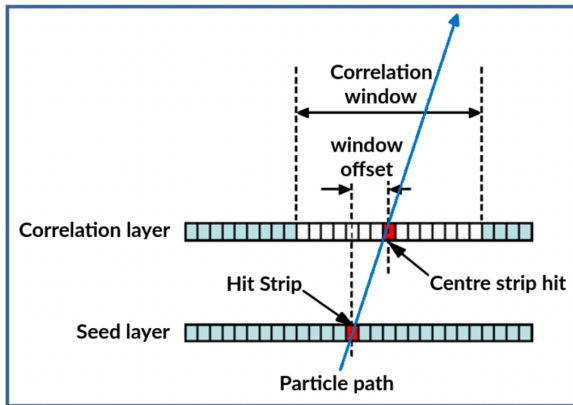


Figure 2.15: Sketch of stub formation logic, given the seed and correlation layers. The correlation window with its width and center is also shown.

Stub information combines the cluster position in the seed sensor, namely the stub address, and the lateral difference in strip units between the seed and correlation cluster. This latter quantity is called *bend*. It is defined as

$$bend = x_{correlation} - (x_{seed} + offset) \quad (2.27)$$

where offset represents the one used for the center of the correlation window. In the original application for the CMS upgraded tracker the 2S module is designed to trigger on high transverse momentum tracks. Stub position is then calculated as:

$$x_{stub} = x_{seed} + \frac{bend}{2}. \quad (2.28)$$

The bend is used to estimate their deflection in the strong CMS magnetic field [43]. There, it is used for triggering purposes.

2.5.2 Electromagnetic calorimeter



Figure 2.16: The prototype calorimeter, with the 25 $PbWO_4$ crystals and the APD (shown on top) for the readout.

The current setup of the electromagnetic calorimeter is based on the CMS one, composed of 25 crystals of $PbWO_4$. A picture is shown in Fig. 2.16. The scintillation light is read-out by APDs, while the front-end electronics is based on the multi-gain preamplifier (MGPA) chip [46]. A laser system is used for calibration and control of the overall system. The detector will be placed downstream of the last tracker station. The role of the ECAL in MUonE is mostly to use it as a control system for the tracker, helping in assessing the systematics. Some of the possible contributions are listed below [32, 47]:

1. an independent measurement of the electron energy;
2. e/μ PID. The association of ECAL energy cluster to a matched track, may help in resolving the kinematical ambiguity for small scattering angles (where $\theta_e \sim \theta_\mu$);
3. direct identification of radiative or background events, which break the perfect correlation between the muon and electron angle;
4. systematic studies.

The energy resolution is $\sigma(E)/E \sim 1\%$ above 100 GeV and position resolution less than ~ 1 mm for the reconstructed electron impact point.

A fast simulation has been developed based on the GFLASH parametrization used in CMS [48, 49]. It has been used to study the behaviour of the ECAL and its capability of selecting a clean sample of elastic events [50].

During last years beam tests have been carried out to characterize the detector response the detector. The commissioning of the present ECAL is not yet complete. Further work needs to be done to improve the analysis methods and evaluate the impact on the MUonE measurement systematics.

2.5.3 Muon filter

A muon detector is foreseen to measure and identify muons from elastic event. It will be placed after the ECAL, behind an iron shield. This will allow to identify muons, discarding possible pions contamination of the beam, and to measure the trajectories of muons from elastic events, distinguishing them from pileup beam muon.

This detector is still under development, however the layout should contain a few detector layers, providing spatial measurement, a shielding layer to absorb background hadrons and shower tails leaking out of the calorimeter. A relatively simple system is envisaged based on the same 2S-modules used for the tracking stations. Monte Carlo studies are under way to optimize the design, a possible sketch of the detector is reported in Fig. 2.17.

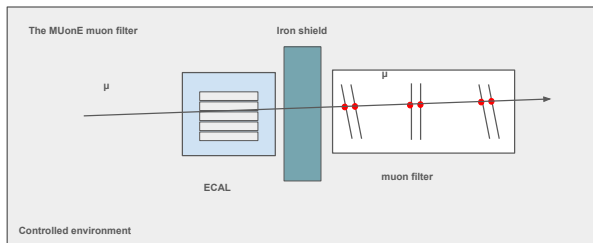


Figure 2.17: Schematic diagram of the muon filter layout. Distances between filter elements will be determined by simulation.

Chapter 3

Simulation and reconstruction tools

3.1 FairMUonE software

The full simulation for MUonE relies on a combination of specialized MC generators that produce interaction vertices for both the signal and the main background, as well as the Geant4 toolkit, which simulates the passage of particles through matter. This setup allows for the simulation of a particle beam with specified momentum and position distributions, typically provided by the M2 beam experts.

The needed high precision necessitates a theoretical simulation of the $\mu^+e^- \rightarrow \mu^+e^-$ scattering process at least at the next-to-next-to-leading order (NNLO). This has been accomplished with the current MESMER generator, as discussed in Section 2.3.1. In addition, to investigate the main source of background, a dedicated generator is needed for lepton pair production from muon scattering on target nuclei, specifically $\mu^+N \rightarrow \mu^+Nl^+l^-$, where electron and positron production has the highest probability[40].

Simulation, together with software for event reconstruction and detector alignment, are integrated in a dedicated package called FairMUonE. It is based on the FairRoot experimental environment [52], that makes use of external packages (like Geant4 [53] and ROOT [54]) provided by the FairSoft framework.

3.1.1 Simulation

As previously mentioned, the FairMUonE simulation combines MC generators with Geant4. While the generators handle specific interactions for each beam muon, Geant4 allows for the generation of what is known as *minimum bias* events. This approach enables the creation of samples including all possible interaction types, with probabilities determined by their respective cross sections. Geant4 minimum bias simulation was very useful for some background studies, before the development of the dedicated

pair-production MC generator.

Interaction of high-energy muons in matter includes several processes:

- direct production of lepton pairs, both on nuclei and atomic electrons:

$$\begin{aligned} \mu N &\rightarrow \mu N l^+ l^- \quad l = e, \mu \quad (\text{mainly } e^\pm); \\ \mu e^- &\rightarrow \mu e^- l^+ l^- \quad l = e, \mu \quad (\text{mainly } e^\pm); \end{aligned} \quad (3.1)$$

- bremsstrahlung, both on nuclei and atomic electrons:

$$\mu N \rightarrow \mu N \gamma \quad \mu e^- \rightarrow \mu e^- \gamma; \quad (3.2)$$

- inelastic interactions with nuclei:

$$\mu N \rightarrow \mu X. \quad (3.3)$$

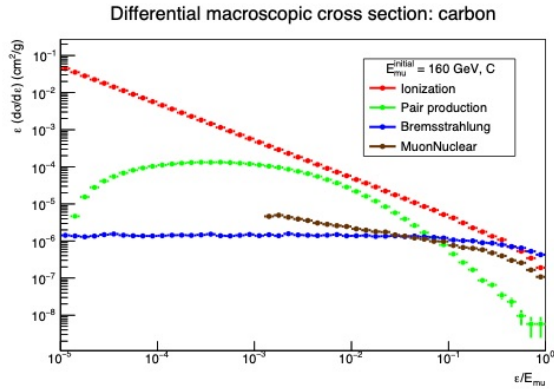


Figure 3.1: Macroscopic differential cross sections of muons with $E_\mu = 160$ GeV in carbon as a function of the relative energy transfer [55].

Fig. 3.1 shows the macroscopic differential cross sections in beryllium for the three background processes as a function of the relative energy transfer ϵ/E_μ , where ϵ is the energy transferred by the incoming muon and E_μ is its initial energy. The processes have been simulated with Geant4.

In the M2 beam line, the rate is of 40 MHz (25 ns) and beam intensity can reach 50 MHz. Given these numbers, the Poisson distribution predicts, with a certain probability, the occurrence of 2, 3, 4, etc. pileup muons. Therefore, there is the need of simulate beam pileup that can occur simultaneously within an elastic event.

MESMER generators MESMER generators integrated in FairMUonE give the possibility to study specific interactions, as the elastic scattering $\mu^+ e^- \rightarrow \mu^+ e^-$ and the pair production on nuclei $\mu^+ N \rightarrow \mu^+ N l^- l^+$, in a full simulation of the detector, provided by the integration of Geant4 in the software. The interaction is forced to happen in the target for every beam muon. Dealing with the MESMER signal generator, many aspects can be deeply studied. Some examples are listed below:

- kinematics and topologies of elastic events with a full simulation of the detector;
- reconstruction efficiency and angular resolutions as a function of specific reconstruction configurations;
- efficiency and optimization of elastic selection criteria;
- effects of some of the most important systematics (e.g. knowledge of the beam energy, MS, misalignment).

MESMER background has been designed to achieve a more accurate description of pair production on nuclei. Geant4 includes this type of interaction, however with some limitations; for example, the scattering angle of the muon after the interaction with nuclei is not accurately simulated. In addition, this tool is crucial for assessing the level of background that remains after applying various elastic cuts.

Minimum bias for background studies Geant4 minimum bias is a valuable tool for generating samples that include both signal and background events, with a realistic probability based on the cross sections, without any forced interaction. One of its main drawbacks, however, is that it generally requires more time to produce a sample with sufficient statistics compared to standalone generators as MESMER. Nevertheless, this tool is crucial to perform cross-checks with results obtained from specific event generators. Some studies have been done in this direction, in particular to study the background level after a simple elastic selection (Appendix 3.1.1) or some cross section measurement of different processes as shown in Fig. 3.1.

3.1.2 Event reconstruction

The event reconstruction stage in FairMUonE utilizes as inputs the tracker hits (or *stubs*) either in real data or in simulated events. The simulated stubs are generated during the digitization stage, which aims to replicate the digital readout from the front-end electronics of the 2S modules. Once the inputs are established, a reconstruction algorithm is applied. The first step involves pattern recognition, which is designed to create 2D track candidates in the XZ and YZ projections. This collection of 2D track candidates is obtained by pairing hits from the X and Y modules located at the start and end of each tracking station.

In certain kinematic configuration, the angular separation between the two tracks may be small in one or the other projection $\Delta\theta_{xz}$ or $\Delta\theta_{yz}$, thus those might share one or more stubs. The reconstruction algorithm permits hit sharing by adjusting a parameter known as the *number of hits shared*, which can reasonably range from zero to two. The combination of 3D tracks is achieved by associating U and V stubs. The 45° rotation around the Z axis of these stereo modules facilitates accurate matching of the XZ and

YZ projections, thereby resolving ambiguities. For each combination of 2D tracks, the algorithm searches for the nearest stereo hit within a specified search window (3mm distance between track and stereo hit). The distance between the position of the stereo hit u_{hit} and the combined track is calculated from the expected hit position along the track, which is defined by the two 2D lines:

$$x(z) = m_x \cdot z + q_x \quad (3.4)$$

$$y(z) = m_y \cdot z + q_y, \quad (3.5)$$

The latter position is projected onto the measurement direction determined by the module's rotation angle α , having as a result the distance:

$$d(\text{hit}, \text{track}) = |u_{\text{hit}} - (x(z_{\text{hit}}) \cdot \cos \alpha + y(z_{\text{hit}}) \cdot \sin \alpha)|. \quad (3.6)$$

The chosen stereo hit is included in the set of hits for the specified combination of 2D projections. The 3D track is then fitted using these points with a χ^2 minimization approach:

$$\chi^2 = \sum_{\text{hits}} \frac{[d(\text{hit}, \text{track})]^2}{\sigma_{\text{hit}}^2}, \quad (3.7)$$

where σ_{hit} is the measurement uncertainty of the module where the hit was recorded. The signature of an elastic event is characterized by two outgoing tracks - one for μ^+ and one for e^- - originating from a common vertex that is consistent with the target. Vertex candidates are created by matching the two candidate outgoing tracks with a single reconstructed track in the previous station. The vertex location is estimated by identifying a position that minimizes the sum of distances of closest approach to each of the three tracks. For this triplet of tracks, a specialized kinematic vertex fit is performed. The uncertainties of the hits associated with the track exhibiting the larger scattering angle are estimated including the expected multiple scattering (MS) from the target material and from the traversed modules. The fit is based on a constrained least square method, using the 3D line slopes of the three tracks as well as the x , y vertex positions as free parameters. The z position is estimated through the distance of closest approach (DOCA) method. The three tracks that define the vertex are then re-fitted with the additional condition of passing through the same (x, y, z) position. All the reconstructed vertices are stored and sorted by their normalized χ^2 .

3.1.3 Alignment

The alignment step is necessary to determine the real detector geometry, that is the corrections to be applied to the ideal positions and orientations of each module in every tracking station. This process relies on track fitting. Currently, a simplified alignment is available for the experiment. It is an iterative procedure based on the correction

of the positions and orientations through alignment parameters u_{offset}^i and α_{offset}^i , for each i -th module. The implementation now provides u_{offset}^i for the shift along the local measurement direction, while α_{offset}^i for the rotation around the beam axis. The remaining two rotations are fixed to their nominal values, while the module positions along the beam axis are determined by the laser metrology measurements. In addition, a possible shift along the direction orthogonal to the measured one does not affect directly the track, and is neglected.

The algorithm starts from a clean sample of events containing just one stub per module. These are single muon events, and this selection helps eliminating ambiguities caused by noise stubs or multiple muons passing through the detector simultaneously. The process begins by reconstructing the selected events, either by assuming the ideal geometry or by incorporating external input (such as metrology measurements) to establish initial values for the alignment parameters. These are determined by numerical minimization of the following χ^2 :

$$\chi_{\text{align}, i}^2 = \sum_{\text{tracks}} \chi_{\text{track}}^2(u_{\text{offset}}^i, \alpha_{\text{offset}}^i) \quad (3.8)$$

Here, χ_{track}^2 is the χ^2 of the single tracks defined in Eq. 3.7, where the residuals in Eq. 3.6 are modified by applying the substitutions $u_{\text{hit}} \rightarrow u_{\text{hit}} + u_{\text{offset}}^i$, $\alpha \rightarrow \alpha + \alpha_{\text{offset}}^i$.

The minimization is carried out separately for each module. In this step, the parameters for the other modules are fixed to the estimates used in the previous iteration. Once the χ_{align}^2 has been minimized for all the modules, the resulting alignment parameters are used to perform a new track reconstruction, and the procedure is repeated iteratively until convergence of all the alignment parameters.

This procedure can be used to align the modules internally in each station, or to align multiple stations at the same time by using all their modules to reconstruct the same track.

Further improvements are foreseen for the local alignment, and they will be discussed in next Chapters. While a global alignment based on the minimization of a global χ^2 including all the parameters is under development for future tests.

3.2 Reconstruction performance

Evaluating the physics performance of the MUonE setup, depending on its design and the reconstruction algorithm has been an essential part of the work. This involved developing and testing various versions of the FairMUonE software and exploring different configurations. A key focus was the analysis of the reconstruction efficiency on MC generated events, and in addition the angular resolution of the reconstructed electron and muon tracks. This study is crucial for understanding the performance of the reconstruction algorithms and improving the accuracy in future analyses. The reconstruction algorithm can be tuned by means of a set of configuration parameters, foreseen in order to establish

the optimal running configuration. Among them, the most important one defines the maximum number of hits that can be shared between two reconstructed tracks. Another important configuration parameter allows to vary the accuracy in modeling the effects of the multiple scattering in the track reconstruction. In order to evaluate the effects of these changes and the differences between several releases, the reconstruction step on a given generated sample needs to be run for all the different versions and configurations. This may take significant cpu-time, thus, in order to speed up the procedure, a pipeline that parallelizes different steps of the tests and validations has been developed, based on the Snakemake tool [56]. More details are given in Appendix A.

3.2.1 Reconstruction efficiencies

The efficiency of the FairMUonE reconstruction algorithm has been analyzed across various simulated data samples and configurations. It has to be as uniform as possible all over the entire allowed kinematic region. The setup used for these studies consists of 2 tracking stations with a graphite target of 3 cm inserted in the second station, in the upstream side. The incoming muon is simulated with a beam profile determined by the SPS accelerator experts [32]. For the present study, six MC samples of elastic events have been generated with MESMER, corresponding to different θ_e intervals. The entire interval spans the geometrical acceptance covered by the tracking stations, from 0 to 32 mrad. The samples are normalized to the corresponding values of the cross section, which are returned by the generator.

As a first step, the reconstruction efficiencies have been evaluated separately for the two particles. Subsequently, the efficiencies for the entire elastic event have been assessed, where it has been requested that both particles' tracks are reconstructed. As already mentioned, for given topologies it may happen that two outgoing particles could hit a detection module closely or even overlap, resulting in only one stub being generated. For that reason, one of the main reconstruction parameters to tune is the *maximum number of shared hits* (n_{shared}^{max}) between two tracks, which defines how many stubs two tracks can share. Therefore, the efficiencies have been studied as a function of this parameter, which was set to 0, 1, and 2. Sharing more than one hit can lead to the formation of clone tracks, namely multiple reconstructed tracks associated with the same MC track. It is important to quantify the level of clones production as a function of the hit sharing parameter and to check if the tracks selected for the event vertex are the best ones within all the clones. Therefore a quality criterion needs to be defined. Table 3.1 presents the percentages of reconstructed events with and without clones as a function of the hit sharing parameter:

As one might anticipate, the proportion of events with clones increases with the number of shared hits. Ensuring that the vertexing algorithm selects the optimal electron

n_{shared}^{max}	$1\mu + 1e$ (no clones)	events with clones
0	92.28%	0.02%
1	98.70%	0.30%
2	91.50%	8.41%

Table 3.1: Fraction of events without (2nd column) or with (3rd column) clones as a function of the maximum number of hits shared.

and muon tracks among all clones is of paramount importance. A quality variable of reconstructed tracks can be defined from the MC truth as the fraction of the number of hits in the track which are linked to the associated MC particle. If the fraction of associated hits is $\geq 65\%$, it means that the reconstructed track shares at least 4 hits with the associated MC track, qualifying it as a *good track*. Tracks with low quality, below 65%, or clones are categorized as *fake tracks*.

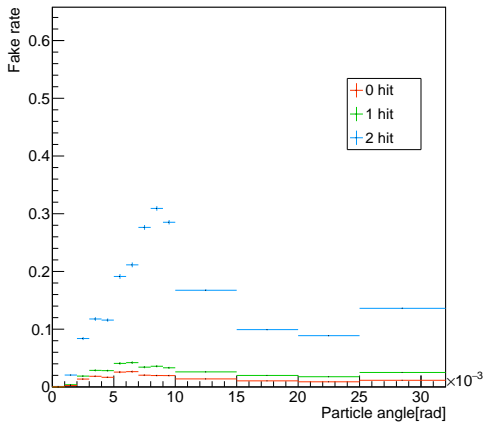


Figure 3.2: Rate of fake tracks as a function of particles scattering angle from MC simulated events generated from MESMER LO. Results are shown for different settings of the maximum number of shared hits.

The rate of fake tracks is defined as:

$$rate_{fake} = \frac{reconstructed_{fake}}{all\ reconstructed} \quad (3.9)$$

The resulting fake rates are shown in Fig. 3.2. This demonstrates again that the proportion of *fake tracks* is increased when two shared hits are allowed, particularly in the low scattering angle region.

The reconstruction efficiency has been studied from MESMER LO events, as a function of the leptons scattering angles and of the opening angles between the outgoing particles. The reconstruction efficiency is defined as:

$$\epsilon = \frac{reconstructed}{reconstructible}, \quad (3.10)$$

where, *reconstructible* are events with all the three tracks involved in the elastic process μ_{in}, μ_{out} and e_{out} lying within the geometrical acceptance at the MC level. This is achieved requiring that each track must have released at least 5 hits (established by looking at MC truth) in the tracker, which is the minimum number of hits for the Fair-MUonE reconstruction algorithm to reconstruct a track. In addition, incoming muons are required to have good track quality when reconstructed, set by requiring a normalized $\chi^2 < 2$. The definition of *reconstructed* events depends on the efficiency being studied:

1. **The reconstruction efficiency of a single particle**, μ_{out} or e_{out} . In this case, there must be at least one reconstructed track correctly associated to the requested outgoing particle, passing the given quality criterion defined by MC truth.
2. **The reconstruction efficiency of the elastic event**, i.e. both μ_{out} and e_{out} . In this case, there must be two reconstructed tracks correctly associated to the electron and to muon, respectively. In addition, it is requested that the two tracks meet in a common vertex.

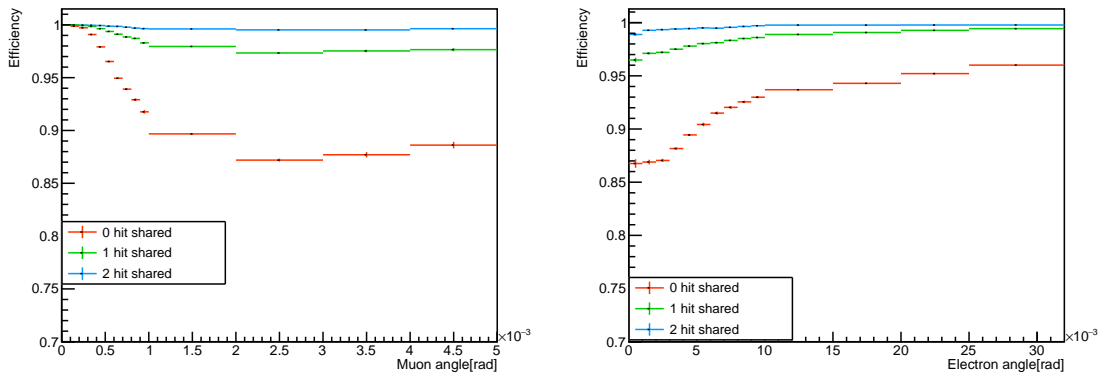


Figure 3.3: Single particle reconstruction efficiency for muon (left) and electron (right) as a function of the lepton scattering angle. The behavior with the three different configurations for the maximum allowed number of shared hits is shown (0,1,2).

The reconstruction efficiency of single particles, for the three configurations of shared hits between tracks, is shown in Fig. 3.3. The plots reveal that not allowing for hit sharing results in a significant decrease in efficiency, particularly evident for low θ_e angles, corresponding to larger θ_μ values, where the efficiency can drop to approximately 87%. In this particular region, the two particles have a relatively small opening angle, occasionally resulting in the formation of just one stub instead of two in one of the detection layers. Consequently, only one of the two tracks can be successfully reconstructed in such instances. The situation improves notably when allowing for one shared hit, leading to a

substantial increase in the efficiency. Even at large θ_e values, where the efficiency without hit sharing exceeds 90% throughout the region, there are still advantages in sharing hits. The efficiency of the vertex reconstruction algorithm plays a crucial role in defining the

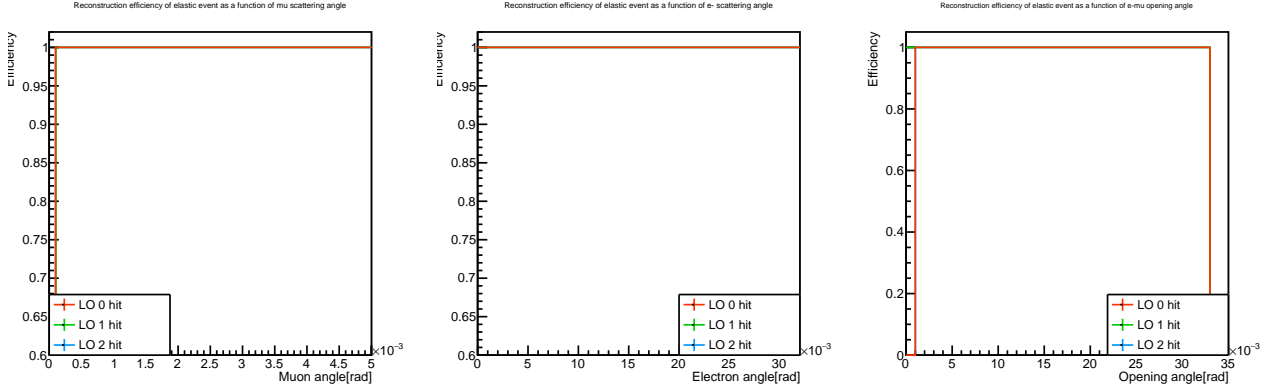


Figure 3.4: Vertex reconstruction efficiency as a function of the lepton scattering angles and the opening angle between the two leptons. The behavior with the three different configurations of shared hits is shown.

efficiency of the elastic event. This is defined as the number of events with at least two reconstructed tracks with a reconstructed vertex associated to these over the number of all events with at least two reconstructed tracks. This efficiency remains full and perfectly flat across all kinematical regions, as shown in Fig. 3.4, regardless of the number of shared hits. This uniformity arises because once the two tracks are reconstructed, irrespective of the hit-sharing configuration, the algorithm is able to reconstruct a vertex using these two tracks.

Let's now consider all the events with a reconstructed vertex. The efficiencies for event reconstruction, represented as functions of the scattering angles for different numbers of shared hits, are generally expected to exhibit similar trends as those observed for single particle efficiency, as can be seen in Fig. 3.5. However, an additional factor comes into play, when simultaneous reconstruction of both the electron and the muon is required. The inefficiency of electron reconstruction at large scattering angles, attributed to MS, is reflected in the corresponding low θ_μ region. This leads to an inefficiency of approximately 5% for muon reconstruction in that region compared to the single particle efficiency. Moreover, the efficiency as a function of the opening angle effectively demonstrates that when particles are close to each other, they benefit more from hit sharing. This leads to an approximate 30% efficiency gain for small opening angles.

The performance of the vertex finding algorithm has been tested by studying the probability of combining a wrong pair of tracks and is shown in Fig. 3.6 as a function of their opening angle. Wrong vertexing is more frequent when 2 hits are shared, however

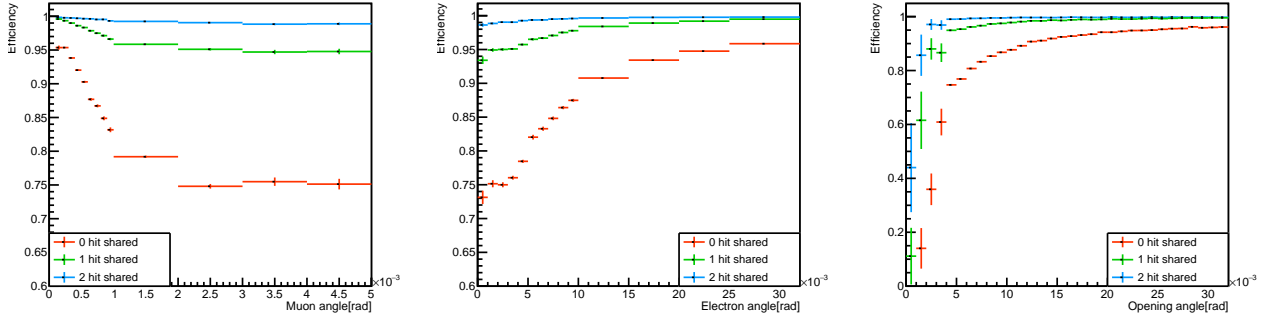


Figure 3.5: Elastic event reconstruction efficiency as a function of the lepton scattering angles and the opening angle between the two leptons. The behavior with the three different configurations for the maximum allowed number of shared hits is shown (0,1,2).

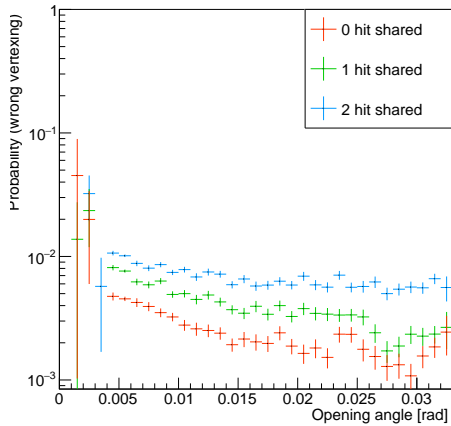


Figure 3.6: Probability of wrong vertexing (vertex not combining the correctly associated tracks) as a function of the opening angle between the two tracks.

the probability of taking a wrong combination is below 1% within the full kinematical region.

3.2.2 Angular resolution

The angular resolution has been studied from the residual distributions of the reconstructed angles compared to the true quantities known from the MC simulation. Let's define it as:

$$\Delta\theta = \theta_{reco} - \theta_{true}. \quad (3.11)$$

For the two outgoing leptons, the scattering direction is evaluated with respect to the incoming muon direction. Let's focus on the reconstructed tracks before the vertex kinematic fit.

In Fig. 3.7 and Fig. 3.8 the angular residuals respectively of the electron and the muon

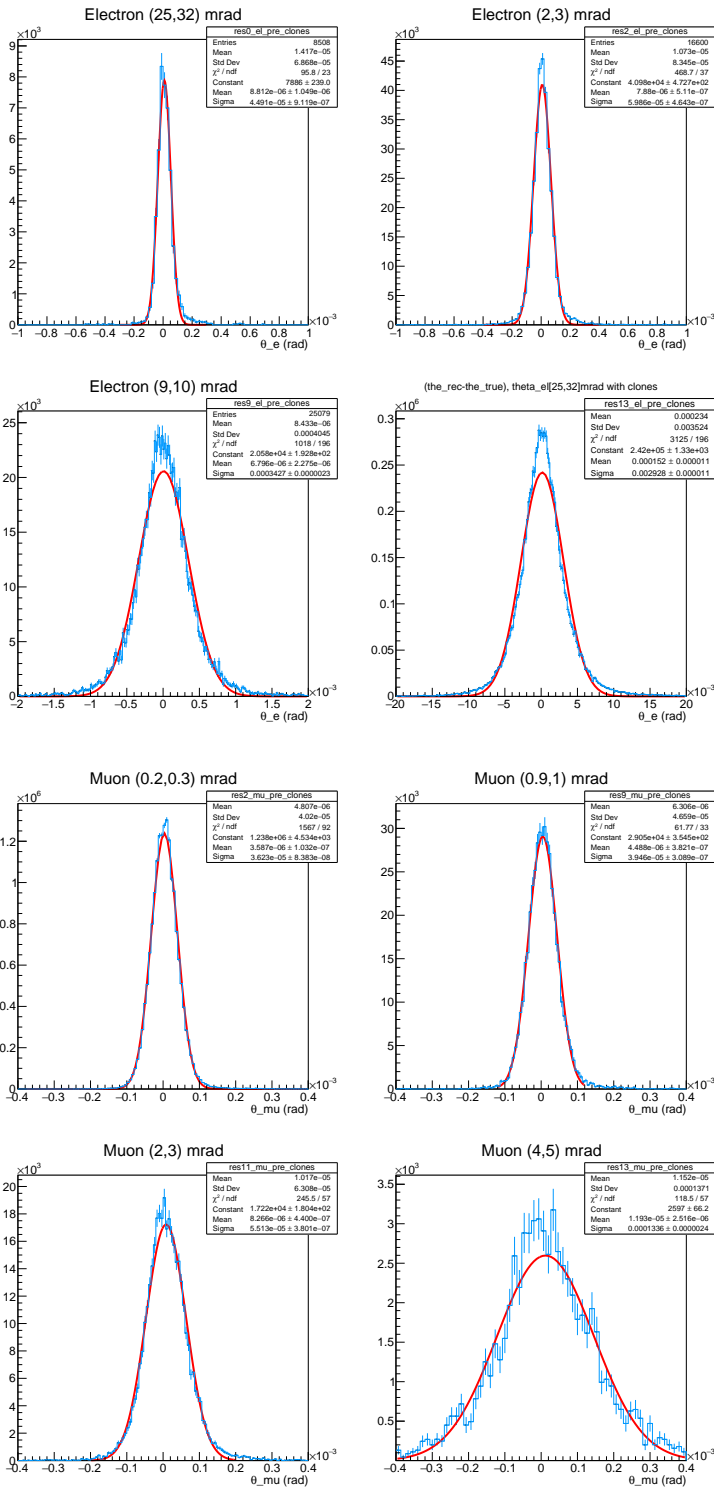


Figure 3.7: Difference between reconstructed and MC true scattering angle for the electron in different kinematic regions: 0-1 mrad (top-left); 2-3 mrad (top-right); 9-10 mrad (bottom-left); 25-32 mrad (bottom-right). A Gaussian fit is superimposed in red.

Figure 3.8: Difference between reconstructed and MC true scattering angle for the muon in different kinematic regions: 0.2-0.3 mrad (top-left); 0.9-1 mrad (top-right); 2-3 mrad (bottom-left); 4-5 mrad (bottom-right). A Gaussian fit is superimposed in red.

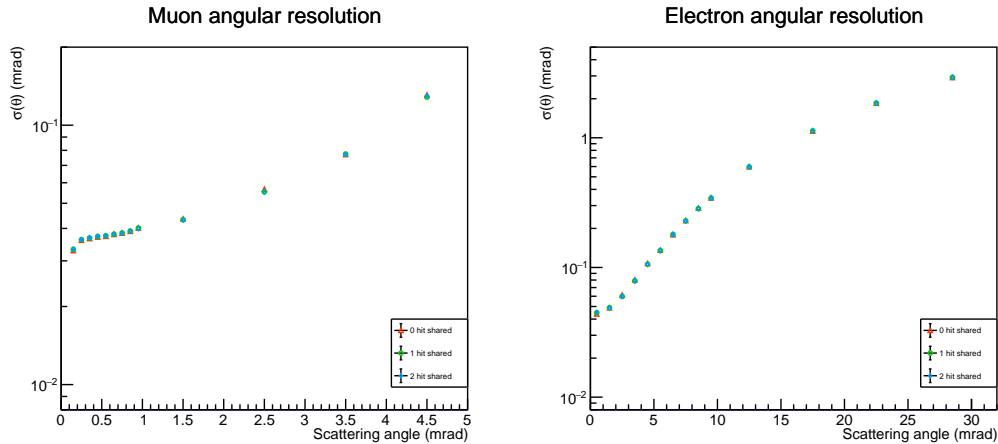


Figure 3.9: Gaussian width from the fit of the angular residual distributions of the muon (left) and the electron (right) as a function of the scattering angle. Different settings for the maximum number of shared hits (0,1,2) are compared.

Electron angle [mrad]	0 – 1	2 – 3	9 – 10	25 – 32
Resolution [μ rad]	45	60	343	2928
Muon angle mrad]	0.2 – 0.3	0.9 – 1	2 – 3	4 – 5
Resolution [μ rad]	36	39	55	134

Table 3.2: Representative values of the angular resolution obtained from the Gaussian fits of Fig. 3.7 and Fig. 3.8, for the electron and the muon respectively.

are shown for a few reference kinematic regions. Results from fits are summarized in Tab.3.2.

Fig. 3.9 reports the Gaussian width of the fits on the muon angular residual distributions as a function of the scattering angle for 0,1,2 shared hits. The first observation is that the resolution is the same independently on the allowed number of shared hits. Thus there is no degradation of the resolution allowing two shared hits, which is the configuration that maximize the reconstruction efficiency. It is also visible that the resolution of the muon is better than that of the electron over almost all the kinematic region. The reason is that the electron is more affected by MS with respect to the muon when $\theta_e \geq 5$ mrad. Currently, the treatment of MS in the track fit needs to be refined and there is still room for improvement on that side. In the most important signal region ($\theta_\mu > 1.5$ mrad and $\theta_e < 5$ mrad), the resolution for both particle ranges from 40 to 100 μ rad.

The electron and muon trajectories are fitted at two key stages: first during the recon-

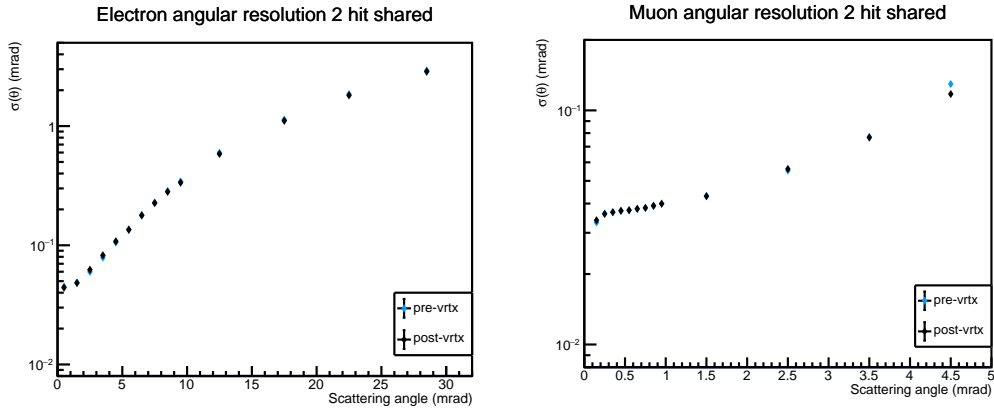


Figure 3.10: Angular resolution on the muon (left) and electron (right) scattering angle, for the reconstruction setup allowing 2 shared hits between tracks. Results are shown for both pre-vertexing and post-vertexing fits.

struction of 3D tracks, and second when three tracks are selected to create a common vertex. We can refer to these stages as pre-vertexing and post-vertexing fitting. The purpose of the post-vertexing fit is to improve the angular resolution by constraining the three selected tracks to originate from a common vertex, in the kinematical fit. Currently, the post-vertexing angular resolution is comparable to the pre-vertexing one, as shown in Fig. 3.10. However, as already mentioned, there is still room for improvements, in particular regarding MS corrections.

3.2.3 Tilted modules

The detector geometry with tilted planes was introduced in the first and last $x - y$ pairs of modules and it was verified through detector simulations that it improves the single hit resolution of 2S modules [45], as reported in Section 2.5.1. However, a relevant issue arose regarding tilted modules from other MC studies. Although it has been partially resolved since then, this issue still requires careful consideration in discussions about preserving tilted modules.

The problem deals with the presence of tails in the angle and position residuals of reconstructed tracks. An example of the outgoing muon angular residuals, defined in Eq.3.11, is shown in Fig. 3.11-top for θ_X, θ_Y projections. The presence of a long asymmetric tail is evident. The asymmetry on the negative side of the distribution indicates that the reconstructed angle sometimes underestimates the true angle. For those events in the tail ($\Delta\theta < -0.2$ mrad), the true and reconstructed distance between the muon and electron stubs is shown in Fig. 3.11-bottom and it is defined as:

$$d_{stubs} = stub_\mu - stub_e, \quad (3.12)$$

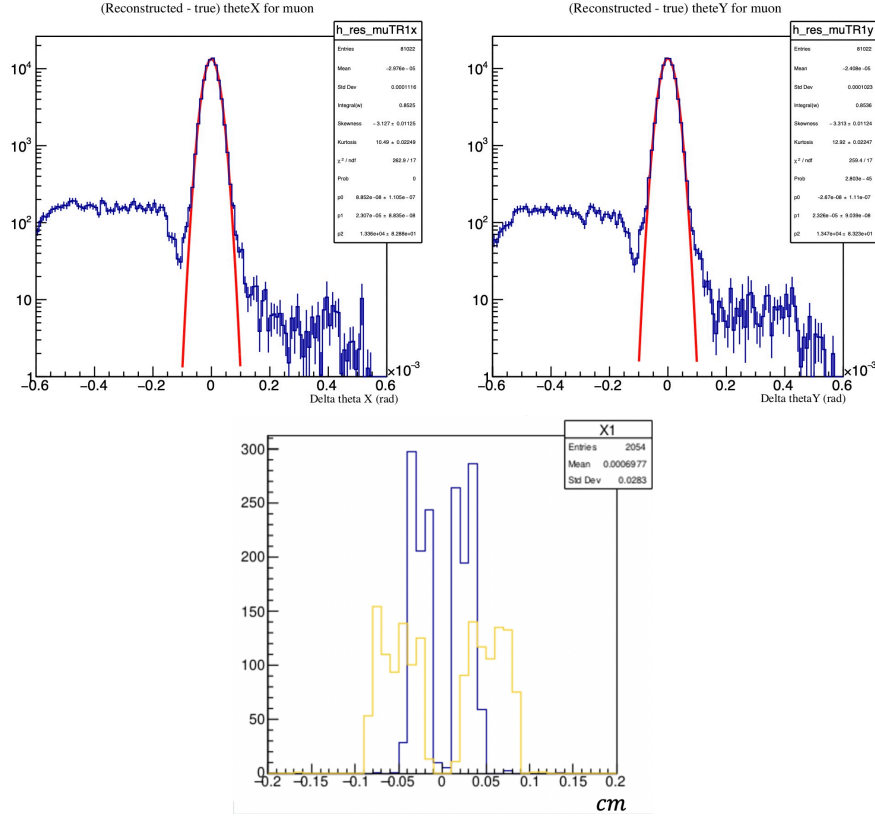


Figure 3.11: (Top) Angular residual of θ_X , θ_Y projections for outgoing muon, with superimposed a Gaussian fit. (Bottom) distance between electron and muon stubs in the first module of the second station for events in the left tail of the angular residuals ($\Delta\theta < -0.2\text{mrad}$), determined from the reconstructed hits (blue) or the true simulated hits (yellow).

where $stub_e$, $stub_\mu$ are the relative stub positions. It can be observed that events generated with a distance of less than $\sim 0.1\text{ cm}$ (~ 10 strips), may be poorly reconstructed, with the reconstruction underestimating this distance.

To gain a clearer understanding of the specific topologies where this behavior occurs, Fig. 3.12 illustrates the angular distributions of the projections, where the generated angle is compared with the reconstructed one. While for events in the core of the distributions of Fig. 3.11 ($|\Delta\theta| < 0.2\text{mrad}$) the reconstructed angles are consistent with the generated ones, for events in the left tails of Fig. 3.11 ($\Delta\theta < -0.2\text{mrad}$) there is an evident problem during reconstruction. In particular, when the particle scatters with a small and negative angle in one of the two projections, the reconstruction gets a wrong result.

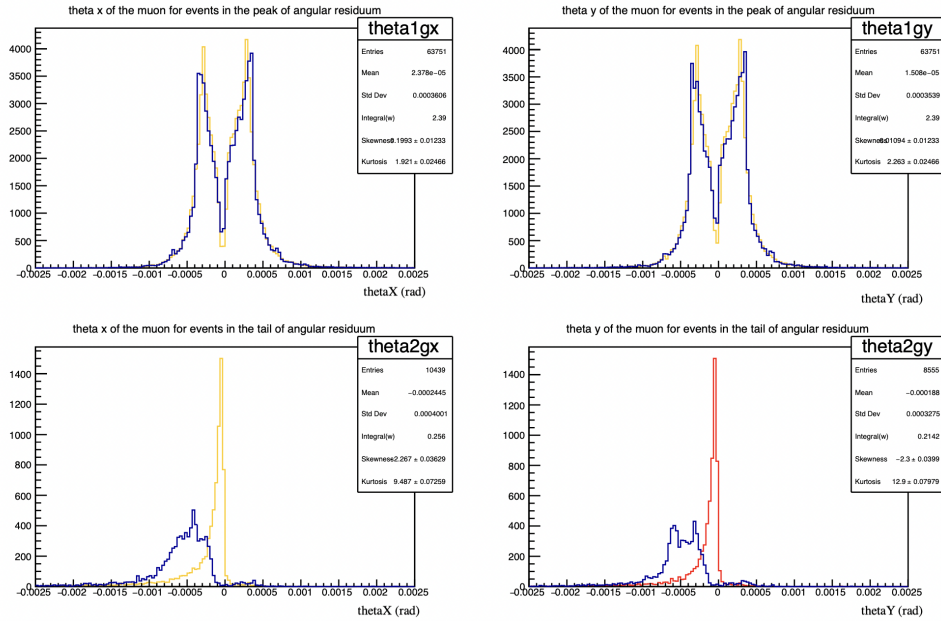


Figure 3.12: Distribution of θ_X (left) and θ_Y (right) projections for events in the core distributions of Fig. 3.11 ($|\Delta\theta| < 0.2\text{mrad}$) (top) and in the tails of Fig. 3.11 ($\Delta\theta < -0.2\text{mrad}$) (bottom). In yellow and red the angle distributions at the generator level are plotted, respectively for θ_X and θ_Y , while in blue the reconstructed angles.

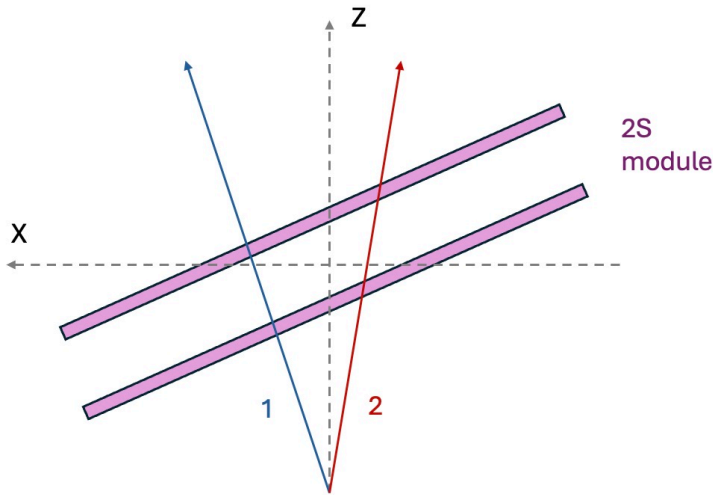


Figure 3.13: Sketch of the event topology for which the angle of particle 2 is not well reconstructed. X axis is the measurement direction of the module, while Z axis is the beam direction. 1 and 2 are the two scattered particles, while the pink lines represent the 2S module sensors.

Events from previous plots point to a particular topology: when the two scattering particles are separated by less than 10 strips and one of the two have a small and negative angle, like particle 2 in Fig. 3.13 -the one with larger bend-, the event is not reconstructed correctly.

In simulation it is possible to try different geometry configurations. In order to under-

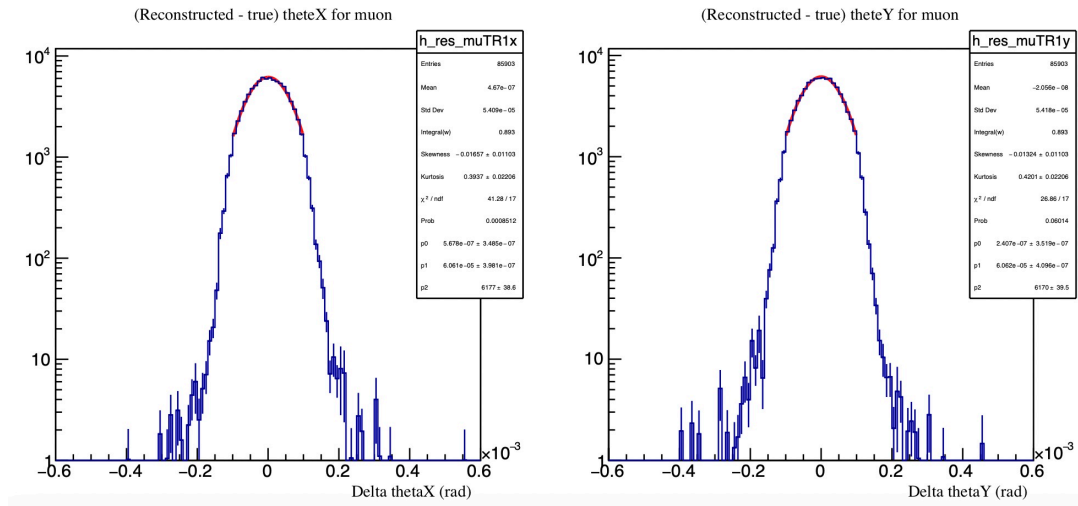


Figure 3.14: Angular residual of θ_X , θ_Y projections for outgoing muons for a geometry without tilt, with superimposed a Gaussian fit.

stand if this problem was related to the tilted geometry, a configuration with modules orthogonal to the beam axis has been simulated, and the obtained residuals θ_X and θ_Y for the measured muon angle are shown in Fig. 3.14. The tails have disappeared, indicating that this issue is connected to the presence of tilt. The problem relates to the calculation of position in the conversion from strip units to centimeters:

$$x[\text{cm}] = \left(x_{seed} + \frac{bend}{2} + \frac{1}{2} \right) \cdot \frac{9.144}{1016} - \frac{9.144}{2} \quad (3.13)$$

where x_{seed} is the seed cluster position in strip units, that comes directly from the CIC. In particular it was given by the wrong calculation of the bend. As described in Section 2.5.1, stub creation is achieved through the search of a corresponding cluster in the second sensor (correlation layer). A correlation window for the search is defined by its center and its width. The center is generally given by the seed strip position, however sometimes it may need an offset to account for geometrical effects. This is shown in the sketches of Fig. 3.15.

While for non-tilted modules the cluster of particle 2 (with highest bend) is correctly included in the correlation window (red), for tilted modules, if no offset is set for the window's center, the cluster won't be able to associate the correct correlation strip to the particle. The seed strip of particle 2 is then associated to the correlation strip of particle 1. And the bend, defined in Eq.2.27, is wrongly calculated, together with position in Eq.3.13. Tilted modules imply a systematic shift in the correlation layer. In the first

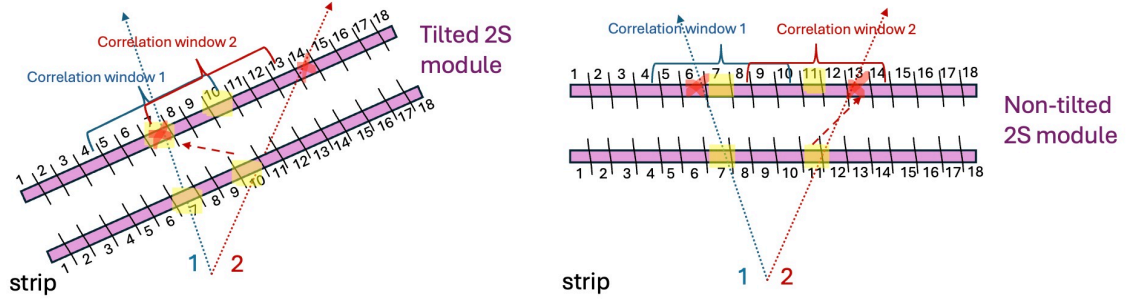


Figure 3.15: Sketch of scattering event in a tilted (left) and non-tilted (right) module, with the creation of seed and correlation cluster (respectively first and second layer). The yellow spot represents the strip fired in the seed layer and, as a consequence, the center of the correlation window (blue and red brackets) without offset, while the red cross is the fired strip in the correlation layer. The dashed red arrow represents the associated strips forming the stub of particle 2.

simulation we were studying, the offset was set to zero and this brought to the bad reconstruction of about 20% of the total reconstructed events in the angular region of $\theta_e < 5\text{mrad}$. The maximum offset that can be set in the current DAQ is limited and it is ± 3 strips. However, with a tilt of 233mrad , the needed offset to correctly reconstruct a straight particle is around ± 4.75 strips, as depicted in Fig. 3.16-left. So accounting for

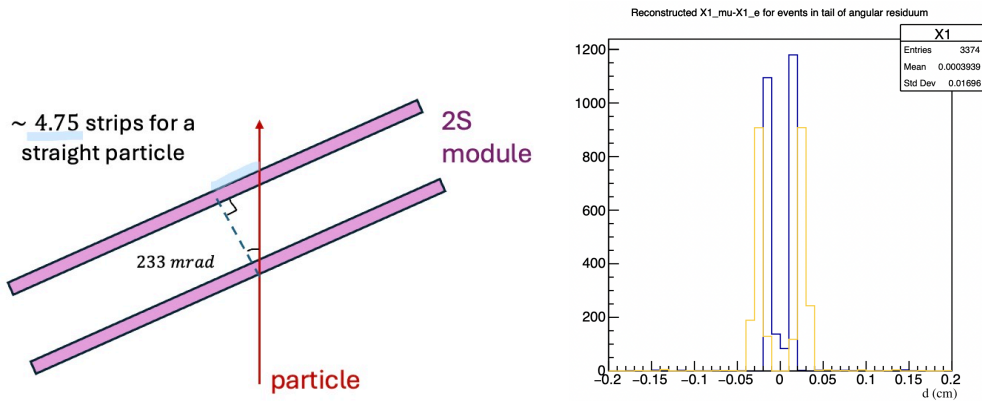


Figure 3.16: Left: Needed offset for the correlation window in tilted modules with $\theta_{tilt} = 233\text{mrad}$, given a straight particle. Right: distance between electron and muon for events in the tail of the angular residuals. Yellow is the reconstructed distance while in blue is the true MC one.

the the maximum possible offset of ± 3 strips, the remaining bad reconstructed events

pass from $\sim 20\%$ to $\sim 6\%$. In Fig. 3.16-right the true and reconstructed distance in cm between muon and electron stubs is plotted, for events in the tail of the angular residuals, after the offset is correctly set at ± 3 . Events with $e - \mu$ stubs closer than 0.04 cm, about 4 strips, suffer still from a systematic shift.

This percentage is low, however given the high precision that we want to achieve it may become important. Therefore, this drawback needs to be taken into account when assessing the benefits of tilted modules.

Chapter 4

Test Run 2023

The apparatus was installed in August 2023 in the M2 beam area at CERN. The beam period allocated as main user lasted about 3 weeks. The setup was composed by two tracking stations, equipped with six modules each, and the ECAL downstream. This configuration is essential for measuring the scattering angles of elastic interactions that occur in a thin target placed in front of the second station, by combining information from the incoming and outgoing tracks. A photograph of the experimental setup is shown in Fig. 4.1.

The technical challenges were to scale the DAQ from one to two stations, synchronize



Figure 4.1: Picture of the isolating structure containing the tracking stations and the ECAL during the August-September 2023 test run.

it with the ECAL DAQ, and test both hardware and software alignment, described in Section 3.1.3. The final goal was to collect enough statistics to provide an initial measurement of the leptonic running of alpha $\Delta\alpha_{lep}$. Part of this thesis work represents steps in the ongoing effort to achieve this measurement.

During the test run, MUonE was able to collect two weeks of data with muons of 160 GeV with maximum intensity of ~ 35 MHz. Low intensity runs were also taken, mainly for detectors calibration. Collision events were obtained with both 2 cm and 3 cm graphite targets. Data without a target were also recorded for alignment purposes.

Data throughput is determined by the intensity of the M2 muon beam. With tracker modules read out at the 40 MHz clock rate, the detector occupancy is relatively low; and pileup may be of only a few overlapping muons per clock cycle. An important point is that in the M2 beam, muons arrive asynchronously compared to the clock rate. This generates signals with random phases relative to the clock. We haven't applied any cut on the arrival time of the muon with respect to the clock signal in the 2023 data analysis, but we plan to measure the muon arrival time and take it into account in future data analysis.

The DAQ does not require a custom hardware trigger to restrict throughput. Instead, on-line filtering can be performed in firmware, reducing the computational resources needed for offline processing. As it will be presented in the next section, an online filtering was not available for this test, therefore an offline algorithm has been developed for the reduction.

The M2 beam line is set in the CERN SPS North Area. There was the possibility to choose between two possible beam profiles, with different size and divergence of the beam. For the low divergence beam option, a beam size of $\sigma_x = 13$ mm and $\sigma_y = 22$ mm with a divergence of $\sigma_{x',y'} = 0.2$ mrad was provided. While for the option of a more focused beam, the beam size was of $\sigma_x = 10$ mm and $\sigma_y = 12$ mm with a divergence of $\sigma_{x'} = 0.5$ mrad and $\sigma_{y'} = 1.3$ mrad. The second one has been chosen for the test. Examples of real-time histograms for beam spot and beam divergence of the high intensity muon beam are shown in Fig. 4.2.

The nominal beam energy of 160 GeV has an energy spread of $\sigma(p)/p \sim 3.75\%$. The

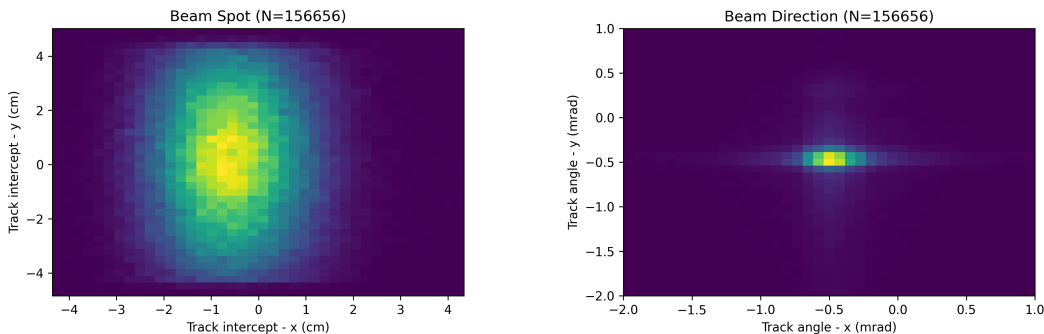


Figure 4.2: Two dimensional histograms showing the beam direction and spot recorded from real time track reconstruction in the 2023 test beam [32].

variation of incoming muons from the nominal beam energy value has a significant effect

on measured $\mu - e$ scattering angles, as it enlarges the width of the elastic band. For that reason, a precise knowledge of beam momentum is important. At the moment, the beam line is instrumented by the COMPASS Beam Momentum Station (BMS) which measures the momenta of transiting particles. It provides momentum resolution of about 1% with a DAQ rate of few kHz. Therefore, it may give us just a statistical information on entering muons in a run. Different studies are ongoing for an improvement of BMS during a possible period of data taking in 2025 with the goal of having a precise event-by-event measurement of the incoming muon momentum.

The geometry of the full setup including the two tracking stations and the ECAL was initially measured by hardware alignment techniques:

1. Laser survey on the beamline, taking as reference points several markers (spheres) installed in different places of the stations, with a precision of the order $\sim 100 \mu\text{m}$;
2. Precise metrology measurement, carried out in laboratory at CERN, on the entire station, with a precision of the order $\sim 10 \mu\text{m}$;
3. Metrology on the single modules uninstalled from the station, with a precision of the order $\sim 10 \mu\text{m}$.

Those measurements have then be used to set the modules position along the beam axis as input parameters for the track-based alignment. Recently a refined version of the software alignment has been developed, using the full set of positions and orientations of all the detector modules as initial conditions.

4.1 Data recorded and offline event selection

In a high intensity beam with many tracking planes, raw data rates generated by the detector exceed what can be stored to disk. During the 2023 test run, the DAQ did not include any online selection. Potentially all the events leaving signals in the tracking stations were recorded. The total size of events written to disk before any selection is about 350 TB of raw data. The largest fraction of these events are passing beam muons which do not make visible interactions in the detector.

It is foreseen for the next run in 2025 to implement an online selection on the DAQ electronics. The 2023 dataset has been used to prepare a suitable filtering algorithm (also called ‘skimming’), developed offline working on the recorded data. This is based on simple occupancy cuts on the tracker modules to classify the event.

As already mentioned, given pileup, there may be more than one muon in the first station. Fig. 4.3 shows the result of the selection by the filter applied to a run of the 2023 data. The black histogram represents the distribution of the total number of stubs recorded across the two stations, whilst the colored histograms represent the same events classified as a single interacting muon with no pile-up (red histogram), an interacting muon with

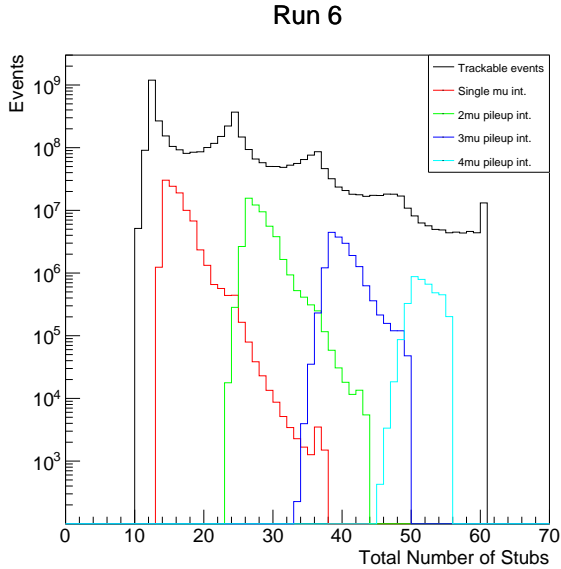


Figure 4.3: Event classification in terms of incoming muon multiplicity obtained by the filtering algorithm for a high-intensity 2023 run.

a single overlapping muon (green), an interacting muon with two overlapping muons (blue), and lastly, an interacting muon with three overlapping muons (cyan). From the yields of events classified as 1,2,3,4 passing muons and their ratios the beam intensity has been probed, assuming that muon multiplicity follows Poisson statistics. A Poisson mean $\mu = 0.85$ was estimated and it corresponds to a muon intensity of about 34 MHz. The efficiency of the filtering algorithm has been tested with MC simulations to make sure that it did not exclude interesting elastic events. Fig 4.4 shows the results obtained on a MESMER NNLO sample. Here the fraction of events passing the filter over all elastic events generated is shown as a function of θ_μ and θ_e . The plots suggest that there is no appreciable loss of signal events due to the filter.

4.2 First studies on TB data

The tracker alignment was carried out as described in Section 3.1.3, with a simple iterative procedure which exploits passing muons with one hit in each module. Unbiased residuals can be evaluated as the difference of the measured hit position per module and the expected position from the fitted track, which asses through all hits but the one under test. First results are shown in Fig. 4.5 where the mean values are all centered at zero within less than $1 \mu\text{m}$. The RMS values are all consistent with the expected hit resolution.

It has been mentioned in Section 2.5.1 that the improved resolution obtained by the tilted detector modules was given by the increment of the number of two-strip clusters

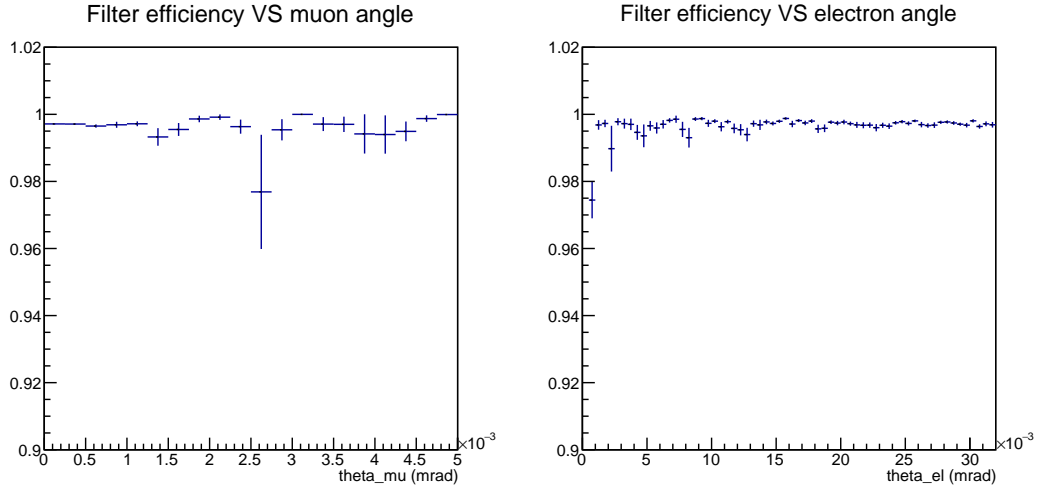


Figure 4.4: Ratio of reconstructed events passing the skimming algorithm over all elastic events reconstructed in a NNLO MESMER sample as a function of muon (left) and electron (right) scattering angle.

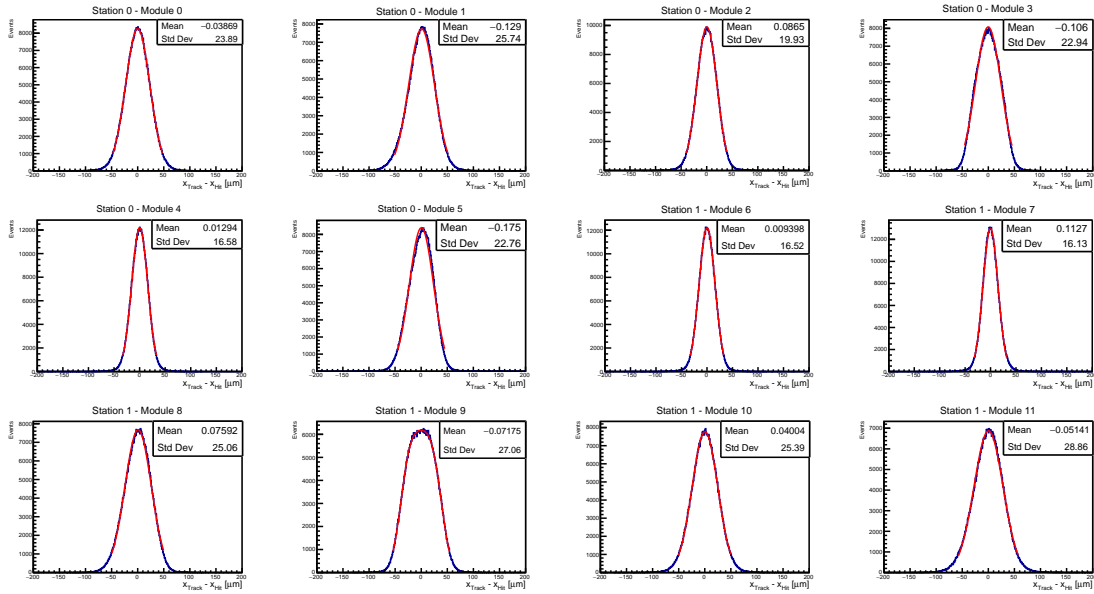


Figure 4.5: Unbiased residual distributions of the measured hit position on the 12 tracker modules fitted by a Gaussian (0-5: modules of the first station, 6-11: modules of the second station) [32].

with respect to the orthogonal configuration which gives almost always single strip clusters. Fig. 4.6 shows the fraction of clusters of even size for tilted (X-Y) and orthogonal

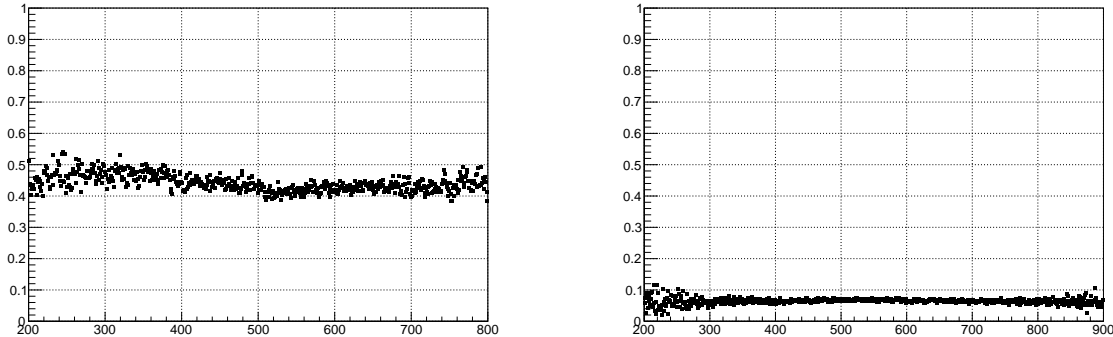


Figure 4.6: Fraction of events with even cluster size in X-Y tilted modules (left) and U-V non-tilted modules as a function of the cluster position in the module (in strip units).

(U-V) tracker modules. Parity of the cluster was studied more than its size as this is the only information available with the current CMS electronics. While for tilted modules the fraction is between 40 – 50%, for the non-tilted ones it is lower than 10%. Therefore, charge sharing is happening in tilted modules as expected, and, for them a higher resolution should be achieved. The study to verify this consequence on angular resolution in real data is still ongoing.

For each module, the efficiency has been evaluated exploiting again passing muons

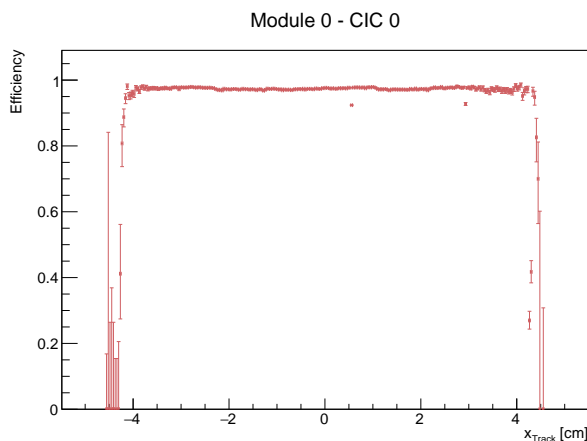


Figure 4.7: Example module efficiency as a function of the track position, obtained in one run with low intensity beam.

through the aligned stations. A track with good χ^2 is selected with hits in all modules except for the one under test. Then, the matching hit is searched there, within a window of $130\ \mu\text{m}$. An example of the efficiency for the first X module of the first station is shown in Fig. 4.7. The average module efficiency found is about $(98.0 \pm 0.5)\%$.

The efficiency for the full track reconstruction in a single station has been tested. Reconstructed muons with all the six hits in the first station are selected, the so-called

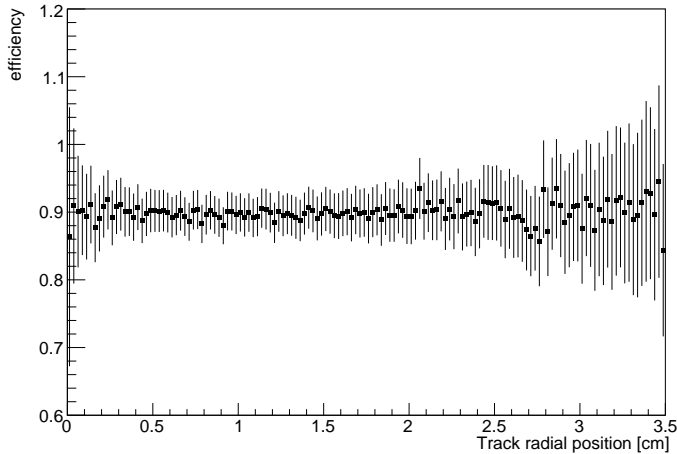


Figure 4.8: Efficiency of muon track reconstruction in the downstream station as a function of the track radial position for events with a muon reconstructed in the upstream station. The position is defined relative to the average beam position [32].

golden muons. To evaluate efficiency, the reconstructed muon is searched also in the second station. Fig. 4.8 shows it as a function of the track radial position. The latter has been defined by the extrapolation of the position at the target plane, with respect to the average position of beam muons. The tracking efficiency is found to be flat at about $\sim 90\%$. This is consistent with the combinatorial result of individual module efficiencies reported above, given that the tracking algorithm accepts also patterns with five hits, if the missing hit is on one of the two stereo layers. With this logic, the probability of track building can be estimated from a common value for the module efficiency ϵ , assuming uncorrelated effects, as:

$$\epsilon_{track} = \epsilon_{mod}^6 + 2(1 - \epsilon_{mod})\epsilon_{mod}^5 = 0.922 \pm 0.019. \quad (4.1)$$

An important first step was achieved regarding the synchronization of tracker and ECAL,

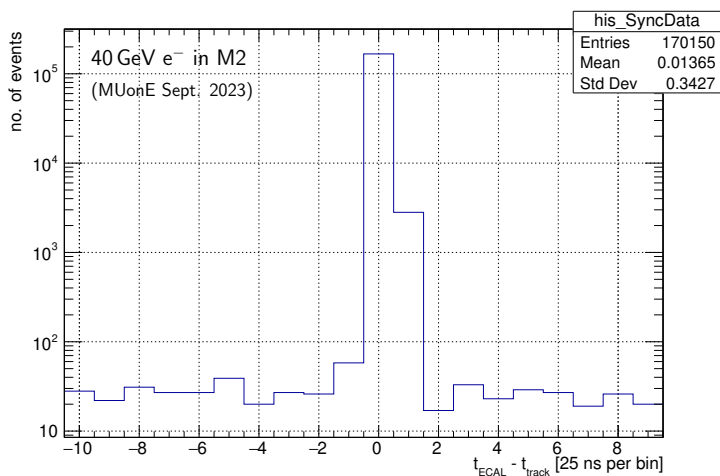


Figure 4.9: Time difference between ECAL and tracker events for an electron beam after the delay offset between the two has been applied [32].

which was one of the main purposes of the test run. Electron induced showers in ECAL have been found matching tracker tracks. A preliminary result is shown in Fig. 4.9, the time difference between matching events found in the two subdetectors in run with 40 GeV electron beam. The coincident events have been moved to the $\Delta t = 0$ bin, the raw time offset was $\sim 1.5 \mu s$.

Chapter 5

Real data and MC comparison

During the test beam data samples have been collected with 2 and 3 cm graphite targets. We have begun analyzing preselected events (using the filter discussed in Section 4.1), such as 'single-muon candidate interactions,' characterized by hit patterns consistent with a single incoming muon in the first station and two tracks in the second, potentially indicating an interaction within the target. The distribution of those vertex z position is shown in Fig. 5.1, overlaying results obtained in two runs with different target sizes. The vertex resolution is found to be about 0.8 cm for the 2 cm target, while slightly worse for the 3 cm, consistently with the expected MS. The prominent peak comes from events originating in the target, while lower peaks correspond to events from the silicon layers of the tracker sensors: the first two peaks correspond to the last two modules in the first station, while the last peak is produced by the first module of the second station.

Fig. 5.2 shows the 2D kinematic distribution of the scattering angles observed in can-

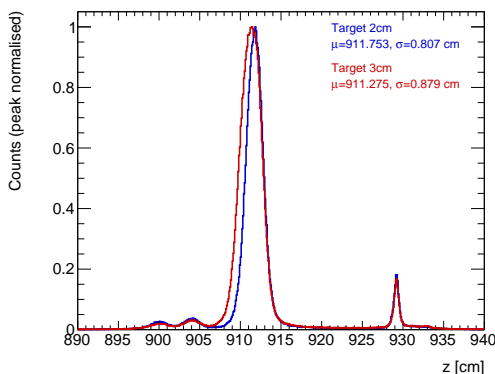


Figure 5.1: Vertex z position determined for events with two outgoing tracks.

didate events of a given run before and after a basic elastic selection. By just requiring an incoming single track and a pair of outgoing tracks loosely matching in a vertex, a high background is found at low θ_{min} . Despite this, the elastic scattering band is already

visible. The loose selection applied effectively reduces the low-angle band region. A more

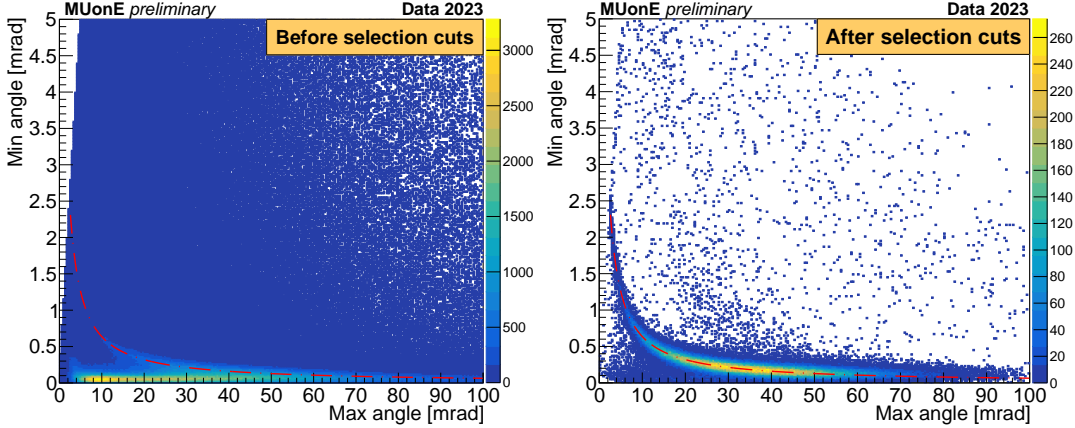


Figure 5.2: 2D $(\theta_{max}, \theta_{min})$ distribution of candidate scattering events: (Left) before and (Right) after the loose elastic selection. The elastic curve is plotted in red.

refined elastic selection has been studied and will be presented in the next paragraphs. For the following data-MC comparison, MESMER MC samples and data collected with a target of 3 cm have been used. Preliminary comparisons have also been performed using Geant4 minimum bias samples to cross-check MESMER results.

Data-MC comparison aims to assess the level of agreement between the two. In order to do so, several steps are required:

1. Real data are first preselected by the skimming algorithm, as described in Section 4.1. MC samples produced with MESMER generator skip this step, as every event simulates a muon-electron interaction is applied;
2. A fiducial cut on the incoming muons;
3. an elastic selection on outgoing particles, in order to discard background/not-interesting events, is applied.

MC samples are generated with a realistic geometry where a misalignment is implemented, based on the metrology measurement carried out at the end of the data taking, as mentioned in Chapter 4. The position and orientations of all the detector modules are given as initial conditions for the iterative alignment procedure, described in Section 3.1.3. This alignment algorithm is the same one used for real data samples.

Fiducial selection The first set of cuts applied is the *fiducial* set. The goal is to select **golden muons**, meaning good quality muon tracks in the upstream station with all 6 stubs, in a selected fiducial region. The latter will remove peripheral muons which could produce scattered electrons outside the target. Several requests are applied:

- The total number of stubs in the first station has to be six, one per module;
- The golden muon candidate impinges last modules of the first station within ± 1.5 cm from the module's center;
- The reconstructed incoming muon has an angle lower than 0.4 mrad;

Elastic selection Then *elastic* cuts are implemented. These aim to select a sample of elastic events as clean as possible. Several requests are applied:

- * The total number of stubs in the second station is set to be ≤ 15 . The aim is to exclude background events with more than two outgoing tracks;
- * A vertex must be reconstructed where at least two outgoing particles are present;
9
- * $\theta_\mu > 0.2$ mrad to exclude the low-band region where background noise is predominant;
- * $\theta_e < 32$ mrad done in order to have maximal efficiency accounting for the geometrical acceptance;
- * **Vertex position:** Some events may have a vertex in the last silicon module and could potentially pass fiducial cuts, as they appear to have six stubs in the first station. Therefore, a selection of events based on the reconstructed Z of the vertex is done such that $Z_{vertex} > 906$ cm;
- * **Acoplanarity:** This variable is defined as the azimuthal difference between the two outgoing tracks relative to the direction of the incoming muon. Elastic events exhibit balanced transverse momenta, resulting in back-to-back outgoing particles, within detector resolution effects. In contrast, this is not true for radiative or background events. It is defined as

$$A_\phi = \pm \left[\pi - \cos^{-1} \left(\frac{(\vec{i} \times \vec{m}) \cdot (\vec{i} \times \vec{e})}{|\vec{i} \times \vec{m}| |\vec{i} \times \vec{e}|} \right) \right] \quad \text{where} \quad T = \vec{i} \cdot \vec{m} \times \vec{e} \quad (5.1)$$

where \pm depends on the sign of T . The cut is set to be $|A_\phi| < 0.4$;

- * $\theta_e > 5$ mrad. An analysis can also be done without particle identification (PID), using θ_{right} and θ_{left} as scattering angles (see [31]). In this analysis, particle identification (PID) assigns the electron to the track with the larger reconstructed angle and the muon to the track with the smaller angle. This cut allow to have **no ambiguity** on the identity of particles, as μ kinematics has $\theta_\mu < 5$ mrad;

- * **Elasticity**: a clear elastic relation exists between θ_μ and θ_e , as illustrated by the red curve in Fig. 2.2, which follows Eq.2.15. Therefore, given the reconstructed θ_e^{rec} , one can predict the theoretical elastic $\theta_\mu^{th}(\theta_e^{rec})$ and ask that θ_μ^{rec} is within ± 0.2 mrad (at least 3σ from the expected angular resolution) from the theoretical value.

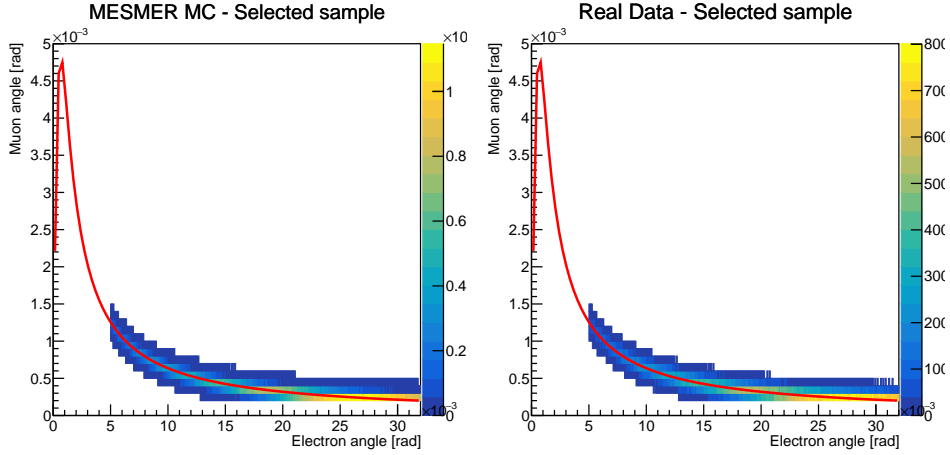


Figure 5.3: MESMER MC (left) and real data (right) samples after the fiducial and elastic cuts to select a clean sample of elastic events. In red the elastic curve described by Eq.2.15 is shown.

In Fig. 5.3 the selected elastic samples in MESMER MC and real data are shown in a 2D plot of the reconstructed scattering angles (θ_e, θ_μ) .

To have a proper comparison between real data and MC, the latter need to be normalized. Each MC sample, where events are weighted, corresponds to an integrated luminosity ¹ given by:

$$\mathcal{L}_{MC} = \frac{\sum_j w_j(fiducial)}{\sigma_{el}} \quad (5.2)$$

where $\sum_j w_j(fiducial)$ is the sum of weights of all the events passing the fiducial cut and σ_{el} is the total cross section of the generated sample, as computed by MESMER.

The integrated luminosity of the real data sample can be estimated from:

$$\mathcal{L}_{RD} = N_{\mu oT} \cdot d_{target} \cdot \rho_{target}^e, \quad (5.3)$$

where $N_{\mu oT}$ is the number of golden muons impinging on target in a given fiducial region, d_{target} and $\rho_{target}^e = \rho \cdot \frac{Z}{A} \cdot N_A$ are respectively its thickness and electron density. The

¹It has to be considered more as an effective luminosity with the aim of scaling to the real data one, statistical power is lower being weighted events.

latter depends on the the atomic and mass numbers, Z and A , and on the Avogadro number N_A . Therefore, the normalization for MC samples results in $\mathcal{L}_{RD}/\mathcal{L}_{MC}$.

In the following Section, a single run from the 2023 test has been analyzed. This run had a 3 cm graphite target and lasted about 1.5 hours. The sample has been skimmed offline by the algorithm described in Section 4.1, reducing the initial 12×10^9 events recorded in triggerless mode to about 97×10^6 events, compatible with single muon interactions. Given Eq.5.3, in order to compute the luminosity of the sample, the number of muons on target needs to be known.

Fiducial cuts are applied to the filtered sample. A passing muon in the first station is indistinguishable from one interacting in the last module before the target. In both cases, the number of stubs produced remains six, causing these events to be categorized as golden muons that could potentially interact with the target. However, the probability of an interaction with the target occurring after an interaction in the silicon is negligible, thus these muons have to be excluded. If one does not take this into account, $N_{\mu o T}$ is overestimated, so does \mathcal{L}_{RD} . A incoming muon passing the golden selection can behave in three ways:

1. Interact in the last silicon module of the first station;
2. Interact in the target;
3. Pass by without relevant interactions.

Therefore, defining N_{golden} as the number of all golden muons, the luminosity takes the form:

$$\begin{aligned}\mathcal{L}_{RD} &= N_{golden} \cdot (d_{silicon} \cdot \rho_e^{silicon} + d_{target} \cdot \rho_{target}^e) = \\ &= N_{golden} \cdot (c_{silicon} + c_{target}).\end{aligned}\tag{5.4}$$

where the contribution of a silicon module of 0.064 cm is $c_{silicon}$ and the one from 3 cm target of graphite is c_{target} . The corrected number of muons on target can be estimated from the number of selected golden muons N_{golden} as:

$$N_{\mu o T} = \frac{c_{target}}{c_{total}} N_{golden} = 97.3\% N_{golden}\tag{5.5}$$

with negligible uncertainty of 0.1%.

In that sample there were $N_{golden} = 8.98816 \times 10^8$, therefore the integrated luminosity computed from Eq.5.3 results to be

$$\mathcal{L}_{RD} = (1443.0 \pm 8.0) \mu\text{b}^{-1}.\tag{5.6}$$

An error of 10 μm has been assumed for the target thickness and of 0.01 g/cm³ on the graphite density.

Dealing with MC, eleven samples of 1.5×10^6 weighted events each have been generated. The estimated MC cross section is

$$\sigma_{el}^{tot} = (1341.65 \pm 0.49) \mu\text{b} \quad (5.7)$$

Therefore, from Eq.5.2:

$$\mathcal{L}_{MC} = (8351.6 \pm 1.4) \mu\text{b}^{-1}. \quad (5.8)$$

5.1 Results

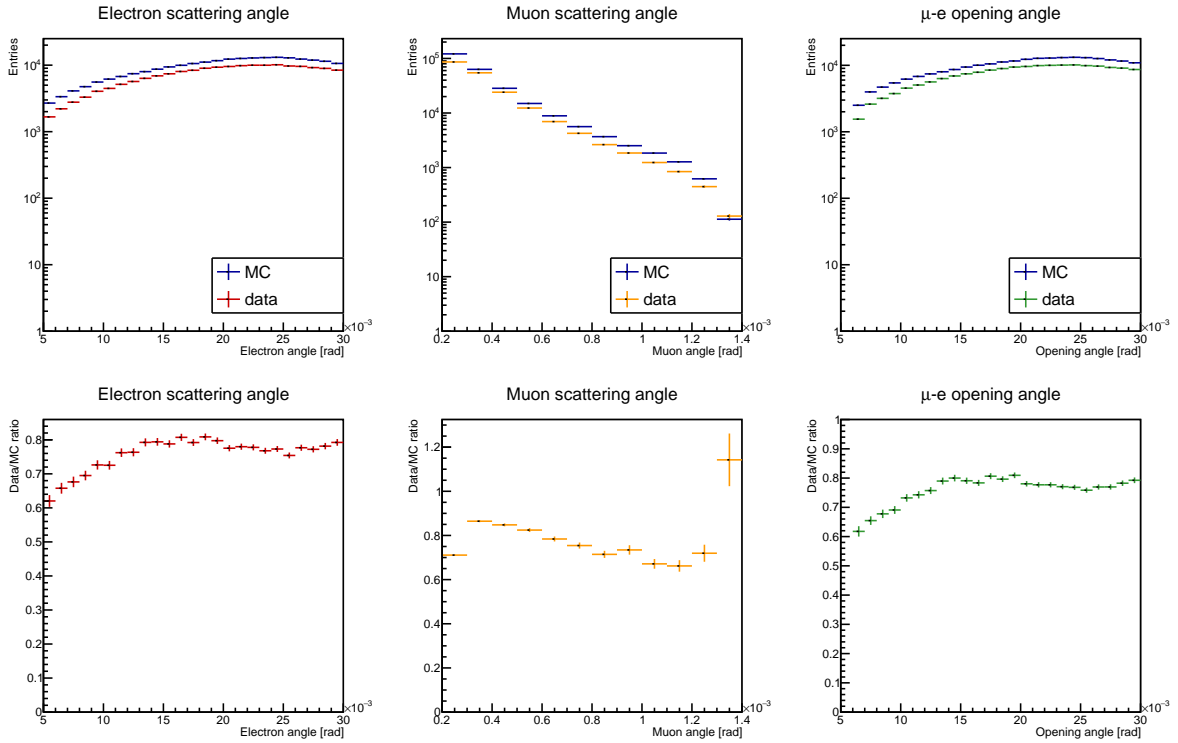


Figure 5.4: Top: differential distributions of the variables in MC (blue) and data (colored). Reconstruction is done sharing 2 hits. Bottom: ratio of data and MC events passing the elastic selection as a function of θ_e (left), θ_μ (center) and relative opening angle (right).

The first study consists in comparing the ratio of events passing the elastic selection in data and MC as a function of θ_e and θ_μ variables. The *uniformity* of the ratio throughout the kinematic region is essential. Furthermore, its mean value reflects the overall system performance in collecting and reconstructing data by integrating all contributing

efficiencies, such as detector and tracking efficiency.

As discussed in Section 3.2.1, according to MC simulation the maximum reconstruction efficiency for elastic events is achieved allowing for two hits shared between the outgoing tracks. With this parameter setting, Fig. 5.4 shows the distributions of reconstructed scattering angles of the electron and muon and their opening angle, comparing real data with the MC expectations. By examining the ratio as a function of θ_e , it becomes evident that it is not uniform, particularly for $\theta_e < 15$ mrad. The plot of the ratio against the opening angle between the muon and electron (Fig. 5.4 right) demonstrates that this lack of uniformity is pronounced at small opening angles between the two leptons. In addition to this leading feature, there are deviations from the uniformity in the high side of plotted angular ranges. These are likely resolution effects, as a consequence of the cuts applied at $\theta_e > 5$ mrad and $\theta_{mu} > 0.2$ mrad respectively. As reported in [51], if the resolution is not well described by MC, a distortion of the *data/MC* ratio as a function of the angles is expected. Therefore the distortion seen in these two regions may be strongly correlated to this.

The optimal reconstruction configuration allows for two shared hits. However, it results

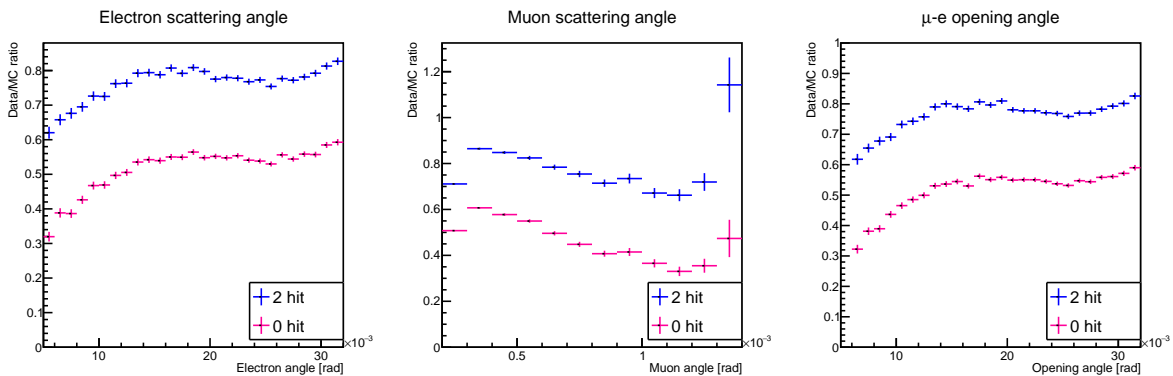


Figure 5.5: Ratio of data and MC events passing the elastic selection as a function of electron angle (left), muon angle (center) and relative opening angle (right). Two settings of the reconstruction are compared: maximum number of allowed shared hits between tracks equal to 2 (blue) or 0 (pink).

in an increased number of fake tracks, as illustrated in Fig. 3.2. This complexity adds to the challenges of event reconstruction in real-world scenarios. Therefore, passing to the simpler configuration of zero hits shared may facilitate a better understanding, allowing us to investigate whether the hit-sharing mechanism is causing any issues. Fig. 5.5 shows the data/MC ratio as a function of the angular variables, comparing the results for the maximum number of shared hits set at zero and two. The behavior is quite similar for both scenarios; however, the value of the ratio worsens more than 20% in the zero hits case. This occurs because sharing two hits is a looser condition. Therefore, if two

tracks happen to share hits because of proximity or misalignment, the zero-hit case will completely reject the event, while the two-hits one allows for its reconstruction.

To confirm that this is the case, the hit pattern of selected events was studied, focusing

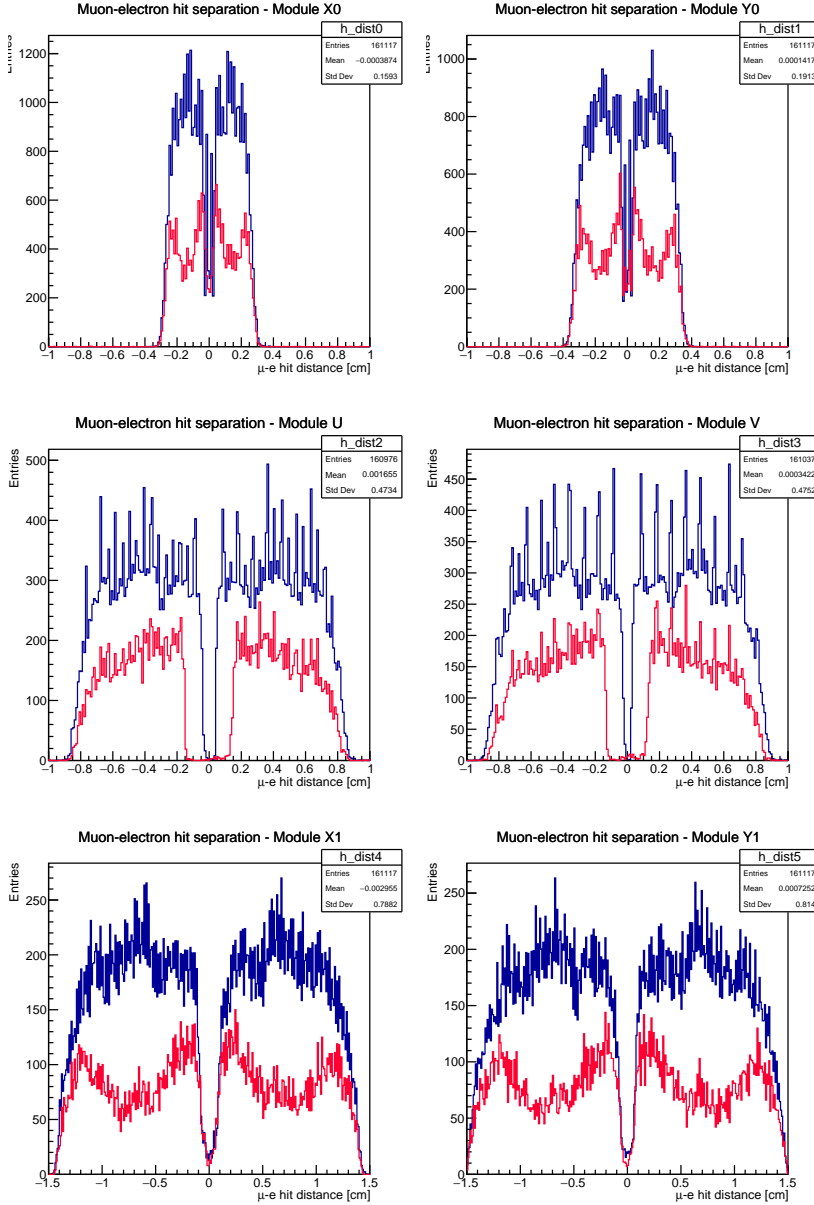


Figure 5.6: Distance between the stubs assigned to muon and electron tracks for each module. Top row corresponds to first two modules X0 and Y0, middle row to stereo modules U and V, bottom row to last modules X1 and Y1. The MC (blue) is compared to the real data (red).

on the case of $5 < \theta_e < 15$ mrad. This range is particularly relevant as the issue is more pronounced at low opening angles. In Fig. 5.6 the distance between the stubs associated to the muon and electron track for each module is shown. As expected, the distance between stubs increases as the particles travel farther. It is evident that the MC does

not accurately represent the data within certain ranges of this distance. Moreover, the evident lack of events in real data is due to the low ratio shown in Fig. 5.5, in the zero hit shared case. Focusing on the U and V modules, there is a significant gap around zero in the data. This indicates an inefficiency of the reconstruction of elastic events when the two U or V stubs are less than 2 mm apart. It has been demonstrated by simulations that the U/V region with $d < |2 \text{ mm}|$ corresponds to the X0,Y0 dips at $d \sim |2 \text{ mm}|$ and to the X1,Y1 dips at $d \sim |8 \text{ mm}|$, thus these lacks of events are correlated.

The results presented above were generated using realistic MC. However, it is worthwhile

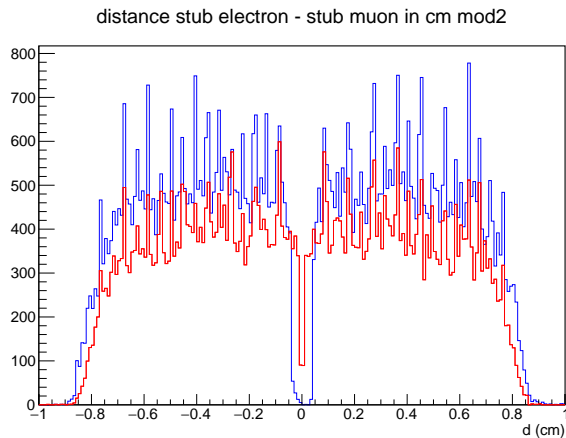


Figure 5.7: Distance between the muon and the electron hits in the U module. In blue realistic MC while in red ideal MC.

to compare these plots with those obtained under ideal conditions, where the residual misalignment is not simulated. Fig. 5.7 shows the distribution for U module obtained with MC using the realistic and the ideal geometries. The dip, clearly visible in real data (Fig. 5.6), begins to emerge in the realistic MC configuration, whereas it is absent in the ideal one -except for the minimal distance that must exist between two different stubs, naturally causing the red dip around zero. Given that the only difference between the two setups is the introduction of misalignments, this suggests that the cause of the hole may lie in an incomplete alignment of the detector.

As described in Section 3.1.2, starting from the 2D tracks candidates, the chosen 3D combination is formed based on the closest stereo hit. Let's assume that two 3D track candidates share one hit. If the hit-sharing parameter is set to zero, the default mechanism is to reject the worst track and keep the best one (quality is based on track's χ^2). However, there is a setting that can be configured in the algorithm which modifies this definition. Instead of rejecting the entire track, only the shared hit is removed from the hit pattern of the worst track. Then, if after this removal the candidate is still reconstructible, namely if it still has two X, two Y and at least one of the two stereo hits, the track is kept and fit without that stub. Thus, the event is saved, both tracks are reconstructed. Let's call it the *zero-loose* configuration.

The 2D event drawing in Fig. 5.8 presents an example of the two different behaviors for

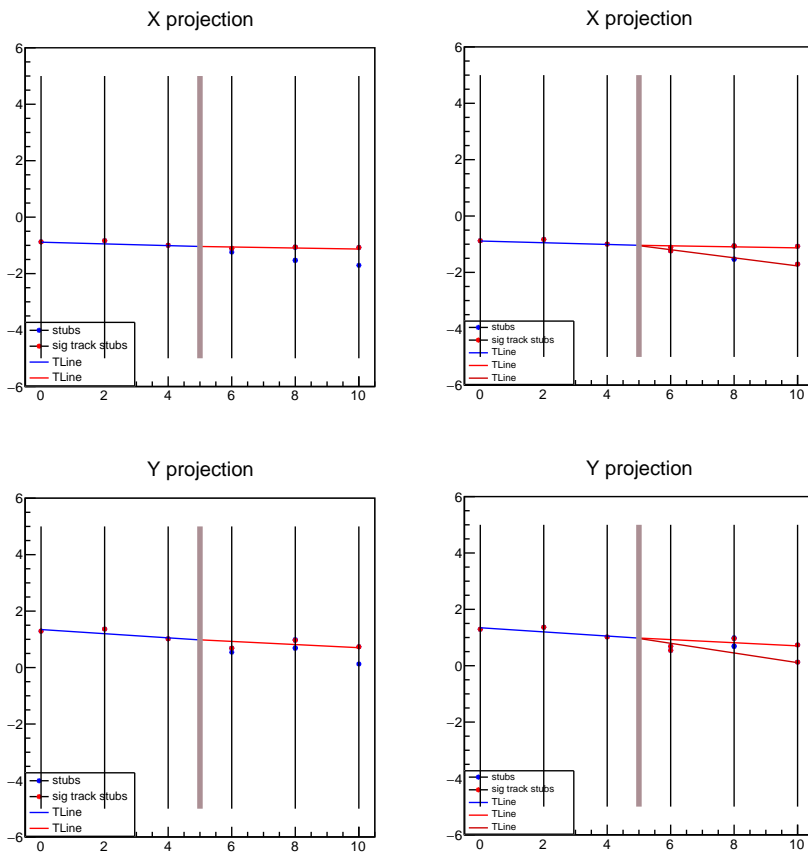


Figure 5.8: 2D event drawing showing the 2D projections XZ (top) and YZ (bottom) of the reconstructed tracks and all the stubs per module in the given event. The brown thick line represents the target, while the black ones the modules. The event is reconstructed with no shared hits allowed, with the tight "zero" setting (left) or with the *zero-loose* criterion (right).

a given event where a hit is tried to be shared. All the stubs in the X and Y views are shown. U and V hits information are combined to obtain a single (X,Y) point through a 45° rotation. While with the tight zero-hit setting just one of the two outgoing tracks is reconstructed, with the *zero-loose* setting also the second track is reconstructed, but without one of the two stereo hits. The potential shared hit is removed and the track is kept and fit without it.

In Fig. 5.9 the two reconstruction settings are compared by showing the resulting data/MC ratios for the angular distributions. It is evident that the *zero-loose* configuration enables to recover from $\sim 20\%$ to 40% of the events that the tight zero-hit setting is not able to reconstruct. In addition, the behavior of the ratios start to be flatter in a wider range of the kinematics.

5.1.1 Analysis of the problem

The algorithm, in its current form, seems to have some difficulties when dealing with real data. The reason may lie in the residual misalignment, which adds complexity to the pattern recognition. Thus, depending on the configuration used, events may or may

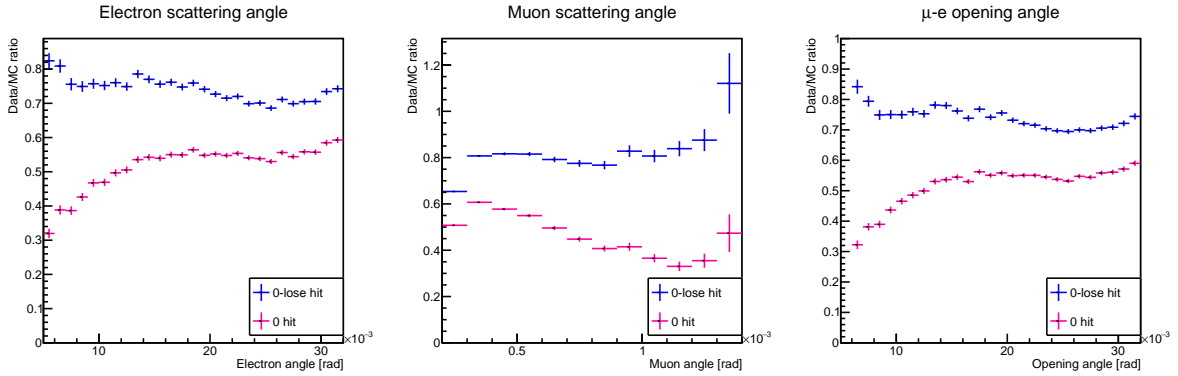


Figure 5.9: Ratio of data and MC events passing the elastic selection as a function of electron angle (left), muon angle (center) and relative opening angle (right). Here the ratio obtained reconstructing with *-zero-loose* condition (blue) are compared with the ones obtained with a 0 hit shared (pink)

not be reconstructed.

Let's examine the pathological case discussed in the previous section. An event with twelve stubs in the second station, two per module, has been selected (as the one in Fig. 5.8). With the tight zero-hit setting for the hit sharing, only one of the two tracks is reconstructed. Conversely, under the *zero-loose* condition both tracks are successfully reconstructed. Excluding one hit improves the reconstruction efficiency; however, the correct, missing hit is present but not utilized.

Considering how the algorithm logic works, for each 2D tracks combination only the closest stereo hit in the acceptance UV window (0.3 cm) is considered for the final 3D track fit. However, imperfect alignment in conjunction with multiple scattering (MS), especially for very close stereo hits ($d < 0.2$ cm), may result in the closest hit not being the correct one. The correct stub might be there, farther away, without being taken into account. If the nearest hit is also associated to another track with better χ^2 , then the considered track is rejected, in the tight zero-hit configuration. If sharing multiple hits is permitted, the track may be reconstructed, but its quality could be compromised, making it unlikely to pass the elastic selection criteria.

To make the algorithm's logic more robust against the complexities of real data, a new approach has been developed. If there is more than one stereo hit within the acceptance UV window, and the first attempt selects the hit associated with the best track, the shared hit should be discarded. Then the algorithm will look for a second hit inside the window, and attempt to use it if available.

The change has been applied in the reconstruction code, modifying the logic of 3D candidates creation. The same event displayed in Fig. 5.8 has been reconstructed with the new algorithm, setting the configuration for no hit sharing. Fig. 5.10 shows the relative

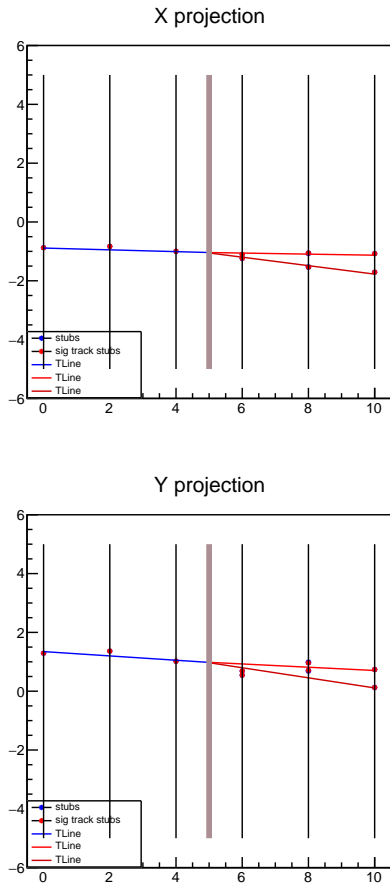


Figure 5.10: 2D event drawing showing the 2D projections XZ (top) and YZ (bottom) of the reconstructed tracks and all the stubs per module in the given event. This is how the event is reconstructed by the new version of the algorithm when 0 shared hits are allowed.

event drawing in the X and Y projections. All the hits are now correctly used and the whole event is reconstructed also with the setting of zero hit shared.

It is mandatory to ensure that this modification does not introduce any drawback in the angular resolution. To test it, the validation code discussed in Appendix A can be used to compare efficiency and angular resolution resulting from the new version of the algorithm with the default one, on simulated events. The realistic geometry has been used for this validation and results are shown in Fig. 5.11 for the efficiencies as functions of the muon and electron scattering angles, and their relative opening angle, for different settings of the hit sharing parameter. The efficiency is significantly improved by the updated algorithm for the zero-hit setting of the hit sharing parameter, up to about 10% in certain regions. Instead, the performance for the setting of one and two shared hits is basically unchanged.

It could be argued that if this issue is merely a matter of misalignment, as reproduced by the realistic MC, a better alignment procedure might solve it without requiring modifications to the code. Therefore, the efficiency has been tested for a simulation with the ideal geometry, where there is no misalignment and only multiple scattering may have

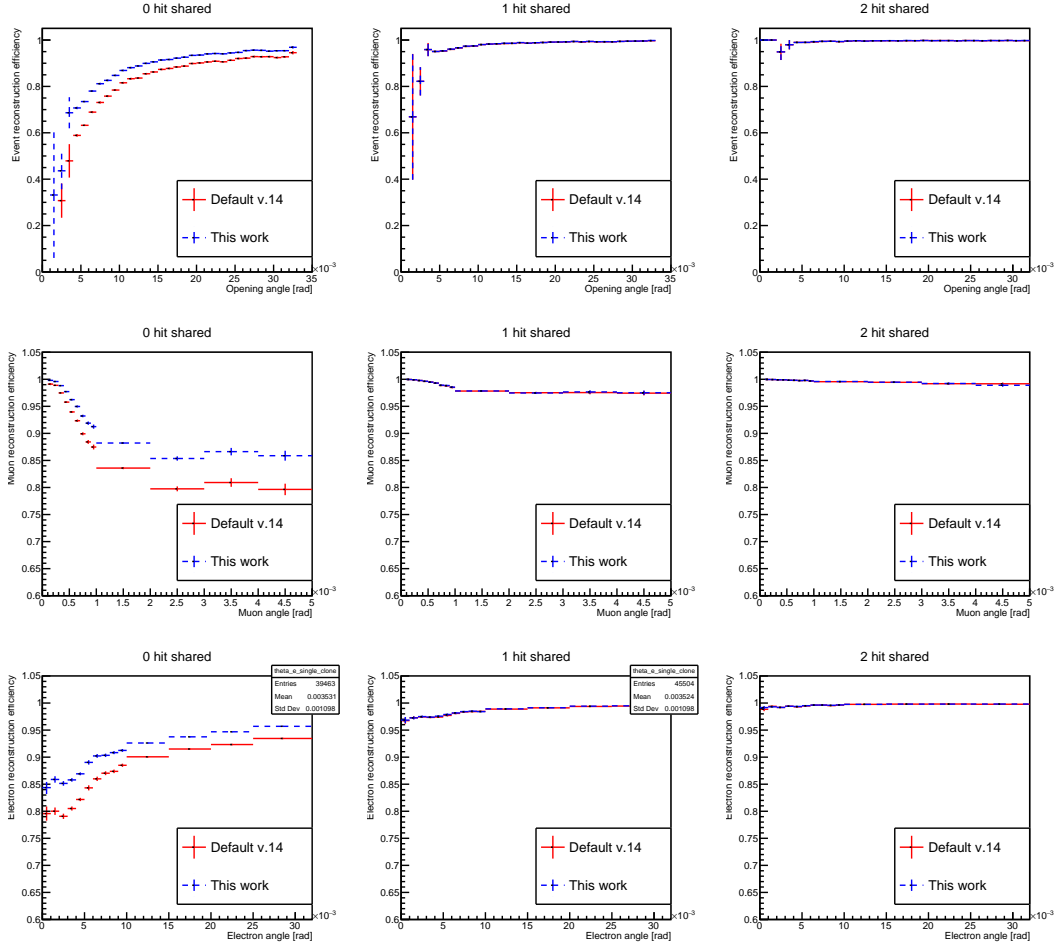


Figure 5.11: Elastic event (top row) reconstruction efficiencies as a function of the μe opening angle and single-particle efficiencies for muon (middle row) and electron (bottom row) as a function of the lepton scattering angle. Different settings for the maximum hit sharing parameter are used: 0 hit (left column); 1 hit (middle column); 2 hit (right column). The red points correspond to the default FairMUonE reconstruction algorithm, the blue ones to the updated version.

an impact on pattern recognition. Fig. 5.12 shows the results for the setting of zero hit sharing. There is still an improvement with the updated algorithm in the large θ_e region (large opening angles), where MS has a larger impact. Thus, even without misalignment it may happen that the electron track is not reconstructed because of the loss of the correct hit, preferring to share the closest one belonging to the muon.

It has also been tested that this gain in efficiency preserves the quality of the reconstructed tracks. Both the angular resolutions of the reconstructed particles and the χ^2

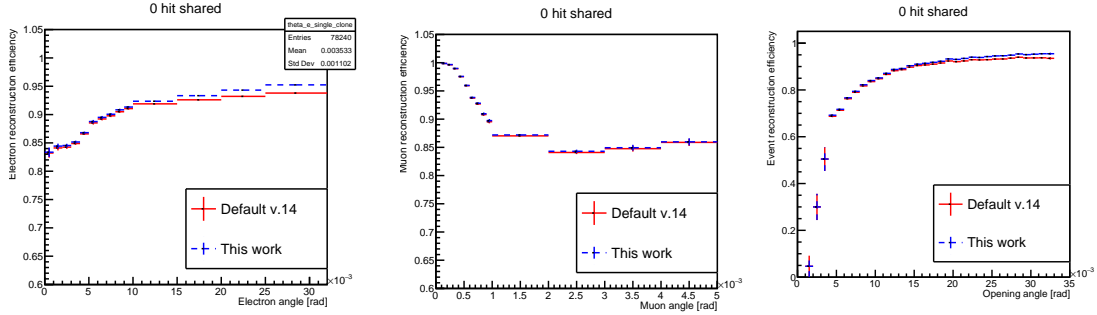


Figure 5.12: Single-particle reconstruction efficiency for electron (left) and muon (middle) as a function of the lepton scattering angle; event reconstruction efficiency as a function of the μe opening angle (right). Reconstruction setting for zero hit sharing. The red points correspond to the default FairMUonE reconstruction algorithm, the blue ones to the updated version.

of the latter are not worsened by this modification. More details can be found in Appendix D.

The reconstruction is now performed using the new algorithm and data/MC ratios as

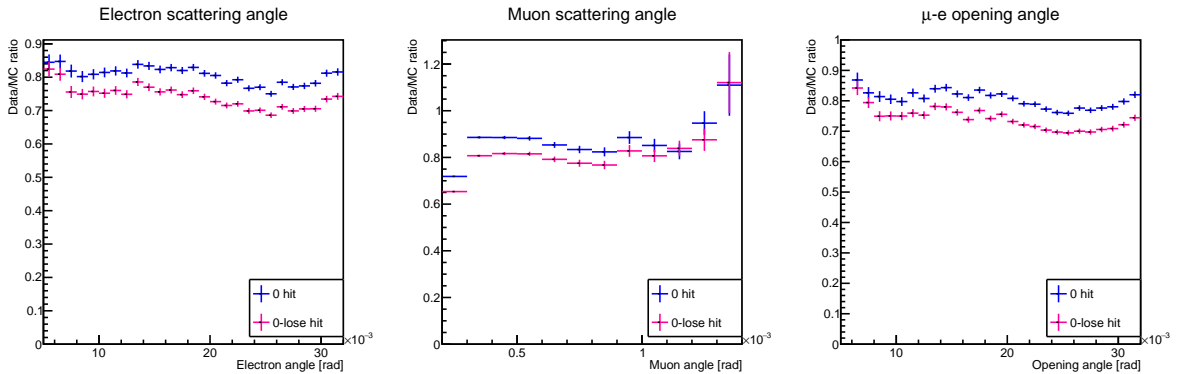


Figure 5.13: Ratio of data and MC events passing the elastic selection as a function of electron angle (left), muon angle (center) and relative opening angle (right). Here the default FairMUonE reconstruction with loose 0-hit sharing parameter (pink) is compared with the updated algorithm with 0-hit sharing (blue).

a function of the scattering and opening angles are shown in Fig. 5.13. The ratio increases by approximately 10% with the updated algorithm. Many more events are now successfully reconstructed, whereas they were previously lost with the default algorithm. Additionally, the behavior of the ratios is now more uniform than before. The events that were lost, as seen Fig. 5.6, i.e. where the distance between stereo hits of the muon and electron is smaller than ~ 2 mm, are now successfully reconstructed, as it is evident

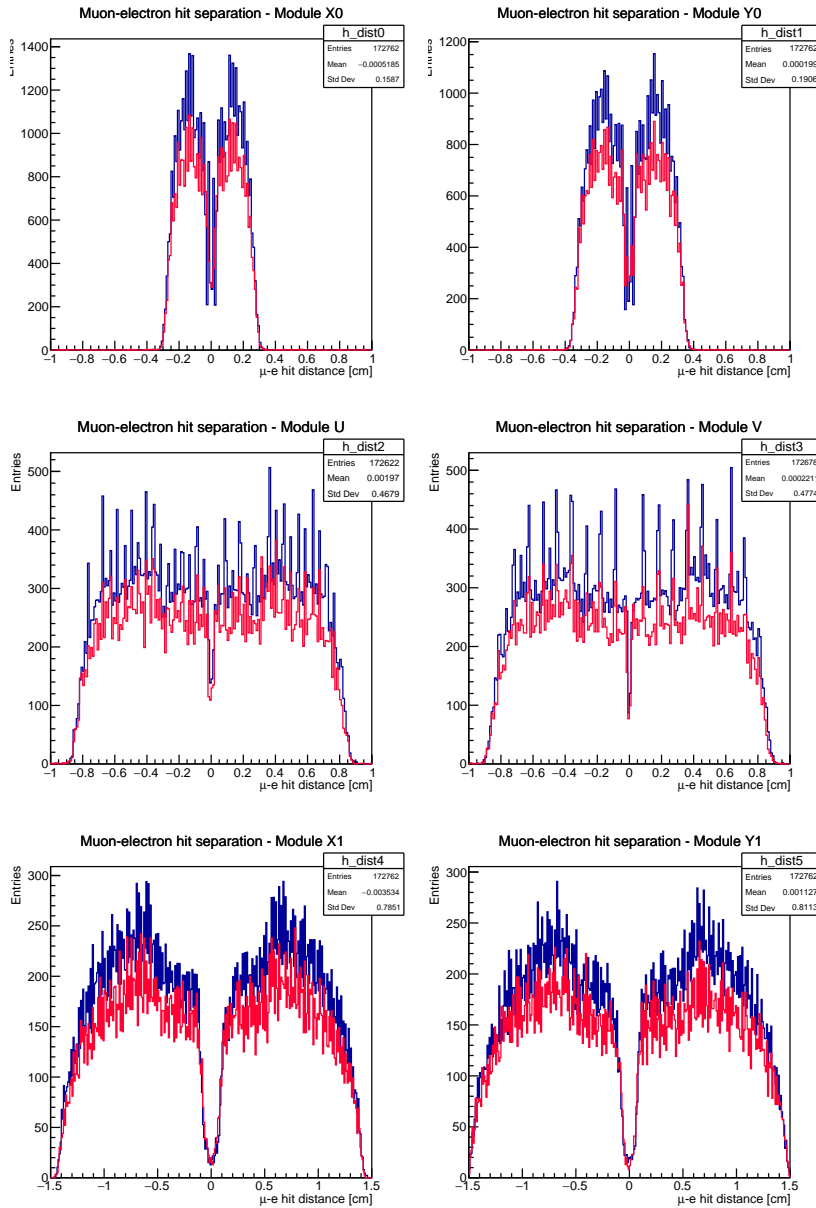


Figure 5.14: Distance between the stubs assigned to muon and electron track for each module with the modified reconstruction algorithm. First row corresponds to first two modules X0 and Y0, second row to stereo modules U and V, third row to last modules X1 and Y1. In blue MC while in red real data.

from Fig. 5.14. Real data and MC are now much more compatible and the dips seem to have disappeared.

The highest and most uniform reconstruction efficiency in MC simulations is achievable with the parameter setting for two-hits sharing (see Section 3.2.1). Consequently, the reconstruction using the new algorithm has also been tested with two shared hits. The results for the data/MC ratios are shown in Fig. 5.15. While a decreasing trend is still observed at small opening angles, there is an overall efficiency gain of approximately 10%

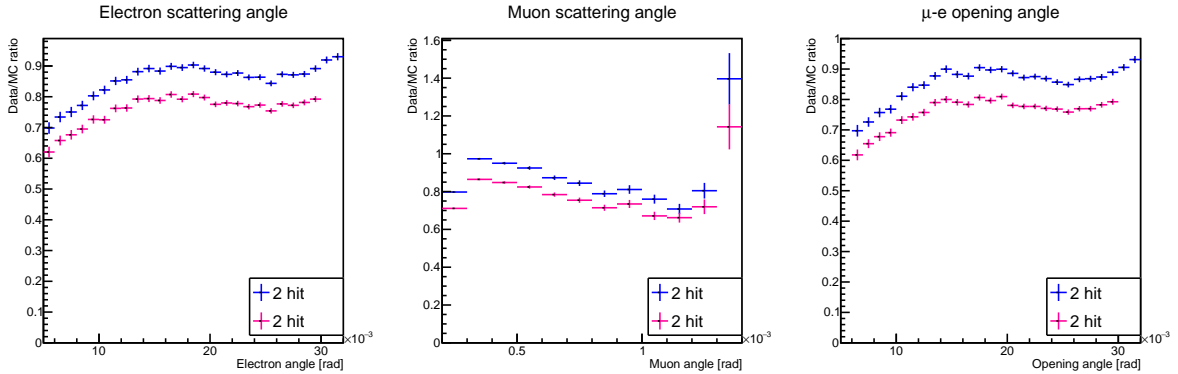


Figure 5.15: Ratio of data and MC events passing the elastic selection as a function of electron angle (left), muon angle (center) and relative opening angle (right). Here the default FairMUonE reconstruction (pink) is compared with the updated algorithm (blue). In both cases the reconstruction has been made with allowed 2-hit sharing.

across the entire kinematic range.

The study conducted so far aims to compare the absolute event yield within the elastic selection to the predictions from MC simulations, considering the absolute luminosity of the analyzed run. To assess the level of agreement, one must consider the probability of having two tracks with at least five stubs each, without any shared hits -thus independent-, in order to account for detector efficiencies. Having Eq.4.1:

$$\epsilon_{2tracks} = \epsilon_{track} \times \epsilon_{track} = 0.850 \pm 0.035, \quad (5.9)$$

considered the measured modules efficiency of $(98.0 \pm 0.5)\%$. Given the 0-hit shared configuration, the observed blue ratios in Fig. 5.13 seem to account correctly for the expected two tracks efficiency. If one focuses on the region $5 < \theta_e < 20$ mrad, the ratio between the integrals is found to be:

$$\frac{N_{data}}{N_{MC}} = \frac{92951}{113261} = 0.821 \pm 0.005, \quad (5.10)$$

in agreement with the expected event detection efficiency evaluated in Eq.5.9

5.1.2 Comparison of the shapes

A first comparison of the shape of the angular distributions is done in the region of $5 < \theta_e < 20$ mrad, using the zero-hit setting, where the ratios are more uniform. For such comparisons, the normalization is done scaling the MC distributions to the same number of real data events.

Some variables before and after the elastic selection (second paragraph of Section 5)

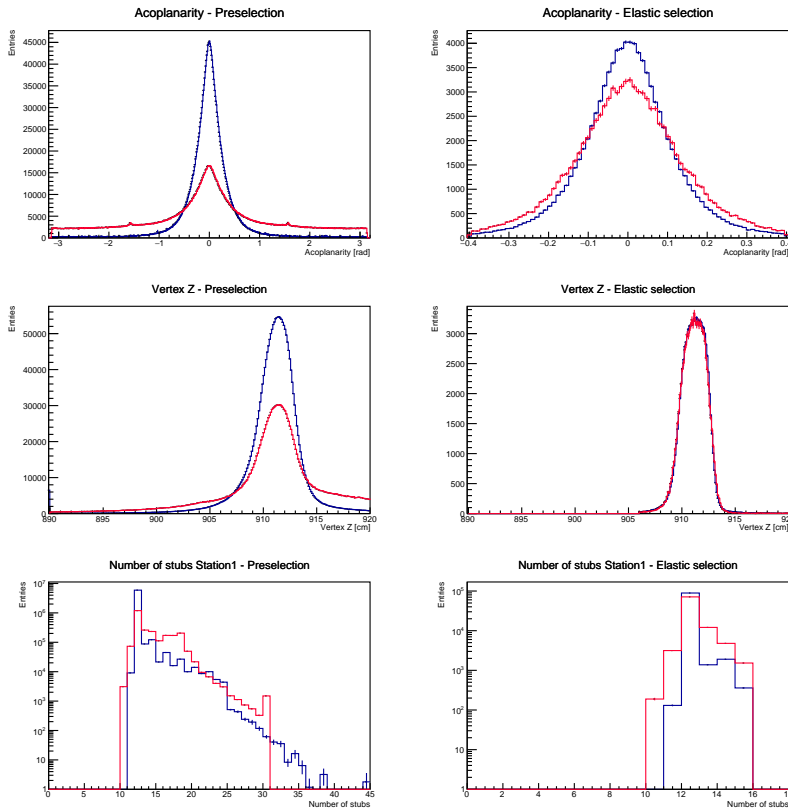


Figure 5.16: Distributions of relevant variables before (left) and after (right) the elastic selection: acoplanarity (top row), longitudinal vertex position (middle) and number of tracker hits after the target. Real data (red histogram) is compared with MESMER simulation (blue histogram) normalized to the data.

are compared in Fig. 5.16. The acoplanarity, the longitudinal position of the vertex and the number of hits in the second station are shown for both data and MC. After the elastic selection, the agreement between data and MC increases. Assuming that MESMER accurately describes radiative processes, the acoplanarity plot after selection reveals differences in angular resolution between data and MC, as has already emerged in other studies.

The reconstruction has been made with the new version of the algorithm, discussed in the last Section, with the setting of zero hit shared. The angular distributions and the data over MC ratios are shown in Fig. 5.17, where the MC sample is normalized to the data integral after the elastic selection. This allows for the examination of differences in the shapes of the distributions, which are plotted on the left side. While the ratio as a function of electron angle remains within $\pm 3\%$ across the entire range, this is not the case for the muon, particularly in the low θ_μ region. As previously mentioned, an inaccurate description of the angular resolution introduces large distortions that increase with the size of the systematic. Currently, first studies estimate about a 30% difference in the intrinsic angular resolution between real and simulated data. The θ_e cut at 20 mrad introduces the distortion on the muon distribution at low angle. This distortion in the range $0.3 < \theta_\mu < 0.5$ mrad was not observed in Fig. 5.13, as the cut on θ_e was set to

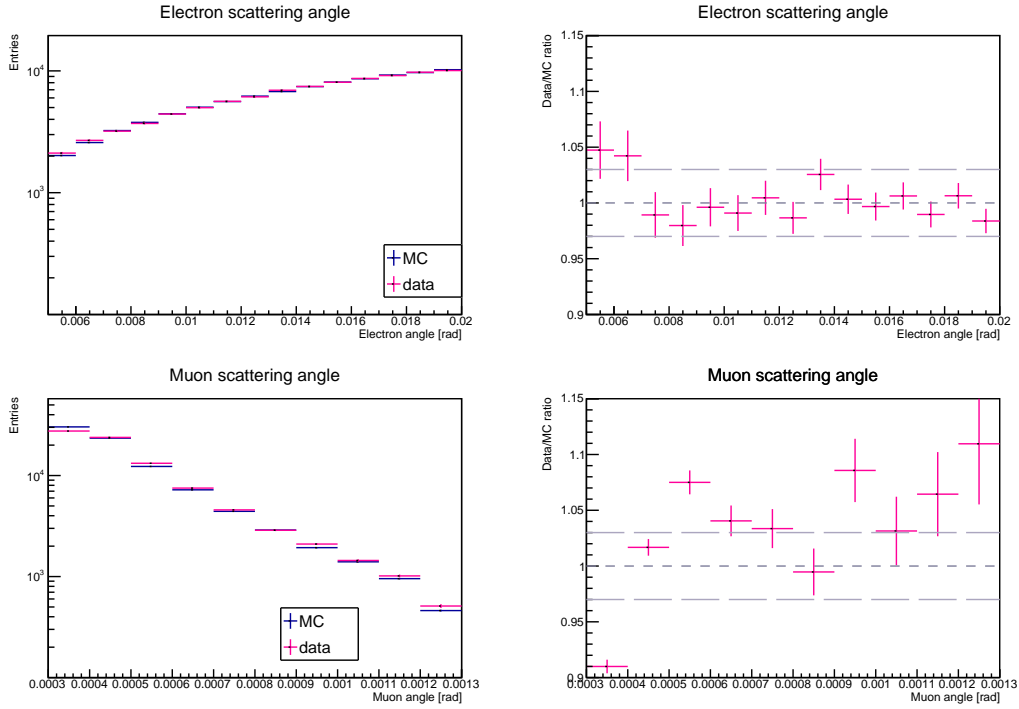


Figure 5.17: Left plots are the distribution of electron (top) and muon (bottom) scattering angle for data and MC, normalized to the data. Right plots are ratios of data and MC. The gray dashed lines mark the unit ratio and a band of $\pm 3\%$.

32 mrad. This suggests that the distortion is correlated with the cut, and thus, with the angular resolution. As reported in [51], distortions on θ_μ are considerably more complex than those affecting the electron. Thus, a more detailed analysis is needed.

The level of expected background remaining after the elastic selection has been evaluated with a Geant4 minimum bias sample, as MESMER signal samples does not contain any type of background processes except for events with radiated photons. Indeed, the long tails in the acoplanarity distributions of real data in Fig. 5.16, before the elastic selection are not described by the MESMER signal MC. Instead, in Fig. 5.18, the same acoplanarity distributions are compared to a minimum bias sample, where the real data tails seem to be correctly described before the elastic selection. The level of background with respect to the signal one is estimated with the minimum bias to be $< 0.2\%$. Therefore, this systematic error on data/MC shapes comparison is negligible with respect to the final error found in the current analysis.

Geant4 is a powerful tool to control the results that are obtained with MESMER gener-

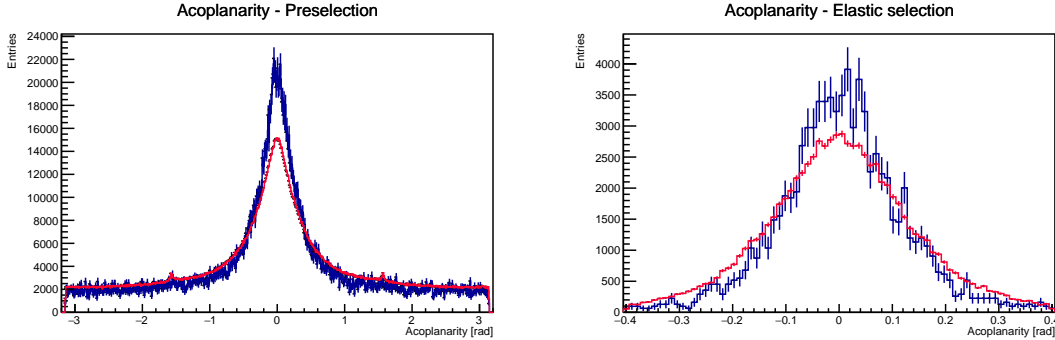


Figure 5.18: Acoplanarity distributions before (left) and after (right) the elastic selection for real data (red) and a minimum bias MC simulation (blue) with a MC minimum bias sample. The normalization is to the number of real data events.

ators. However, at the moment $data/MC$ ratios with minimum bias results to be:

$$\frac{N_{data}}{N_{minbias}} = 0.741 \pm 0.015, \quad (5.11)$$

which underestimates the expected ratio reported in Eq.5.9. However, it results to be within 3σ with the expected value with respect to it. The origins of that underestimation are still under study and more statistics is needed to continue investigating. Further details can be seen in Appendix C.

To start observing the running of alpha, the MC description of angular shapes needs to be within 0.5% of the corresponding data distributions. More work needs to be done to reach this accuracy level. Some ideas for possible improvements are discussed in the next section.

5.2 Future steps

Future steps have been thought in order to improve the MC description. On the reconstruction algorithm side, a new version is under development which includes the covariance matrix for treating MS as described in [57] during track fitting. The aim is to improve the quality of the vertexing, as MS is important for large θ_e and large θ_μ and an incomplete treatment of MS could impact the quality of the tracks and vertex, thus the elastic selection. This version is still under validation.

Another important improvement regards the alignment. At the moment, the measurement direction of a module (e.g. X module) is defined as

$$\vec{v}_{dir} = [R_Z(\alpha + \alpha_{offset}) \cdot R_Y(\theta + \theta_{offset})] \cdot \begin{pmatrix} 1 \\ 0 \\ 0 \end{pmatrix}, \quad (5.12)$$

where the first matrix rotates around Z to adjust the strip orientation α , while the second one produces the tilt angle θ , by rotating around the strip axis. Both of them are reported with their respective alignment offsets α_{offset} and θ_{offset} . A third rotation, around the module axis, is missing. Introducing this third rotation by an angle γ will enable to fully describe any module orientation in space such that:

$$\vec{v}_{dir} = [R_Z(\alpha + \alpha_{offset}) \cdot R_X(\gamma + \gamma_{offset}) \cdot R_Y(\theta + \theta_{offset})] \cdot \begin{pmatrix} 1 \\ 0 \\ 0 \end{pmatrix}. \quad (5.13)$$

It has been verified that the introduction of the full 3D geometry in track fitting will allow the alignment procedure to correct the tilt angle, which until now was considered the main weak mode. As the problem described in previous section is strictly related to incomplete alignment, it may benefit from this new procedure, which is being integrated in the FairMUonE software.

The tilt angle was introduced in the first and last $x - y$ pairs of modules. As discussed in Section 2.5.1, it was demonstrated in MC simulations that it improves the single hit resolution of 2S modules [45]. Although real data observations indicate that the cluster of fired strips is wider for tilted modules (Section 4.2), its introduction in a real system has brought several challenges. Adjusting tracking equations appears to address the alignment issue, but this approach and its implications are still under investigation. At this stage, it is not possible to draw definite conclusions regarding the ability to achieve accurate alignment for this angular variable. Nonetheless, it is crucial to verify this aspect, as it could lead to a decision to eliminate tilted modules in future tests, considering also the drawbacks discussed in Section 3.2.3.

The problem discussed in the previous section is particularly pronounced at small opening angles. In this kinematic range, hit sharing is expected to increase the reconstruction efficiency, as demonstrated by the MC study presented in Section 3.2.1. However, when dealing with real data, it may be difficult to be handled properly. Hit sharing is currently essential due to the system's limited redundancy, with only two X and two Y planes for the straight track to pass through. Therefore, if one of the two hits is missing, the nearby hit from the other track may be used to help reconstructing the track, provided it is sufficiently close. An important and urgent study deals with tracker configuration in terms of number of modules. Adding an extra layer per view could maximize reconstruction efficiency decreasing the number of hits shared. In this scenario, if one of the three hits is lost, two out of three stubs per view would still be available, allowing a track to be defined without the need to share hits with other tracks.

Another important study is the one about the angular resolution. As already mentioned in the previous section, a distortion of the *data/MC* ratio is expected if the resolution is not well described in MC [51]. First studies have been done estimating a systematic difference of about 30% in the intrinsic angular resolution, although this is still an ongoing measurement, that will progress and benefit from the implementation of the alignment

algorithm discussed above.

Chapter 6

Conclusion and outlooks

The anomalous magnetic moment of the muon remains one of the central open questions in contemporary particle physics. As experimental precision increases, theoretical and experimental investigations continue to progress, setting the stage for deeper insights. One of the promising future developments is the MUonE project, designed to directly probe the main contribution to the theoretical uncertainty, with a new method and high accuracy.

This thesis presented a comprehensive overview of the MUonE proposal, focusing on the advances made in the past three years. The primary work concentrated on the validation and performance study of the project's simulation and reconstruction software. A thorough assessment of critical operational parameters, including tracking efficiency and angular resolution, was conducted. This analysis helped identify an optimal configuration for reconstruction, enhancing the system's accuracy and reliability. A preliminary analysis with the optimized configurations was also initiated on data collected during the 2023 test beam. These early results provide valuable insights and mark a significant step towards achieving MUonE's ambitious objectives. Continued work in refining these parameters, alongside new data, will likely yield further advances and contribute substantially to our understanding of the muon's magnetic properties.

The study on the optimal reconstruction configuration in MC simulations revealed that allowing up to two shared hits between tracks achieves the highest reconstruction efficiency, approximately 99%, across the full kinematic range for both single particle and elastic event reconstruction. This finding was instrumental in preparing for the analysis of real data. However, when this configuration was applied, different challenges arose. Issues in pattern recognition and alignment became apparent, leading to a non-uniform data/MC ratio, shown in Fig. 5.4. Additionally, an inefficiency emerged in reconstructing events with a specific topology, namely for tracks with close-by hits in the U/V planes (Fig. 5.6). To address these complexities, a modification to the pattern recognition algorithm was proposed. This update aims to upgrade the algorithm's logic, better accommodating the more intricate conditions of real-world data and improving overall

reconstruction performance. This proposed modification has been validated in MC simulations, where it maintained consistent reconstruction efficiency (Fig. 5.11). Notably, the adjustment improved the efficiency in the large θ_e region without compromising the angular resolution. In application to real data, the updated algorithm achieved a uniform data/MC ratio with zero shared hits, as demonstrated in Fig. 5.13. Additionally, the modification recovered over 10% of events with two shared hits, which were previously lost under the default reconstruction algorithm. However, despite these improvements, uniformity issues persist in regions with small lepton opening angles, as observed in Fig. 5.15.

A restricted kinematic region, specifically $5 < \theta_e < 20$ mrad, was analyzed using the zero hits shared configuration, yielding a more uniform data/MC ratio within this range. The projected tracking efficiency for μe elastic events in this configuration is 0.850 ± 0.035 , assuming a detector module efficiency of 0.980 ± 0.005 . The achieved ratio between event yields in data and the MC expectation, after the elastic selection, 0.821 ± 0.005 , aligns well with the expected tracking efficiency reported.

A preliminary comparison of the MC and data shapes for the angular distributions of electrons and muons was performed using the configuration with zero shared hits, which yielded the most uniform data/MC ratio. Although this setup enhances data uniformity, at present it does not provide optimal MC reconstruction efficiency and must be further refined to aim for future measurements of the angular distributions.

However, it aids in examining systematic effects, such as angular resolution and multiple scattering, which can distort distribution shapes. This comparison showed that the normalized data/MC ratio for the electron angular distribution remains within $\pm 3\%$. In contrast, the muon distribution exhibited greater fluctuations, some of which could stem from the angular cut applied to the scattered electron at $\theta_e < 20$ mrad. According to previous studies [51], a systematic error on the angular resolution of 10% may introduce significant distortions in the angular distributions. For the running of $\alpha(t)$ to be observed, the MC description of angular shapes must be accurate to within at least $\pm 0.5\%$. Looking forward, various improvements to reconstruction and analysis pipeline are planned. One priority is alignment. New tracking equations will soon be employed to address the tilt angle alignment, which has been identified as a primary weak mode in data reconstruction. Since pattern recognition closely depends on alignment quality and is crucial for accurately reconstructing real data events, this change could substantially improve reconstruction performance and data/MC consistency. Additionally, an upcoming release of the reconstruction algorithm will integrate refined MS correction terms in track fitting, as detailed in [57]. This update is expected to enhance both vertex reconstruction accuracy and post-vertex track fitting, allowing for a more precise and optimized elastic event selection.

Another important consideration for future tests involves the layout of tracking stations. Key decisions include whether to maintain module tilt and whether to add two additional tracking layers, one for the X view and one for the Y view. The advantages

of tilt have been confirmed in both MC simulations[45] and real data 4.2. However, tilt introduces some limitations, notably in calculating the bend in tilted modules (Section 3.2.3), which can affect elastic event reconstruction for specific topologies. A partial solution has been found: correctly tuning the window offset in the correlation layer of the 2S module can mitigate these issues, although a maximum offset of ± 3 strips, imposed by the current tracker electronics, results in $\sim 6\%$ of events being misreconstructed. Excluding bend information could recover this $\sim 6\%$, though this may compromise resolution. Furthermore, using only one of the two 2S module sensors to determine particle position brings to have unused extra silicon material, potentially impacting measurement accuracy. Several options are open regarding the tracking station layout and the use of tilt in X and Y modules:

1. Removing tilt in X and Y modules: this would allow correct usage of bend information, fully exploiting the available data. This approach could simplify alignment without the complications of the tilted geometry;
2. Reducing material budget with 1S modules: Another option is to adopt modules with a reduced material budget. One promising prototype currently in development is the 1S module, which, based on the 2S model, incorporates a single sensor instead of two. The reduced material budget in these modules helps minimize multiple scattering effects. Additionally, bend information is absent in this configuration. However, the 1S module is still under testing and this option should be developed together with the idea of having additional modules per view;
3. Exploring pixel detectors: Pixel detectors present another promising alternative, as they can meet MUonE requirements by incorporating 3D position information within a single module, thus minimizing material while preserving information density. Current pixel detector technology can achieve better position resolution with respect to that of 2S modules, making it a strong candidate for future detector designs.

A key consideration about tilt depends on the effectiveness of the new alignment algorithm. If the algorithm can effectively align the weak tilt mode, the primary drawback of tilt could be resolved. However, if alignment proved to be challenging, removing tilt would simplify the system's configuration, though it may reduce position resolution to the nominal pitch/ $\sqrt{12}$. In this scenario, increasing the number of modules could compensate for the resolution loss, as track resolution improves with additional layers. Although adding modules may increase multiple scattering, the extra layers would benefit the pattern recognition algorithm, improving track reconstruction accuracy. This thesis has demonstrated the utility of hit sharing in recovering events that would otherwise be lost. Hit sharing, while useful in MC simulations, can be less reliable in real data. Adding more layers per view would improve tracking efficiency by enhancing track

reconstruction quality and reducing the probability of hit sharing. Furthermore, additional layers would benefit the 2D combination track step described in Section 3.1.2, as a larger number of layers would help reduce the pool of viable 2D track building, thus refining the reconstruction process.

Appendices

Appendix A

Automatized workflow with Snakemake

The tests and validation workflow is divided in different steps:

1. Six different samples of elastic events are generated at the MC level with MESMER generator. Those are divided per kinematic regions, corresponding to θ_e intervals: $[0, 5]$, $[5, 10]$, $[10, 15]$, $[15, 20]$, $[20, 25]$, $[25, 32]$ mrad, each one containing the same number of events;
2. the reconstruction is run with a given geometry and a given configuration file (sets of parameters and flags);
3. after generation and reconstruction, ROOT macros are run on the reconstructed samples to evaluate reconstruction efficiency and angular resolution;
4. it is possible to generate efficiency and resolution plots comparing different versions of FairMUonE or different reconstruction configurations.

The Snakemake workflow management system [56] is a tool to create reproducible and scalable data analyses. As the tests and validation workflow for FairMUonE contains a multitude of heterogeneous steps, from the application of various command line tools to the usage of ROOT macros for the generation of plots, this tool resulted to be an optimal solution for reproducing these steps with just one click, exploiting parallelization when possible.

Fig. A.1 shows for illustrative purposes some of the plots resulting from the automated testing procedure corresponding to the comparison of two different configurations of the reconstruction algorithm. One version of the reconstruction in this example determines the interaction vertex assuming the z vertex position in the middle of the target, the other one determines the z position of the vertex as the distance of closest approach (DOCA) of the two outgoing tracks. These plots represent the reconstruction efficiency

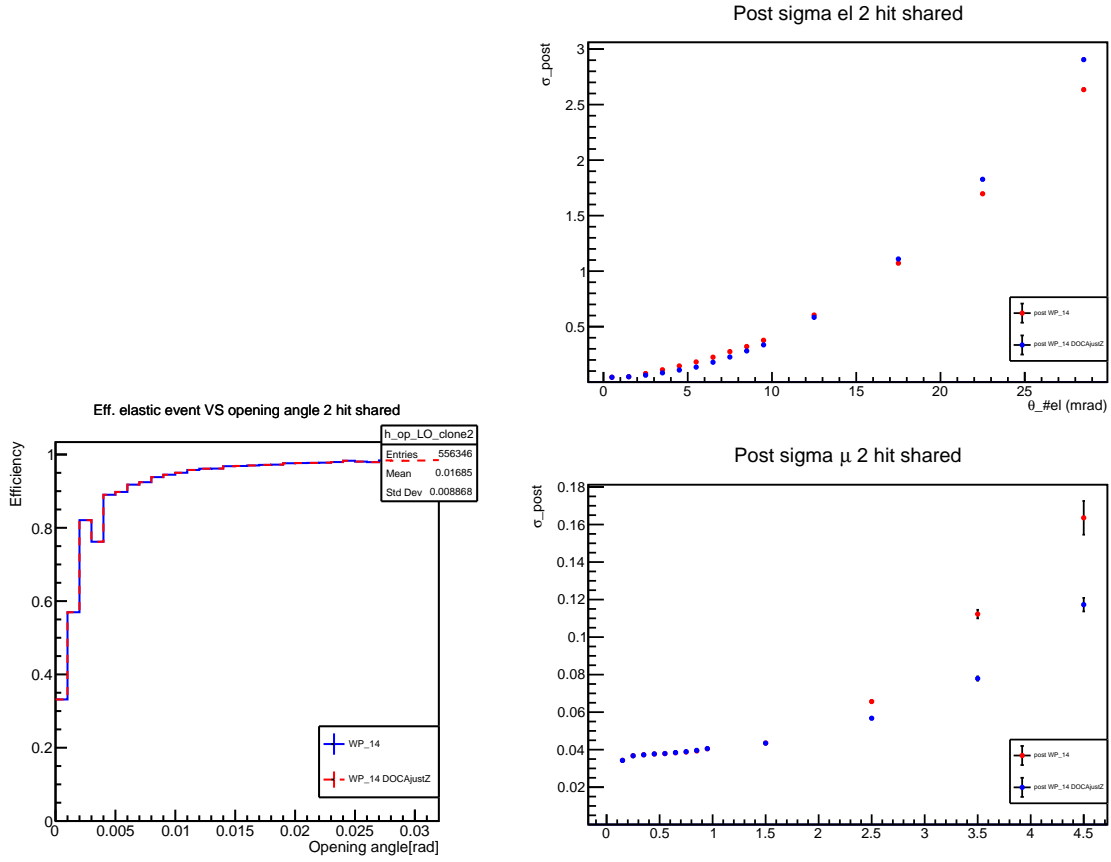


Figure A.1: *Left*: reconstruction efficiency of an elastic event as a function of the opening angle between the outgoing electron and muon. *Right*: Angular resolution as a function of the electron (top) and muon (bottom) scattering angle. Results achieved by constraining the vertex longitudinal position to: the middle of the target (red), or to the Z position determined from the DOCA minimization (blue).

of the algorithm for Monte Carlo elastic events when allowing for 2 shared hits among tracks and the resulting angular resolution that can be achieved in the two cases. Thanks to this tool, changes between different configurations, new releases of the code, various settings of the parameters, can be effectively spotted.

In Fig. A.2, the variable $\frac{\sigma_{post} - \sigma_{pre}}{\sigma_{pre}}$ is presented, which shows whether the post-vertexing track fits improve the angular resolution in comparison with the pre-vertexing fits.

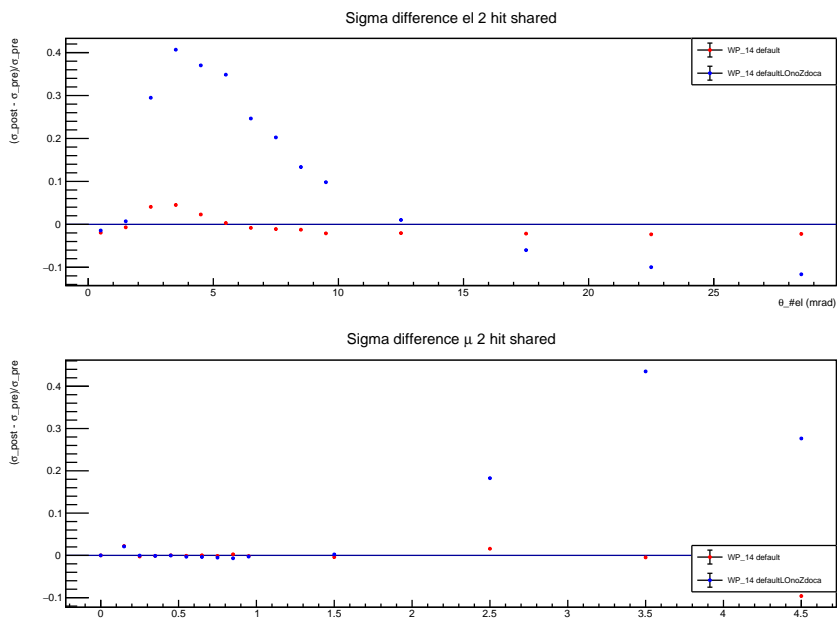


Figure A.2: Fractional difference between resolution from the pre-vertexing fit and post-vertexing fit as a function of electron (top) and muon (bottom) scattering angles. Results compare track fitting with vertex constrained to the Z position of: the middle of the target (red) or the position from the DoCA fit (blue).

Appendix B

First background studies with minimum bias simulation

A sample of Geant4 minimum bias events have been simulated with a monochromatic muon beam of 160 GeV in a geometry with two stations and one carbon target of 1 cm. The outgoing products from the pair production background typically include one muon and two leptons, primarily an electron and a positron. However, it is possible that one of the three leptons may not be reconstructed, with the electron or positron being the most likely candidates due to the effects of multiple scattering, especially given the low energy of the products. The majority of background events lie below $\theta_{min} < 0.2$ mrad, a basic cut to get rid of the most of the pair-production events as discussed in Section 2.3.1.

Another important cut is the one on the acoplanarity. This helps the selection as elastic scattering events are planar, with the outgoing muon and electron emitted in opposite directions in the transverse plane, conserving the transverse momentum. While pair-production may not conserve it. Fig. B.1 shows acoplanarity distributions comparing the pair-production background from a minimum bias simulation, with elastic signal obtained either from MESMER or from the same minimum bias simulation, without any cut applied. While the signal is well peaked within $(-1, +1)$ for both samples, the background is uniformly spread all over the range. This also gives a first proof of the consistency between MESMER and minimum bias signal, as the distributions are in agreement. As already discussed, one of the most effective cuts for background rejection is $\theta_{min} > 0.2$ mrad. Fig. B.2 shows acoplanarity distributions with the application of this basic cut. It is evident that the majority of pair-production events are rejected. Another additional cut is the quality of the reconstructed vertex, that was initially set to $\chi_{vtx}^2 < 100$. Some results can be given to quantify the effects of these cuts on signal and background events in a minimum bias sample, obtained from the simulation of 3×10^6 beam muons. Table B.1 shows the remaining background events after some cuts applied, followed by the remaining signal ones:

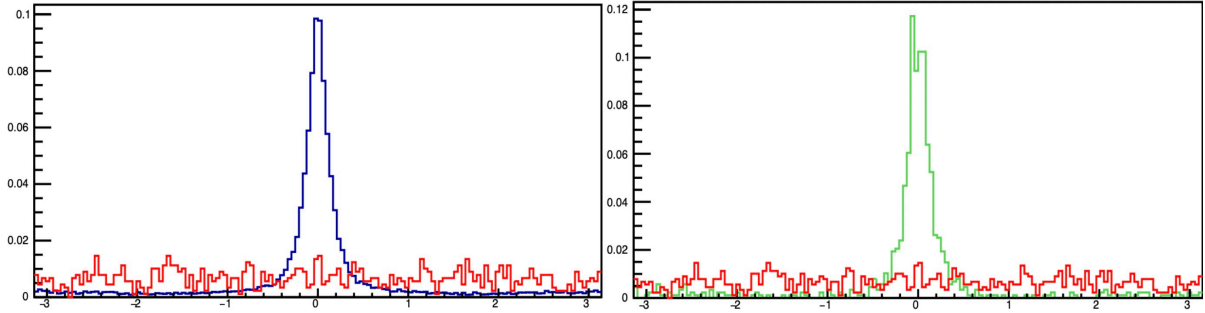


Figure B.1: Acoplanarity distributions for background (red) -obtained from a minimum bias sample- are compared with signal ones. The latter are obtained from a MESMER sample (blue, left) and from minimum bias sample (green, right).

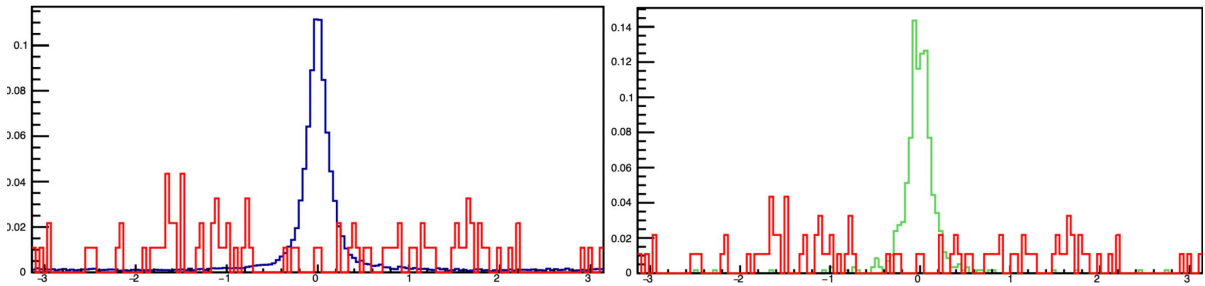


Figure B.2: Acoplanarity distributions for background (red) -obtained from a minimum bias sample- are compared with signal ones. The latter are obtained from a MESMER sample (blue, left) and from minimum bias sample (green, right). A cut on $\theta_{min} > 0.2$ mrad is applied to reject most of the background.

In Fig. B.3 and B.4 2D plots of the scattering angles of the two reconstructed particles ($\theta_{max}, \theta_{min}$) for a minimum bias sample are shown respectively for background and signal. Dealing with background, it can be noticed that the majority of the events surviving the elastic cuts are away from the elastic curve, while the selected signal ones follow it as expected.

From this first study the remaining background was estimated to be of the order of 10^{-3} after a basic elastic selection. This was one of the first studies that was done with minimum bias simulations. The selection can be refined; new studies are ongoing using more statistics and an updated version of the reconstruction code and these seem to point at the same level of background estimated from this first work.

BACKGROUND				
	No cuts	$\chi^2_{vrtx} < 100$	$ aco < 1$	$\chi^2_{vrtx} + aco $
All	0.03% (902)	0.0034% (104)	0.0096% (289)	0.0009% (27)
$\theta_\mu > 0.2 / , mrad$	0.003% (92)	0.0005% (16)	0.0009% (28)	0.0001% (3)
SIGNAL				
	No cuts	$\chi^2_{vrtx} < 100$	$ aco < 1$	$\chi^2_{vrtx} + aco $
All	0.029% (878)	0.018% (543)	0.026% (767)	0.018% (541)
$\theta_\mu > 0.2 mrad$	0.019% (584)	0.015% (450)	0.019% (576)	0.015% (449)

Table B.1: Remaining background and signal events after the application of several cuts.

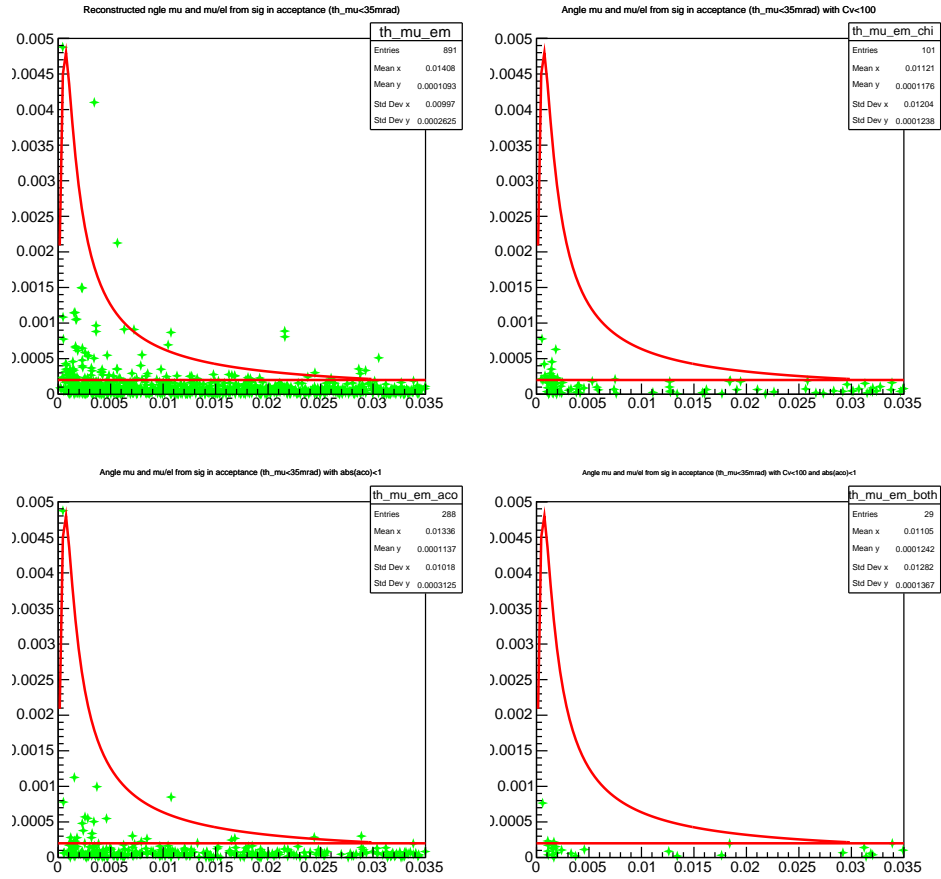


Figure B.3: 2D plot of the maximum VS minimum angle of scattering of two leptons reconstructed in a minimum bias sample with background events. The red curve represents the elastic curve, while the red line the basic cut $\theta_{min} > 0.2$ mrad usually applied to get rid of the majority of pair-production events. The effect of few selection cuts is shown: (top-left) all the background reconstructed events, (top-right) events after χ^2_{vrtx} cut, (bottom-left) events after $|aco| < 1$ cut and (bottom-right) events after both the vertex and the acoplanarity cut.

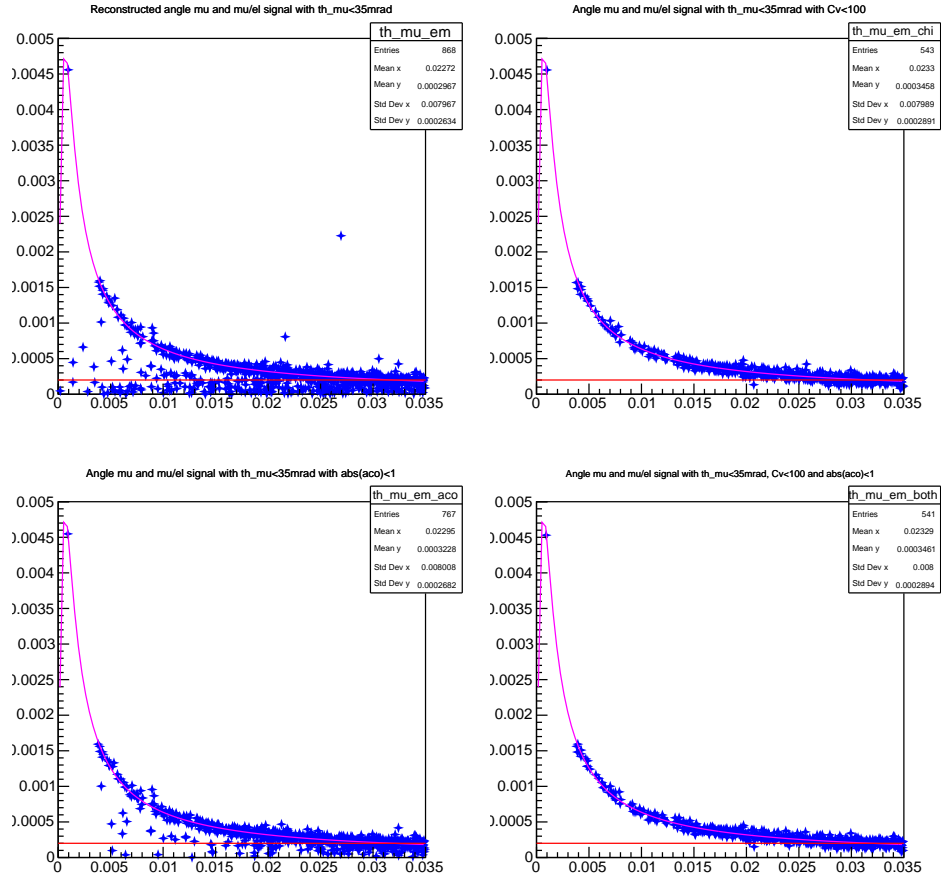


Figure B.4: 2D plot of the maximum VS minimum angle of scattering of two leptons reconstructed in a minimum bias sample with signal events. The red curve represents the elastic curve, while the red line the basic cut $\theta_{min} > 0.2\text{mrad}$ usually applied to get rid of the majority of pair-production events. The effect of few selection cuts is shown: (top-left) all the background reconstructed events, (top-right) events after χ_{vrtx}^2 cut, (bottom-left) events after $|aco| < 1$ cut and (bottom-right) events after both the vertex and the acoplanarity cut.

Appendix C

Comparison of data with minimum bias MC simulation

A sample of about 3×10^7 minimum bias events has been generated in the past months with the 2023 test run geometry: two tracking stations and 3 cm target of graphite. The fiducial and elastic cuts discussed in the first two paragraphs of Section 5 have been applied and the sample has been normalized to the number of events in real data. Fig. C.1 compares the acoplanarity, vertex position and number of hits found in real data with the minimum bias normalized plots.

The comparison of the shape is reported in Fig. C.2 where the angular distributions for MC and data are shown. The ratios are quite fluctuating in these ranges. Moreover $\frac{N_{data}}{N_{MC}} = 0.741 \pm 0.003$, which underestimates the expected two-tracks efficiency of Eq.5.9. The reasons of this underestimation are not clear yet. It may be related to statistical reason and more samples need to be generated. Another possibility is that the higher-order cross sections are not precise in Geant4, therefore radiative contributions might be underestimated. Further studies need to be performed.

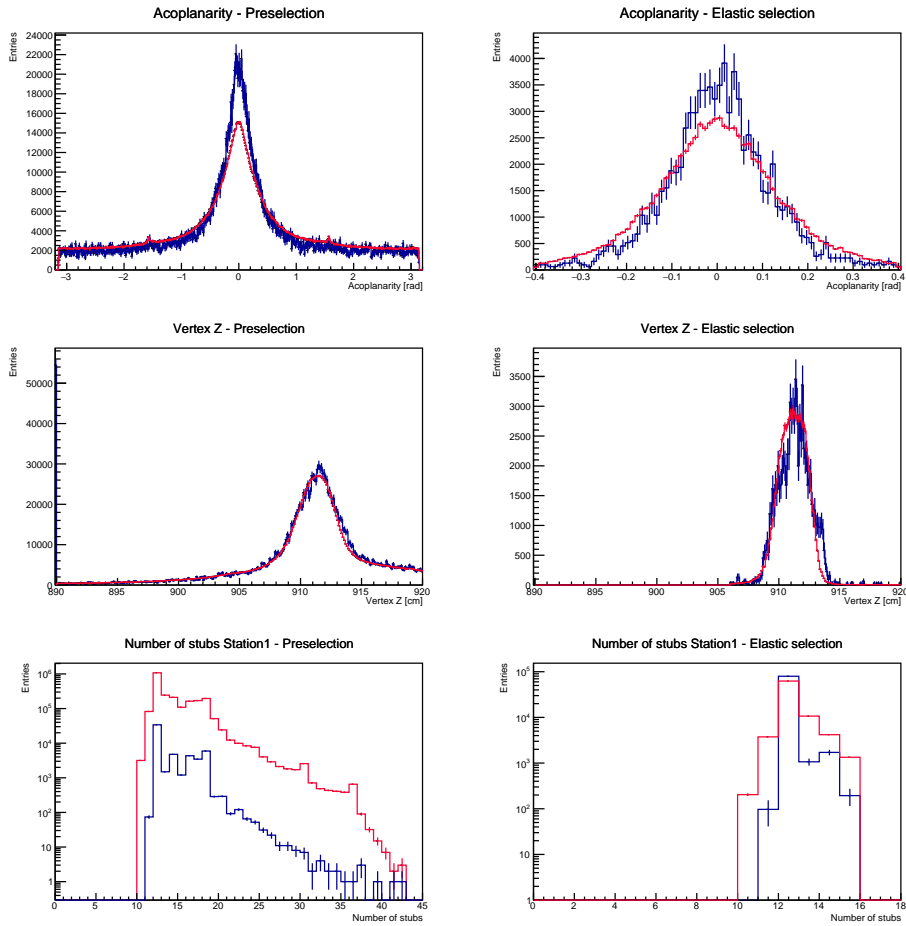


Figure C.1: Distributions before (left) and after (right) the elastic selection for data (red) and MC (blue). Acoplanarity (top), longitudinal vertex position (center), hits in the downstream station (bottom). The left side plots are obtained from preselected data with incoming muons passing the fiducial cuts; the right side plots include the elastic selection described in Sec.5.

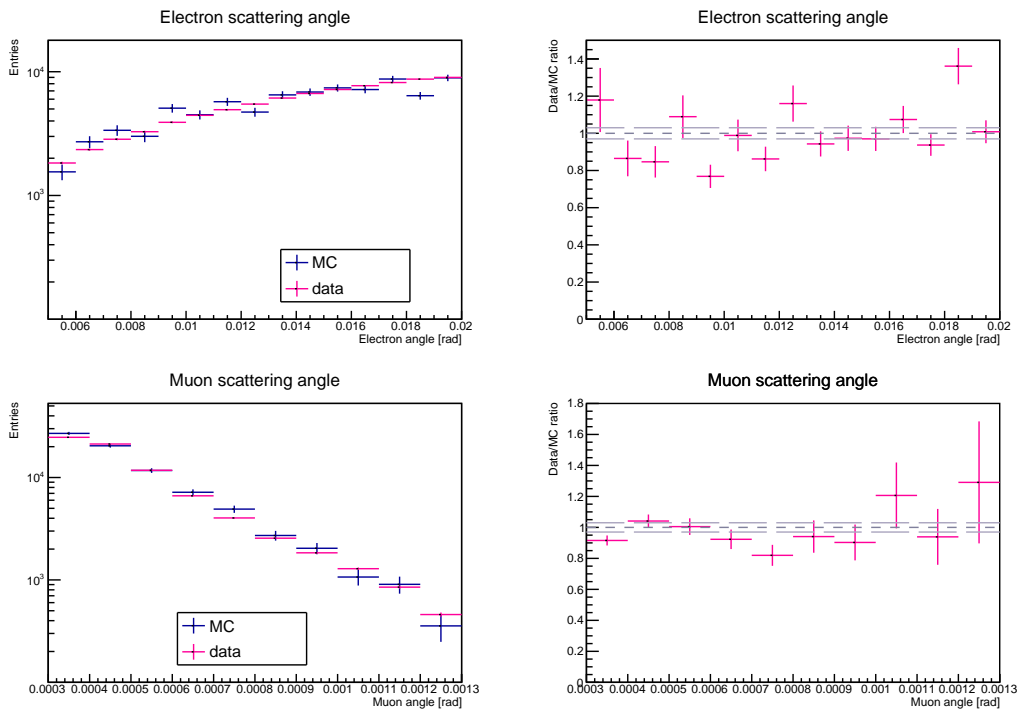


Figure C.2: Left plots are the distribution of electron (top) and muon (bottom) scattering angle for data (pink) and MC (blue). Right plots are the ratios and MC. The gray dashed lines mark the unit ratio and a band of $\pm 3\%$.

Appendix D

Angular resolution and track quality with improved reconstruction algorithm

Plots in Fig. D.1 represent the angular resolution of the muon and the electron before and after the vertex reconstruction, which implies a re-fit of tracks. No degradation seems to be introduced as the values in the new version (blue) and in the default one (red) are in agreement within the error bars.

Next step is to check that the quality of the tracks and of the vertex is not compromised. This is shown in Fig. D.2 (top row) for realistic MC. The vertex χ^2 is defined as the sum of the incoming and two outgoing tracks' χ^2 after a vertex has been found. One can notice the the quality of the tracks is stable, so this modification is increasing the efficiency of reconstruction without worsening the quality.

Major benefits are visible looking at real real data in Fig. D.2 (bottom row). It can be noticed that the major improvement is for the electron track. The mean normalized χ^2 value obtained with the new version is $\langle \chi^2 \rangle = 6.454$, while for the default version it was $\langle \chi^2 \rangle = 6.818$. In addition, the plots are made starting from the same sample of real data. Looking at the statistics, it is clearly visible an increase of the number of reconstructed events if the sample is reconstructed with the new algorithm.

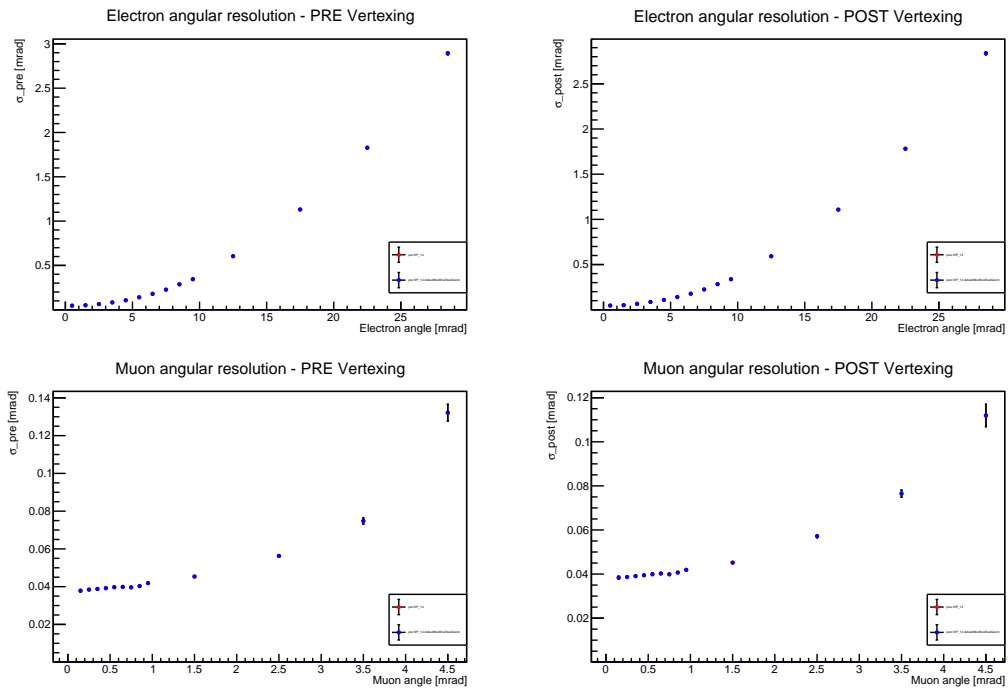


Figure D.1: Angular resolution of the electron (top plots) and of the muon (bottom plots) as a function of their scattering angles. FResults are shown before vertexing (left column), and after the refit at vertex (right column), for the reconstruction setting with zero hit shared. The default FairMUonE reconstruction (red) is compared to the new version of the algorithm (blue).

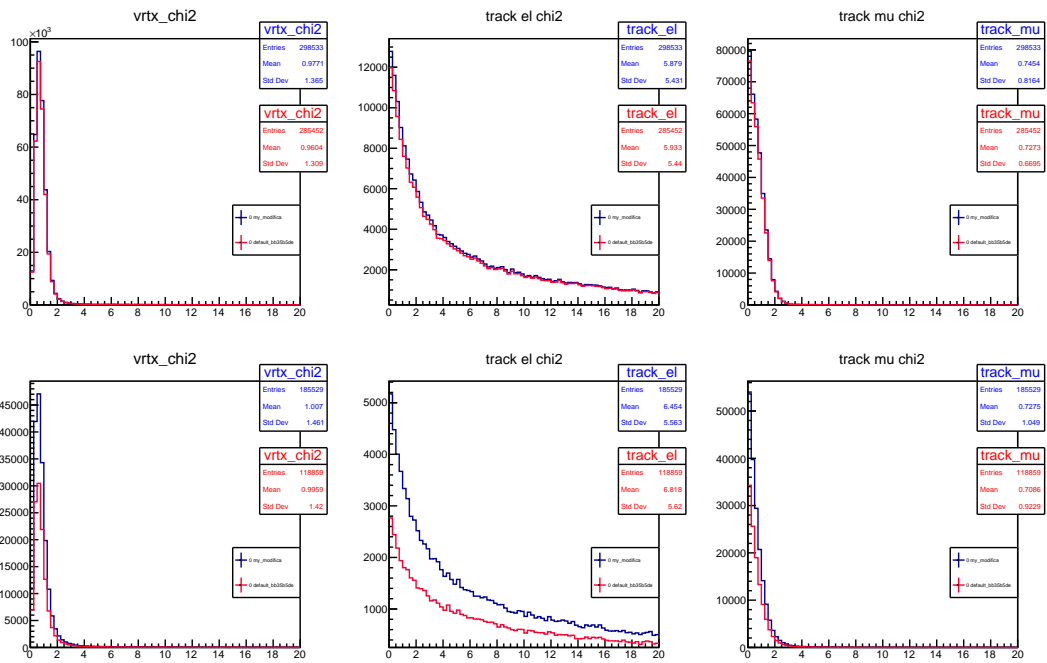


Figure D.2: Distributions of the normalized χ^2 of the vertex (left), electron track (middle) and muon track (right). Top row is for MC and bottom row is for real data. The results are obtained with the default FairMUonE reconstruction (red histograms), and the new algorithm (blue histograms).

Bibliography

- [1] S.H. Neddermeyer, and C.D. Anderson; *Note on the Nature of Cosmic-Ray Particles*, *Phys. Rev.* **51** (1937) 884, <https://doi.org/10.1103/PhysRev.51.884>
- [2] C. Street, and E.C. Stevenson; *New Evidence for the Existence of a Particle of Mass Intermediate Between the Proton and Electrons*, *Phys. Rev.* **52** (1937) 1003, <https://doi.org/10.1103/PhysRev.52.1003>
- [3] J.M. Conversi, E. Pancini, O.Piccioni; *On the Disintegration of Negative Mesons*, *Phys. Rev.* **71** (1947) 209, <https://doi.org/10.1103/PhysRev.71.209>
- [4] C. Latters et al.; *Process Involving Charged Mesons*, *Nature* **159** (1947) 694-697, <https://doi.org/10.1038/159694a0>
- [5] W. Gerlach, O. Stern; *Der experimentelle Nachweis des magnetischen Moments des Silberatoms*, *Zeitschrift fr Physik* **8** (1922) 110-111, <https://doi.org/10.1007/BF01329580>
- [6] G. Uhlenbeck and S. Goudsmit; *Spinning Electrons and the Structure of Spectra*, *Nature* **117** (1926) 264-265, <https://doi.org/10.1038/117264a0>
- [7] P. Zeeman; *On the influence of magnetism on the nature of the light emitted by a substance.*, *Philosophical Magazine* **43** (1897) 226-239, <https://commons.princeton.edu/josephhenry/wp-content/uploads/sites/71/2021/01/Zee-man-Philosophical-Magazine-1897.pdf>
- [8] P.A.M. Dirac, and C.D. Anderson; *The quantum theory of the electron*, *Royal Society* **117** (1928) 778, <https://doi.org/10.1098/rspa.1928.0023>
- [9] C. G. Tully; *Elementary Particle Physics in a Nutshell*, *Princeton Univ Press* (2012) <https://press.princeton.edu/books/hardcover/9780691131160/elementary-particle-physics-in-a-nutshell?srsltid=AfmB0oqX2fCn3YEw32Rc-bUz3jRhyES8JK4gRsq-n5ev9tef3KrASbKR>
- [10] J. Schwinger; *On Quantum-Electrodynamics and the Magnetic Moment of the Electron*, *Phys. Rev.* **73** (1947) 416, <https://doi.org/10.1103/PhysRev.73.416>

- [11] P. Kusch and H. M. Foley; *The Magnetic Moment of the Electron*, *Phys. Rev.* **74** (1948) 250, <https://doi.org/10.1103/PhysRev.74.250>
- [12] T. Aoyama et al.; *The anomalous magnetic moment of the muon in the Standard Model*, *Phys. Rept.* **887** (2020) 1-166, [<https://doi.org/10.1016/j.physrep.2020.07.006>]
- [13] R. H. Parker et al.; *Measurement of the fine-structure constant as a test of the Standard Model*, *Science* **360.6385** (2018) 191–195, <https://doi.org/10.1126/science.aap7706>
- [14] P.A. Zyla; *Particle Data Group*, *Prog. Theor. Exp. Phys.* **8** (2020) 083C01, <https://doi:10.1093/ptep/ptaa104>
- [15] F. Ignatov; *Status of $R(s)$ measurements by energy scan method*, *EPJ Web of Conferences* **179** (2018) 01005, <https://doi.org/10.1051/epjconf/201817901005>
- [16] F. Jegerlehner; *The Anomalous Magnetic Moment of the Muon*, *Springer Tracts in Modern Physics* **274** (2017) 2nd edition, <https://doi.org/10.1007/978-3-319-63577-4>
- [17] A. Anastasi et al. [KLOE-2]; *Combination of KLOE $\sigma(e^+e^- \rightarrow \pi^+\pi^-\gamma(\gamma))$ measurements and determination of $a_\mu^{\pi^+\pi^-}$ in the energy range $0.10 < s < 0.95$ GeV²*, *JHEP* **03** (2018) 173, [https://link.springer.com/article/10.1007/JHEP03\(2018\)173](https://link.springer.com/article/10.1007/JHEP03(2018)173)
- [18] J. P. Lees et al. [BABAR]; *Precise Measurement of the $e^+e^- \rightarrow \pi^+\pi^-(\text{gamma})$ Cross Section with the Initial-State Radiation Method at BABAR*, *Phys. Rev. D* **86** (2012) 032013, <https://doi.org/10.1103/PhysRevD.86.032013>].
- [19] CMD-3 Collaboration; *Measurement of the $e^+e^- \rightarrow \pi^+\pi^-$ cross section from threshold to 1.2 GeV with the CMD-3 detector*, *Phys. Rev. D* **109** (2024) 11, 112002, <https://doi.org/10.1103/PhysRevD.109.112002>
- [20] Sz. Borsanyi et al.; *Leading hadronic contribution to the muon magnetic moment from lattice QCD*, *Nature* **593** (2021) 51-55, <https://doi.org/10.1038/s41586-021-03418-1>
- [21] T. Blum et al. (RBC, UKQCD); *Calculation of the Hadronic Vacuum Polarization Contribution to the Muon Anomalous Magnetic Moment*, *Phys. Rev. Lett.* **121** (2018) 022003, <https://doi.org/10.1103/PhysRevLett.121.022003>
- [22] A. Boccaletti et al.; *High precision calculation of the hadronic vacuum polarisation contribution to the muon anomaly*, *aeXiv [hep-lat]* (2024), <https://doi.org/10.48550/arXiv.2407.10913>;

- [23] M. Davier et al.; *Tensions in $e^+e^- \rightarrow \pi^+\pi^-(\gamma)$ measurements: the new landscape of data-driven hadronic vacuum polarization predictions for the muon $g-2$* , *Eur. Phys. J. C* **84** (2024) 721, <https://doi.org/10.1140/epjc/s10052-024-12964-7>;
- [24] M. Davier et al.; *Hadronic vacuum polarization: Comparing lattice QCD and data-driven results in systematically improvable ways*, *Phys. Rev. D* **109** (2024) 076019, <https://doi.org/10.1103/PhysRevD.109.076019>;
- [25] G. Charpak et al.; *Measurement of the Anomalous Magnetic Moment of the Muon*, *Phys. Rev. Lett.* **6** (1961) 128-132, <https://doi.org/10.1103/PhysRevLett.6.128>;
- [26] G. W. Bennett et al.; *Final report of the E821 muon anomalous magnetic moment measurement at BNL*, *Phys. Rev. D* **73** (2006) 072003, <https://doi.org/10.1103/PhysRevD.73.072003>;
- [27] D. P. Aguillard et al.; *Measurement of the Positive Muon Anomalous Magnetic Moment to 0.20 ppm*, *Phys. Rev. Lett.* **131** (2023) 161802, <https://doi.org/10.1103/PhysRevLett.131.161802>;
- [28] M. Abe et al.; *A new approach for measuring the muon anomalous magnetic moment and electric dipole moment*, *Progress of Theoretical and Experimental Physics* (2019) 053C02, <https://doi.org/10.1093/ptep/ptz030>;
- [29] C.M. Carloni Calame, M. Passera, L. Trentadue, G. Venanzoni; *A new approach to evaluate the leading hadronic corrections to the muon $g-2$* , *Physics Letters B*, Vol. **746** (2015) Pages 325-329, <https://doi.org/10.1016/j.physletb.2015.05.020>
- [30] G. Abbiendi et al. *Measuring the leading hadronic contribution to the muon $g-2$ via scattering*, *Eur. Phys. J. C* **77**, **139** (2017), <https://doi.org/10.1140/epjc/s10052-017-4633-z>;
- [31] G. Abbiendi et al., *Letter Of Intent: The MUonE Project*, CERN-SPSC-2019-026 (2019), <https://cds.cern.ch/record/2677471>;
- [32] G.Hall et al.; *Proposal for phase 1 of the MUonE experiment*; CERN-SPSC-2024-015 ; SPSC-P-370, <https://cds.cern.ch/record/2896293>;
- [33] B.E.Lautrup, A.Peterman, E.de Rafael, *Theory of the muon anomalous magnetic moment*, *Phys.Rep.* **3** (1972) 193, <https://link.springer.com/book/10.1007/3-540-32807-6>
- [34] G. Abbiendi et al. [OPAL Collaboration], *Measurement of the running of the QED coupling in small-angle Bhabha scattering at LEP*, *Eur. Phys. J. C* **45**, (2006) 1, <https://doi.org/10.1140/epjc/s2005-02389-3>;

- [35] P. Banerjee et al., *Theory for muon-electron scattering @ 10 ppm*, The European Physical Journal C volume **80**, (2020) 591 <https://doi.org/10.1140/epjc/s10052-020-8138-9>;
- [36] M. Alacevich, C. M. Carloni Calame, M. Chiesa, G. Montagna, O. Nicrosini and F. Piccinini, *Muon-electron scattering at NLO*, JHEP **02** (2019) 155 <https://arxiv.org/pdf/1811.06743.pdf>;
- [37] E. Budassi et al., *NNLO virtual and real leptonic corrections to muon-electron scattering*, JHEP **11** (2021) 098, <https://doi.org/10.1007/JHEP11%282021%29098>;
- [38] Carloni Calame et al., , *Towards muon-electron scattering at NNLO*, JHEP **11** (2020) 028, [https://link.springer.com/article/10.1007/JHEP11\(2020\)028](https://link.springer.com/article/10.1007/JHEP11(2020)028)
- [39] A. Broggio et al., *Muon-electron scattering at NNLO*, High Energy Phys. **01** (2023) 112, [https://link.springer.com/article/10.1007/JHEP01\(2023\)112](https://link.springer.com/article/10.1007/JHEP01(2023)112)
- [40] G. Abbiendi et al., *Lepton pair production in muon-nucleus scattering*, Phys. Lett. B **854** (2024) 138720, <https://doi.org/10.1016/j.physletb.2024.138720>;
- [41] M. Fael., *Hadronic corrections to $\mu - e$ scattering at NNLO with space-like data*, J. High Energ. Phys. **02** (2019), p. 027., [https://doi.org/10.1007/JHEP02\(2019\)027](https://doi.org/10.1007/JHEP02(2019)027);
- [42] M. Fael and M. Passera. *Muon-Electron Scattering at Next-To-Next-To-Leading Order: The Hadronic Corrections*, Phys. Rev. Lett. **122** (May 2019), 192001, <https://doi.org/10.1103/PhysRevLett.122.192001>;
- [43] CMS Collaboration, *The Phase-2 Upgrade of the CMS Tracker*, Tech. rep. CERN-LHCC-2017-009, CMS-TDR-014, (2017), <https://cds.cern.ch/record/2272264>;
- [44] M. Prydderch, *CBC3.1 User Manual* July 2019 (PDF), https://www.hep.ph.ic.ac.uk/ASIC/cbc3.1/Manuals/CBC3p1_User_Manual_V1p4.pdf;
- [45] R. Pilato (2022), *Feasibility study of the MUonE experiment*, (2022) <https://etd.adm.unipi.it/t/etd-02222023-185026/>;
- [46] M. Raymond, G. Hall, J. Crooks, and M. French. *The MGPA electromagnetic calorimeter readout chip for CMS*, IEEE Trans. Nucl. Sci. **52** (2005), pp. 756–763, <https://ieeexplore.ieee.org/document/1487720>;
- [47] E. Spedicato [MUonE collaboration], *A prototype electromagnetic calorimeter for the MUonE experiment: status and first performance results*, JINST **19** (2024) C02044, <https://iopscience.iop.org/article/10.1088/1748-0221/19/02/C02044>;

- [48] G. Grindhammer et al., *The Parameterized Simulation of Electromagnetic Showers in Homogeneous and Sampling Calorimeters*, (2000), <https://doi.org/10.48550/arXiv.hep-ex/0001020>;
- [49] G. Grindhammer, M. Rudowicz and S. Peters, *The Fast Simulation of Electromagnetic and Hadronic Showers*, *Nucl. Instrum. Meth. A* **290** (1989) 469, [https://doi.org/10.1016/0168-9002\(90\)90566-0](https://doi.org/10.1016/0168-9002(90)90566-0);
- [50] E. Spedicato, *Fast simulation of the MUonE 2021 test run setup*, <http://amslaurea.unibo.it/23207/>;
- [51] G. Abbiendi, *Status of the MUonE experiment*, *Phys. Scr.* **97** (2022) 054007, <https://doi.org/10.1088/1402-4896/ac6297>;
- [52] M. Al-Turany et al. *The FairRoot framework*, *J. Phys. Conf. Ser.* **396** (2012), p. 022001, <https://iopscience.iop.org/article/10.1088/1742-6596/396/2/022001>
- [53] CERN Geant4 team. Geant4 Simulation Toolkit, <http://Geant4.web.cern.ch/>;
- [54] CERN ROOT team. Data Analysis Framework, <https://root.cern.ch/>;
- [55] P. Asenov. *A Geant4-based simulation study for a preliminary setup of the MUonE experiment*, *Proceedings of the 41st International Conference on High Energy physics — PoS(ICHEP2022)*. Vol. **414** (2022), p. 905., <https://doi.org/10.22323/1.414.0905>;
- [56] Mölder, F. et al., *Sustainable data analysis with Snakemake*, *F1000Res* 10, (2021) 33, <https://pubmed.ncbi.nlm.nih.gov/34035898/>
- [57] M. Pentia et al., *Multiple Scattering Error Propagation in Particle Track Reconstruction*, *Rom. J. Phys.* **40** (1995) 181-191, <https://arxiv.org/abs/hep-ex/9406006>

Ringraziamenti

Questo lavoro e questi tre anni sono stati pienamente supportati da Umberto Marconi e Giovanni Abbiendi. Sono stata seguita in maniera molto professionale e umana in tutti gli aspetti di questo percorso, dai primi lavori, alla stesura e correzione della tesi. Per quest'ultima ringrazio particolarmente Giovanni per la sua attenzione al dettaglio su tutte le 100 e passa pagine. Vi ringrazio sinceramente per il sostegno e la fiducia che mi dimostrate ogni giorno. L'umanità, la condivisione e il sincero interesse alla persona non e' scontato, soprattutto in ambito lavorativo.

In maniera telegrafica ma comunque sentita:

ringrazio la mia famiglia e Matteo per il sostegno durante tutto il percorso. Sono grata anche a tutti gli amici incontrati in questi anni. A Bologna, dove ho conosciuto persone nuove con cui ho condiviso diversi interessi come cinema e musica o anche solo un buon te' (Giovanni, Elisa, Sara) e dove ho approfondito vecchie amicizie (Flex). Al CERN dove, nei mesi trascorsi, ho avuto l'occasione di conoscere persone che mi hanno accolta e aiutata a vivere a pieno e con entusiasmo quel periodo di indipendenza e scoperta (Giorgia, Sara, Chiara L., Chiara M., Federica, Andrea, Pietro).